Universidade de São Paulo
Instituto de Astronomia, Geofísica e Ciências Atmosféricas
Departamento de Astronomia

Thayse Adineia Pacheco

Hot Subdwarf stars in the integrated light of old stellar populations

São Paulo
2024

Thayse Adineia Pacheco

Hot Subdwarf stars in the integrated light of old stellar populations

Thesis presented to Departamento de Astronomia of the Instituto de Astronomia, Geofísica e Ciências Atmosféricas (IAG) at Universidade de São Paulo (USP) as a requirement to the achievement of the Ph.D. in Science.

Sub-area: Astronomy.
Advisors: Dr. Marcos Perez Diaz.
Dr. Paula Rodrigues Teixeira Coelho.

Versão Corrigida.
O original encontra-se disponível na Unidade.

São Paulo

2024

To my parents,

Adineia and Claudionor!

Acknowledgements

Aos meus orientadores Dr. Marcos Diaz e Dra. Paula Coelho, pela dedicação e paciência empregadas no desenvolvimento deste trabalho, também pelas correções do texto da tese e demais ensinamentos durante os últimos 4,5 anos; principalmente pelo apoio emocional durante os momentos difíceis em questões de saúde mental.

Ao Dr. Ricardo Schiavon, meu supervisor durante o período de sanduíche na Liverpool John Moores University, pelas discussões científicas que aperfeiçoaram minha pesquisa e pelo suporte durante as aplicações de pósdoc; também pelo otimismo e por acreditar no meu potencial; Aos meus colaboradores, Dr. Ronaldo Levenhagen e Dra. Lucimara Martins, pelas discussões enriquecedoras sobre atmosferas e populações estelares. Ao Dr. Jorge Meléndez pelas aulas, pelos conselhos e por me apoiar na mudança de área de pesquisa. To Dr Rafaelle Haywood, for supporting me in my applications.

Aos amigos do Observatório Abrahão de Moraes e do Atendimento Astronômico do IAG, especialmente ao Dr. Ramachrisna Teixeira, à Msc Rosely de Sousa e ao Dr. Reinaldo de Lima, por todo o apoio e energia restaurada nas atividades de atendimento ao público, fundamentais para a minha formação como astrônoma.

Ao Instituto de Astronomia, Geofísica e Ciências Atmosféricas (IAG) e a Universidade de São Paulo (USP) pelo suporte técnico e de infraestrutura, especialmente aos porteiros e agentes de limpeza. Aos técnicos de informática, Marco dos Santos, Luís Manrique e Ulisses Castello, por salvar o meu PC inúmeras vezes. Aos secretários, Daniel Bigardi, Márcia Ramos e Marcel Kimura. À Coordenação de Aperfeiçoamento de Pessoal de Nível Superior - Brasil (CAPES) - Código de Financiamento 001, pelo apoio financeiro. Ao Conselho Nacional de Desenvolvimento Científico e Tecnológico (CNPq), Ministério da Ciência, Tecnologia e Inovações pelo apoio financeiro durante o doutorado sanduíche. Ao

banco Santander, pelo apoio financeiro durante o período de mobilidade acadêmica.

Aos amigos do grupo de pesquisa Pleiad, Morgan Camargo, Msc Vinícius Branco, Lídia Ascon, Msc André Rodrigo da Silva, Dra. Danielle Santos e Dra. Maria Luísa Dantas.

Aos amigos do grupo de pesquisa de binárias jovens, que foram de grande suporte durante o isolamento social, Dra. Larisa Takeda, Dra. Patrícia Cruz, Florence de Almeida, Bruno Gerotti, Dr. Pedro Beaklini e Juliana Hirata.

To the friends from Liverpool, for the pubs, climbing, and hiking, Dra. Victoria Yankelevich, Dra. Sara Saracino, Elena Balakina, Tutku Kolcu, Andrew Mason, Beth Garton, Shobhit Kisku, Jonah Conley, Scarlett Royle, Ali Ranjbar, Adam Garner, Ryan Roberts, Jacob Wise, Andrea Sante, Helen Jermak, Dr. Sebastian Kamann, Pacome, Sara, Michael O'Connor, and Chris Rowe; to my love and partner João Bento.

Aos amigos que formei nesses últimos 6,5 anos no IAG: Lilianne Nakazono, Msc Maria Luísa Buzzo, Msc Natália Andrade, Dra. Miriam Molina, Msc Henrique Lupinari, Gabriela Carvalho (Mercedes), Msc Érik de Lima (Vinícius), Msc Geraldo Gonçalves, Elismar Losch (Santos), Pablo Araya, Marcelo Vicentin, Vitor Cernic, Msc Gabriel Fabiano, Guilherme Limberg, Dr. Helio Perottoni, Msc Loreany de Araújo, Msc Pedro Almeida, Msc Pedro Motta (Lúcifer), Dr. Fabio Cafardo, Msc André Luis, Raquel Ruiz, Isabel Bonomio, Giulya Souza, Msc Lia Doubrawa, Laís Borbolato, Stephan Hanada, Stela Addduci, Fernanda Nogueira, Dr. Julian Santos, Giovani Vicentin, Msc Catarina Aydar, Msc Yuri Abuchaim, Msc Amanda Rubio, Douglas Carlos, Luana Reis, Dr. Rafael Ribeiro, Dr. Felipe Almeida, Dra. Patricia Novais, Msc Thainá Sabino e Arthur Magalhães.

A Mariana Milena, minha afilhada, por dar energia e ser entusiasta da ciência, sempre me lembrando os motivos de eu ingressar na vida acadêmica; Ao Lucas Almeida, por todas as feiras veganas; Ao Klaus Prellwitz, por todos os memes e piadas ruins; Ao Hilton Milanez, ao Daniel Bragança, por todas as festas; Às amigas do sul, Dra. Marina Dal Ponte, Msc Jamile Fritz, Msc. Laís Gedoz e Msc Larissa Amaral, por todo o apoio emocional dedicado a distância. À Letícia Nogueira, por todos os desabafos e conversas; À Évelin Severo, por me incentivar, pelo suporte e longa amizade;

Àos amigos unidos pela AAAGW (Associação Atlética Acadêmica Gleb Wataghin), pela receptividade, momentos de descontração e festas, especialmente a Enzo Moriayma (Einy), Uiran da Silva, Hugo, Ana Paula Novoa, Marcelo Sime, Rodrigo Suigh, Érika Marchi, Evandro, Lucas Grassetti, Daniel Martini, André Santos (Deco).

Ao BAFEFI (Basquete Feminino da Física) e ao BarFEFI, por todos os treinos e por me ensinar que praticar esporte vai muito além do que acontece em quadra, especialmente à Dra. Thaís Silva (Santana), Renata Camargo (Beatriz), Msc Gabriela Camargo (Juliana), Lívia Sakimoto (Lavínia), Msc Jéssica Niide (Rabetânea), Dra. Louise Oliveira (Fernanda), Victoria Oliveira (Ick), Agnessa Nóbrega (Silvia), Msc Deborah Bertoldo (Isabela), Hyana Labanca (Rebeca), Laura Stephano (Beatriz), Caro Bedoya, Juliana Cocentino, Dra. Isabel Orselli, Graziella Bento, Ana Paula Tanaka, Ingrid Belotto, Malu Pellachin, Teresa Lanna, Maria Paula, Marina Raquel, Gabriele, Luiza Monticelli e ao treinador Nicolas Yudi.

À O Beco da USP, especialmente ao seu Adelino, seu Manoel e Paulinho, por sempre servir e ter uma mesa para as meninas.

Aos meus pais, Adineia e Claudionor, os principais incentivadores dos meus sonhos.

Esta tese/dissertação foi escrita em LaTeX com a classe IAGTESE, para teses e dissertações do IAG.

"*Ticking away the moments that make up a dull day*
Fritter and waste the hours in an offhand way
Kicking around on a piece of ground in your hometown
Waiting for someone or something to show you the way

Tired of lying in the sunshine, staying home to watch the rain
You are young and life is long, and there is time to kill today
And then one day you find ten years have got behind you
No one told you when to run, you missed the starting gun

And you run, and you run to catch up with the sun but it's sinking
Racing around to come up behind you again
The sun is the same in a relative way but you're older
Shorter of breath and one day closer to death

Every year is getting shorter, never seem to find the time
Plans that either come to naught or half a page of scribbled lines
Hanging on in quiet desperation is the English way
The time is gone, the song is over, thought I'd something more to say
[· · ·]"

George Roger Waters /
David Jon Gilmour / Nicholas Berkeley Mason / Richard William Wright

Abstract

Observational evidence indicates that hot Horizontal Branch stars such as Subdwarfs are the most likely candidates to account for the ultraviolet excess of old globular clusters and elliptical galaxies. These hot and evolved components are still missing in most of the libraries used in the synthesis of stellar populations. Due to this, some differences between models based on resolved and integrated light spectral fitting can translate into age differences of up to 50% in low metallicity globular clusters.

To address this problem, we first computed a detailed grid of non-LTE fully line-blanketed stellar atmosphere models for hot and moderately cool Horizontal Branch stars. This new library also provides high-resolution spectra and synthetic photometry in the range from 1 000 – 10 000 Å, covers ten temperatures within $10\,000 \leq T_{\rm eff} \leq 65\,000$, five surface gravities in the range $4.5 \leq \log g \leq 6.5$, two helium abundances matching two extreme helium-rich and helium-poor scenarios, and two limiting metallicity boundaries regarding both solar ([Fe/H] = 0) and Galactic halos ([Fe/H] = −1.5 and [α/Fe] = +0.4).

Secondly, this library was combined with others in the literature to model the integrated spectra of simple stellar populations based on the color-magnitude diagrams of NGC 2808 and NGC 7089. We propose modifying the CMD-based methodology in literature by directly matching each observed star to a synthetic spectrum in a ten-dimensional color plane, avoiding inaccuracies of current color-$T_{\rm eff}$ relations. This allows us to quantify the impact of Blue and Extreme Horizontal Branches in the integrated flux, which dominates the light in the far ultraviolet. This approach of stellar population synthesis models will help to break the degeneracy between age and Horizontal Branch morphology which is known to affect the integrated light of old stellar populations.

Resumo

Evidências observacionais indicam que estrelas quentes do Ramo Horizontal, como Subanãs azuis, são as candidatas mais prováveis para explicar o excesso no ultravioleta de aglomerados globulares velhos e galáxias elípticas. Essas componentes quentes e evoluídas ainda estão ausentes na maioria das bibliotecas utilizadas na síntese de populações estelares. Devido a isso, algumas diferenças entre modelos baseados em ajuste espectral de luz integrada e resolvida se traduzem em diferenças de idade de até 50% em aglomerados globulares de baixa metalicidade.

Para abordar esse problema, calculamos uma grade detalhada de atmosferas estelares totalmente *line-blanketed*, não-LTE, para estrelas da Ramo Horizontal quentes e moderadamente frias. Esta nova biblioteca também fornece espectros de alta resolução e fotometria sintética no intervalo de 1.000 a 10.000 Å, cobre dez valores de temperaturas entre 10.000 $\leq T_{\rm eff} \leq$ 65.000, cinco valores de gravidades superficiais entre 4,5 $\leq \log g \leq$ 6,5, duas abundâncias de hélio que correspondem a dois cenários extremos ricos e pobres em hélio, e dois limites de metalicidade em relação ao solar ([Fe/H] = 0) e halos Galácticos ([Fe/H] $= -1,5$ e $[\alpha/\mathrm{Fe}] = +0,4$).

Esta biblioteca foi combinada com outras na literatura para modelar os espectros integrados de populações estelares simples com base nos diagramas cor-magnitude de NGC 2808 e NGC 7089. Propomos modificar a metodologia baseada em diagramas cor-magnitude da literatura, combinando diretamente cada estrela observada com um espectro sintético em um plano em dez dimensões de cor, evitando imprecisões das relações cor-$T_{\rm eff}$. Isso nos permite quantificar o impacto dos Ramos Horizontais Azul e Extremo no fluxo integrado, que domina a luz no ultravioleta distante. Essa abordagem de modelos de síntese de populações estelares ajudará a quebrar a degenerescência entre idade e morfologia do Ramo

Horizontal, que é conhecida por afetar a luz integrada de populações estelares antigas.

List of Figures

List of Tables

Contents

Chapter 1

Introduction

Groups of stars that are born together and share characteristics such as age and chemical composition, orbiting a common kinematical center, are established as stellar populations. By studying stellar populations, we can comprehend the formation and evolution of star clusters and galaxies, including the Milky Way. This is in an interface where Galactic and extragalactic domains connect to stellar astrophysics.

The concept of stellar populations emerged in the 1940s following the observation of resolved stars in the local group of galaxies by Baade (1944). He analyzed such stellar data and compared it to the Hertzsprung-Russell (HR) diagram [1] of the solar neighborhood and Galactic stellar clusters. He concluded that stars can be categorized into distinct populations and suggested two types: type I resembles stars near the Sun and type II, which correspond to those in globular clusters.

Nowadays, the study of stellar populations can be divided into two primary approaches: resolved and integrated light. Resolved stellar populations comprise observing individual stars by analyzing them within a specific region or stellar cluster and providing detailed information about their properties. On the other hand, integrated stellar populations consider the light from all stars in an extended object, often because most individual stars can not be resolved, offering a perspective of the combined stellar content.

Due to observational limitations, most stellar systems solely possess integrated observations. As Galactic globular clusters can be observed both in resolved and integrated manners, they are essential proxies to test our integrated light models and methods. In this work, we adopted a two-step strategy, commencing with a resolved study that enables a comprehensive understanding of individual stars and their properties. Subsequently, this

[1] HR diagram: theoretical plane of luminosity vs. $T_{\rm eff}$.

information is employed to model the integrated light emitted by an entire population.

1.1 Stellar populations synthesis

The process of combining separate elements or components to create a unified whole or a more complex entity is named synthesis. It consists of merging distinct parts or ideas to form the assembly or integration of diverse elements to produce a comprehensive understanding of a new compound or concept. Methods of stellar population synthesis have been evolving for decades.

1.1.1 Early developments

Baum (1959) studied stars in nearby galaxies by plotting the ratio between stellar counts and surface brightness within selected regions and stellar colors. The data on dwarf ellipticals detected the presence of Population I, contradicting the earlier belief that only old Population II existed in those systems. He concluded that NGC 205 is mainly composed of Population II, while M 31 and M 32 exhibit an old-Population I majority alongside some Population II. This implies that the galaxy's evolution is primarily shaped by its initial mass and angular momentum rather than the inherent chemical distinctions of different stellar populations.

Crampin and Hoyle (1961) studied the old open cluster M67 and described the theoretical evolution of its $B-V$ color. They proposed the idea of dating extragalactic systems through their combined colors. Additionally, they highlighted the need for improvement in the theoretical stellar evolutionary tracks that predict the stellar properties such as temperature, size, and luminosity from the zero-age Main Sequence to the final stages of stellar evolution.

The first work to attempt the light modeling of the integrated stellar content in galaxies is Sandage (1961). He simulated the change in luminosity caused by stellar evolution in elliptical galaxies, intending to apply these findings to cosmological investigations. Sandage (1961) derived light travel time equations for distant galaxies, predicting changes in luminosity over time and offering corrections for observed magnitudes due to galaxy evolution. His model considers stellar evolution and implies an open, infinite universe with a mild expansion.

Later, Spinrad (1966) discusses how observations of stars can be combined to model the integrated light of galaxies. To understand the universe's geometry and expansion, he analyzed Galactic nuclei using the Hubble diagram [2], investigating how Galactic luminosity changes over time. This study shows the complexity of cosmology's observational tests linked to stellar evolution. Already at this early effort, Spinrad (1966) also discusses how the stellar content in stellar clusters can be used to interpret galaxies, even mentioning Horizontal Branch stars, Blue Stragglers, and White Dwarfs.

Tinsley (1968) computed the first model for a galaxy and analyzed its evolutionary history. She based the method on the evolution of color indices and effective temperature ($T_{\rm eff}$-color) relations by Johnson (1966). The upper Main Sequence and the Subgiant Branch were represented by evolutionary models, while the Red Giant Branch and the lower Main Sequence were empirically included. The number of stars at each evolutionary phase was proportional to their lifetimes, and Tinsley (1968) claimed that the Post-Main Sequence mass dispersion was less important due to their fast evolution.

The next generation of stellar population synthesis method is presented by Tinsley (1972) and Faber (1972). They modeled the gas content, mass-to-light ratios, and colors of elliptical galaxies, regions of spirals, and globular clusters. Faber (1972) models suggest a rise in metal abundance with higher galaxy luminosity. The properties derived from the Tinsley (1973) model were based on star formation rates and initial mass function assumptions, providing insights into Galactic evolution. The evolution of luminosity, stellar masses, remnant mass, outflow rate, and yields of heavy elements were analytically developed in this model.

1.1.2 Current methodologies

Nowadays, there are three main methodologies to model integrated stellar populations: isochrone synthesis, the fuel consumption theorem, and color-magnitude diagram-based recipes.

Evolutionary Synthesis. The models known today as isochrone synthesis transformed stellar population studies, incorporating stellar evolution, spectral libraries, and initial mass functions for comprehensive galaxy studies. These models of simple stellar popu-

[2] Hubble diagram: correlation between the redshifts and distances of galaxies.

lations were an advancement of the Tinsley (1972), Faber (1972), and Bica (1988) work. This method offers insights into star formation bursts and facilitates the interpretation of galaxy composite spectra, promising applications in studying distant galaxies (Bica, 1988). They came about because discrete sampling in stellar evolution tracks posed challenges, impacting the precision of models.

Initially, struggling with photometric observations of nearby galaxies that standard models could not explain, Bruzual (1983), Charlot and Bruzual (1991), and Bruzual and Charlot (1993) introduced improvements in algorithms for stellar population synthesis by using isochrones instead of evolutionary tracks. Isochrones, representing stars of identical age and metallicity on the Hertzsprung-Russell diagram, aid in correlating temperature, gravity, and mass. Bruzual and Charlot (1993) refined the isochrone synthesis by employing a stellar spectral library with broader spectral coverage to predict the population evolution.

Bruzual and Charlot (2003) is the first work that studies absorption lines across various ages and metallicities, accurately reproducing spectral indices and providing insights into star formation histories and metallicities of galaxies. The model effectively reproduces observed star clusters and galaxy spectra, constraining star formation, metallicity, and dust content. This is important in the context of broader galaxy studies that need composite stellar populations. Such modeling requires factors such as dust attenuation, star formation history, chemical evolution, and simple stellar populations. The initial mass function also impacts mass-to-light ratio, luminosity evolution, and spectral energy distributions.

Cid Fernandes et al. (2005) computed the spectral synthesis of galaxies using a large dataset of observed spectra from the Sloan Digital Sky Survey and a base of simple stellar populations models of Bruzual and Charlot (2003). They applied the method to a sample of 50362 galaxies, producing a catalog of stellar population properties and emission lines.

Moura et al. (2019) combine isochrones to calculate several synthetic spectra with different parameters such as age, metallicity, and helium abundance. They reproduced integrated spectra of Galactic old globular clusters. In addition, Rennó et al. (2020) identified lines to determine element abundances and examined the impact of enhanced sodium abundances due to multiple stellar populations.

The fuel consumption theorem. The fuel consumption theorem was proposed by Renzini and Buzzoni (1986), as an alternative way to deal with the problem of discrete sampling

in stellar evolution tracks by modeling the Post-Main Sequence phases in an alternative manner. It reveals the proportional relationship between the nuclear fuel burned in a Post-Main Sequence evolutionary phase and its contribution to the total luminosity of a simple stellar population. This model includes all the evolutionary phases from the Main Sequence to the Asymptotic Giant Branch and takes into account different Horizontal Branch morphologies. The contributions of stars over time evolve distinctively, as observed particularly in ultraviolet bands, as indicated in the conclusions of Renzini and Buzzoni (1986). The increase in ultraviolet luminosity is mostly due to the young stars correlating with higher star formation rates over time. The ultraviolet emission declines quickly within 2-3 Gyrs, leading to a softer spectrum [3] because the Horizontal Branch has been shifted towards the red for younger globular clusters. On the other hand, the ultraviolet light from post-Asymptotic Giant Branch stars decreases rapidly with time, resulting in fading but harder spectra [4]. The ultraviolet radiation emitted by binaries correlates with the binary components' death rate, indeed their ultraviolet contribution increases with galaxy redshift.

The modern models by Maraston (2005), Maraston (2011) and Maraston and Strömbäck (2011) adopt the fuel consumption theorem. They are based on Maraston (1998), who illustrated the bolometric budget of a simple stellar population over time using this theorem. These works computed a grid of simple stellar populations covering a wide range of ages (up to 15 Gyr) and metallicities. She also compared her models to the integrated luminosity of stellar systems, finding good agreement, both in the optical and infrared, provided the flux is correctly calibrated for thermally pulsing Asymptotic Giant Branch stars.

CMD-based synthesis. Instead of using isochrones and an ad-hoc assumption of the initial mass function, a stellar population synthesis model can also be built upon an observed Color-Magnitude Diagram (CMD) and a library of stellar spectra. In this method, each star in an observed Color-Magnitude Diagram is matched to a representative spectrum from the library. This approach combines the photometry of all individual stars of the globular cluster to create a single integrated spectrum, weighting each stellar spectrum

[3] Soft Spectrum: Lower-energy radiation, longer wavelengths, common in cooler stellar regions.

[4] Hard Spectrum: Higher-energy radiation, shorter wavelengths, typically linked to X-rays emission.

proportionally to their observed total flux in a chosen photometric band (Santos et al., 1990, 1995; Schiavon et al., 2004; Martins et al., 2019).

By being based on observed CMDs rather than isochrones or evolutionary tracks, this approach is particularly useful to study the impact of stellar phases which are not yet well predicted by our stellar evolution models. This is the case, for example, of the extended Horizontal Branch stars and the Blue Stragglers. The loci of these phases in the Hertzsprung-Russell diagram cannot yet be predicted from first principles from stellar evolution models, and require some ad-hoc assumptions about the mass loss at the tip of the Red Giant Branch (Sweigart et al., 2002), the influence of stellar binarity (Pelisoli et al., 2020) and the He mass fraction of the stars.

This is the method of choice for our work, due to its advantages of not relying on assumptions about the initial mass function and (in)accuracies of the stellar evolution predictions. We detail our approach in more detail in later chapters.

1.1.3 The role of stellar libraries

Theoretical and empirical libraries have opposite strengths and weaknesses. In short, one can say that synthetic libraries have wider parameter coverage, while empirical libraries have more accurate individual star spectra.

Various empirical libraries exist, such as ELODIE (Soubiran et al., 1998; Prugniel and Soubiran, 2001; Le Borgne et al., 2004), MILES (Sánchez-Blázquez et al., 2006; Cenarro et al., 2007; Falcón-Barroso et al., 2011; Sharma et al., 2015) and X-shooter Spectral Library (Chen et al., 2014; Verro et al., 2022). The Hertzsprung-Russell coverage of empirical spectra is often incomplete due to sampling stars from the solar neighborhood. Due to the sparse coverage in certain stellar evolutionary phases, and uncertainties in parameters like temperature, we face challenges in constructing stellar population synthesis models. This implies that models based solely on such libraries cannot reproduce chemical enrichments different than our local system, such as the α-enhancement in elliptical galaxies. (see discussions in e.g. Worthey et al., 1992; Thomas et al., 2003; Coelho et al., 2007; Coelho, 2009a).

Regarding theoretical libraries, various theoretical libraries exist, such as Barbuy et al. (2003); Martins et al. (2005); Coelho et al. (2005); Coelho (2014), Husser et al. (2013), and others, with differing specialties and limitations. They cover a wide parameter range

but depend on the accuracy of input parameters such as opacities. The comparisons between theoretical and empirical stellar spectra reveal challenges due to inaccuracies in the opacity lists, such as incomplete atomic and molecular data, especially for cooler stars ($T_{\rm eff} \leq 5\,000\,{\rm K}$) and specific spectral regions (e.g. Martins and Coelho, 2007, 2017; Lançon et al., 2021).

Martins et al. (2019) evaluated the effectiveness of using stellar spectral libraries to create a synthetic integrated spectrum for 30 globular clusters based on photometric data, without any assumptions about the initial mass function or isochrones. The integrated spectrum of the globular clusters, both synthetic and observed, were compared, and the quality of the synthetic spectrum was assessed by measuring the absolute average deviation in flux. After a careful performance evaluation of the libraries tested, it was found that the Coelho (2014) theoretical library demonstrated superior results when wider wavelength ranges were fitted.

Coelho et al. (2020) explored how the choice of either theoretical or empirical library affects the stellar population models and galaxy parameters inferred from spectral fitting. In short, they name the coverage effect as the impact of sub-optimal coverage of the Hertzsprung-Russell diagram by empirical libraries, and the synthetic effect as the impact of inaccuracies in theoretical libraries. The study revealed that color predictions are more affected by the coverage effect, while spectral indices are affected by both effects. Galaxy ages remain mostly unchanged by the synthetic effect but are underestimated when empirical libraries are used with limited parameter models. Metallicities hold up against the limited Hertzsprung-Russell diagram coverage of the empirical libraries but are underestimated when synthetic libraries are used.

Ultimately, no single library, purely theoretical or empirical, covers all needed parameters, so combining varied libraries based on their strengths and weaknesses is essential (see as well Coelho, 2009b). Yet, Martins et al. (2019) and Coelho et al. (2020) demonstrated that modern theoretical libraries are highly competitive, surpassing the performance of empirical libraries in several instances.

1.1.4 Hot low mass stars in stellar population synthesis

The blue and ultraviolet flux is dominated by the locus of the Turn-Off, younger systems showing brighter and hotter stars. But hot low-mass stars such as hot Horizontal

Branch or Blue Straggler stars also contribute to the blue flux, and ideally, we should be able to distinguish between the two. This poses a problem for the spectroscopic dating of extragalactic globular clusters, be it through indices or spectral fitting.x Greggio and Renzini (1990) investigate the origin of strong ultraviolet radiation flux in elliptical galaxies, questioning whether it arises from young massive stars or old low-mass stars. Results suggest potential sources such as hot Horizontal Branch stars, AGB-manque, and post-EAGB stars, but uncertainties remained. Further observations were necessary to distinguish among candidates, particularly in resolving stellar systems like globular clusters and galactic bulges.

Regarding the effect on spectral indices, de Freitas Pacheco and Barbuy (1995) utilized Galactic globular cluster data to demonstrate that models for the Hβ index need to consider the Horizontal Branch morphology (together with metallicity) to recover the observed values properly. These findings, supported by ultraviolet observations, suggest that a blue Horizontal Branch may significantly contribute to the Hβ strength in an integrated stellar population.

This has been reinforced by the results from Schiavon et al. (2004). The authors used the ratio of Hδ_F to Hβ equivalent widths in old globular clusters and concluded that they are more sensitive to Horizontal Branch morphology than age, indicating that these clusters with blue Horizontal Branches appear younger despite their old age. The method allows distinguishing true intermediate-age clusters from those with strengthened Balmer lines by blue Horizontal Branch stars in integrated spectra. This was a significant step in beginning to break the degeneracy between age and Horizontal Branch morphology, and this is still used as an indicator.

The age – Horizontal Branch morphology degeneracy also affects inferences from spectral fitting. Spectral fitting is employed for estimating a galaxy's history by utilizing libraries of simple stellar populations to fit the integrated light of stellar populations.

Ocvirk (2010) derived spectroscopic ages in low-metallicity globular clusters by using optical integrated spectra. They obtained ages that are several gigayears younger than those measured from the Turn-Off, persisting across different models and interpretation methods. The false young bursts emerge in the reconstructed star formation history and contribute up to 12% of optical light. In the work of Ocvirk (2010), red Horizontal Branch clusters fit well with old stellar population models, while blue Horizontal Branch clusters

require an additional hot component.

Recent articles like Gonçalves et al. (2020) show the problem persists even with modern and widely-used codes and models based on isochrone synthesis. Unfortunately, some differences between models based on resolved and integrated light spectral fitting can translate into age differences of 50% (Gonçalves et al., 2020) in low metallicity globular clusters.

Expanding the studies towards the ultraviolet, Peterson et al. (2003) analyzed the mid-ultraviolet and optical spectra of a moderately metal-rich M31 cluster. They employed theoretical stellar spectra and found a good fit with cool and hot blue Horizontal Branch stars, consistent with the color-magnitude diagram. The Turn-Off temperature aligns with Galactic globular clusters, indicating a comparable age. The authors recommend considering hot Horizontal Branch stars in spectral fits of metal-rich populations to avoid potential age underestimates. This is compounded by observational evidence indicating that hot Horizontal Branch stars such as hot Subdwarfs are the most likely candidates to account for the UV-excess observed on spectroscopic and photometric analyses of globular clusters and elliptical galaxies (Yi et al., 1999; Busso et al., 2005; Green et al., 2008).

Furthermore, the UV upturn in nearby early-type galaxies is also attributed to Horizontal Branch stars and their descendants. Yoon et al. (2004) suggested that the Horizontal Branch temperature variation is influenced by both age and metallicity. They proposed the UV upturn as a potential age indicator for the universe's oldest populations, such as early-type elliptical galaxies. As the origin of the extended Horizontal Branch and possibly the ultraviolet upturn phenomenon, Yi (2008) hypothesizes an extreme helium abundance.

In essence, to be able to retrieve reliable ages, models of the integrated stellar population need to take these stars into account. Maraston and Thomas (2000) investigated Composite Stellar Population models by combining old metal-rich and old metal-poor components in elliptical galaxies, reproducing with purely old ages the integrated observed Hβ strengths. They attribute the reason to their different treatment of the Horizontal Branch morphology when compared to isochrone synthesis models.

The extreme Horizontal Branch has been later incorporated into isochrone synthesis models by Hernández-Pérez and Bruzual (2013). The authors incorporated interacting binary pairs of helium white dwarfs, followed by a merger channel. This scenario can effectively explain the presence of extreme Horizontal Branch stars in metal-rich open

clusters. The study also offered insights into the UV upturn phenomenon observed in elliptical galaxies.

Recently, Cabrera-Ziri and Conroy (2022) chose to include one hot Horizontal Branch star in the synthesis of the integrated spectrum. The approach simultaneously models the age, abundance, and Horizontal Branch properties of integrated stellar populations, comparing the integrated spectra with resolved color-magnitude diagrams. The ages derived from spectral fits closely match color-magnitude values for most targets. This study introduces a diagnostic to identify spurious solutions in age, enhancing the method's reliability.

The study of White Dwarfs to analyze stellar populations in ultraviolet was introduced by Bica et al. (1996). They used high Signal-to-Noise ratio IUE (International Ultraviolet Explorer) spectra representing different classes of White Dwarf stars and provided stellar parameters corresponding to each group of White Dwarfs.

Levenhagen et al. (2017) built a theoretical library of White Dwarf stars based on `TLUSTY` atmosphere models. They used isochrone synthesis to investigate the effect of their White Dwarf spectra on the integrated light and suggest that DA White Dwarfs may be detectable in ultraviolet bands for populations older than 8 Gyr. Therefore, it requires consideration in the context of age determination.

It became clear that hot low-mass stars affect the optical light enough to mimic younger ages and that expanding towards the ultraviolet is essential to disentangle the age-Horizontal Branch degeneracy. Most libraries of stellar population synthesis are optimized in the optical and near-infrared wavelengths, for example, UVES-POP (UVES Paranal Observatory Project, Bagnulo et al. (2003); Borisov et al. (2023)). The only high-resolution spectral library dedicated to the ultraviolet is UVBlue (Rodríguez-Merino et al., 2005), which covers the low gravities ($0.0 \leq \log g \leq 5.0$) of the blue giant model parameter space. Therefore, we must improve the spectral synthesis in the ultraviolet and far-ultraviolet bands, especially for high-gravity models, to predict the ages of old stellar populations more reliably.

1.2 Subdwarfs

Hot Subdwarfs are stars that were stripped of part of their outer layers, thus exposing their hot He core. In this section, we will explore the current state of hot Subdwarf star

research, exploring their physical and chemical characteristics, formation, and evolution, as well as the state-of-the-art regarding spectral synthesis.

1.2.1 Overview

Hot Subdwarfs were first photometrically observed as faint blue stars by Humason and Zwicky (1947). They were looking for new White Dwarfs with the 18-inch Schmidt telescope at Palomar observatory. Also, for the first time, hot Subdwarf stars were positioned on the Hertzsprung-Russell diagram at the blue end of the Horizontal Branch, exhibiting an absolute magnitude around 0. Although hot Subdwarfs have low luminosity in the visible and infrared bands, they are luminous in the ultraviolet wavelengths. Another sample of hot Subdwarfs was spectroscopically observed by Greenstein and Sargent (1974), who determined their effective temperatures and surface gravities to settle them in the Kiel diagram [5]. A decade later, Kilkenny et al. (1988) studied stars spectroscopically, classified 1 225 hot Subdwarfs, and, for the first time, cataloged hot Subdwarfs.

As an extension of the Horizontal Branch, hot Subdwarfs are characterized by effective temperatures higher than 15 000 K (Luo et al., 2019). Hot Subdwarfs are typically hotter than Main Sequence stars at the same luminosity, having spectral types O or B. In comparison to Main Sequence stars of similar spectral type, hot Subdwarfs exhibit lower mass (Geier et al., 2017a), which implies higher gravity and lower luminosity and thus are also known as hot subluminous stars (Heber, 2016). Hot Subdwarfs shine towards the hot side of the Hertzsprung-Russell diagram, mostly between the Main Sequence and the White Dwarf cooling sequence as shown in Figure 1.1.

[5] Kiel diagram: theoretical plane of $T_{\rm eff}$ vs. $\log g$.

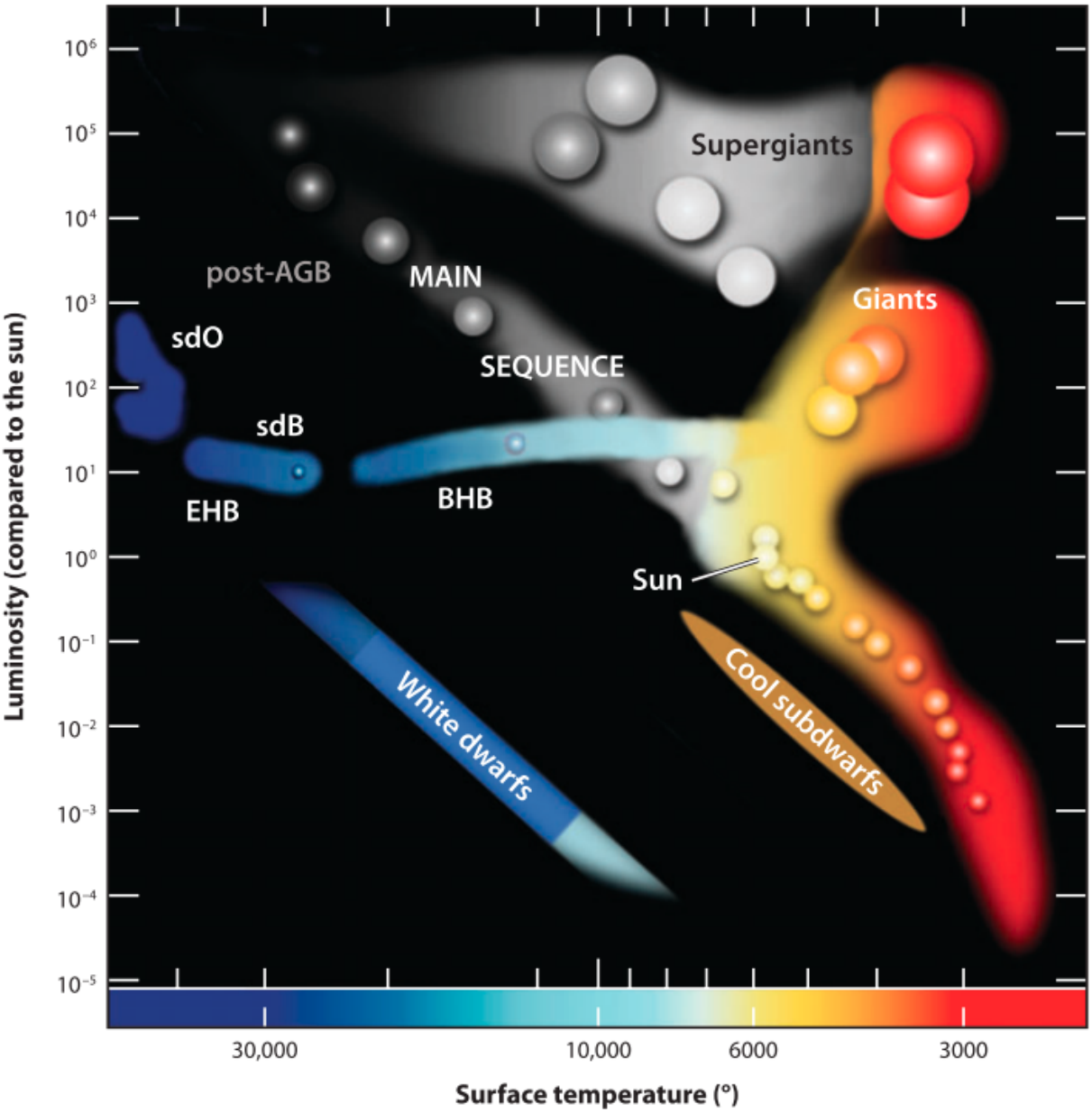

Figure 1.1: Scheme of a Hertzsprung-Russell diagram highlighting the position of type-O and type-B Subdwarf stars (sdO and sdB, respectively), and the extreme Horizontal Branch (EHB) located on the left and below the blue end of the Horizontal Branch (BHB) but above the White Dwarfs cooling sequence. From Heber (2009); © ARA&A.

The progress of current surveys such as Gaia Collaboration et al. (2016) allows us to observe these subluminous low-mass stars in much larger numbers. Culpan et al. (2022) updated the catalog of hot subluminous stars using the improved accuracy of the *Gaia* mission Early Data Release 3 (EDR3; Gaia Collaboration et al., 2021). Hot Subdwarf stars were observed by the *Gaia* and ongoing spectroscopic surveys which reveal the population of hot Subdwarfs nearby. The Geier (2020) catalog that spectroscopically classified hot

subdwarfs was complemented with newly discovered objects from DR6/7 of the LAMOST survey (Luo et al., 2021). Then, based on the astrometric and photometric selection quality criteria, Culpan et al. (2022) created a complete full-sky catalog of hot Subdwarfs stars.

A visual representation of hot Subdwarfs in terms of their observational parameters can be seen in Figure 1.2. This color-magnitude diagram of stars from the Solar neighborhood shows thousands of hot Subdwarfs in cyan crosses (Culpan et al., 2022). Hot Subdwarfs also are much less common compared to Main Sequence stars. Perhaps, this can be attributed to their evolutionary scenario being a still-emerging field of research. The hot Subdwarfs stars can be misclassified as White Dwarfs, extremely low-mass White Dwarf, or even cataclysmic variables due to their similar atmospheric parameters.

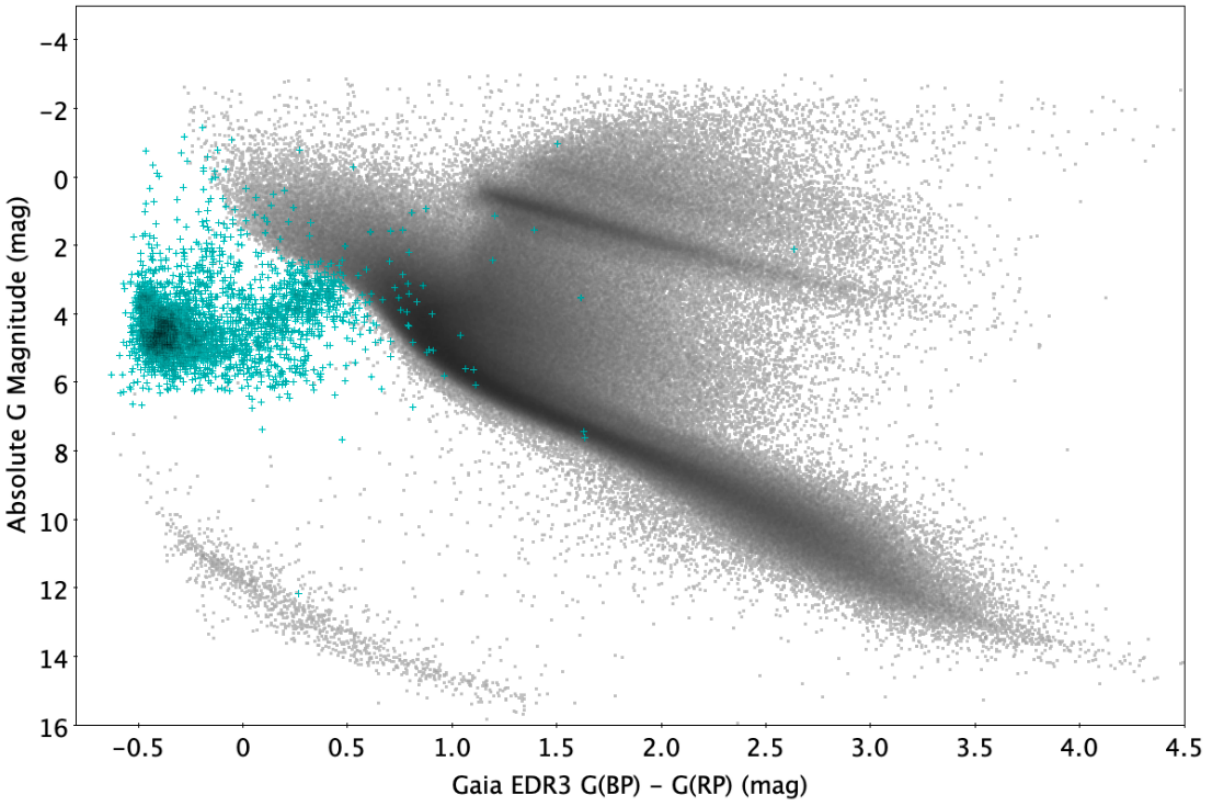

Figure 1.2: Color–magnitude diagram from Gaia EDR3 (grey dots) with the 3 373 known hot Subdwarfs from Gaia DR3 catalog (cyan crosses). From Culpan et al. (2022); © A&A.

Overall, the hot Subdwarfs' synthetic spectra have been built for specific targets and studies. We have hundreds of hot Subdwarf stars cataloged (Geier et al., 2017b; Heber et al., 2017; Geier et al., 2019; Geier, 2020; Culpan et al., 2022), with their spectral analysis focused on classification and/or kinematic properties (Luo et al., 2019; Luo et al., 2021).

The hot Subdwarfs can be separated into three main groups according to their spectra

(Saffer et al., 2000).

(i) Those nonbinaries that have no detectable spectral lines from a cool companion, and show only small or insignificant radial velocity variations (35%).

(ii) Those single-lined spectroscopic binaries that have significant or large velocity variations and probable orbital periods on the order of a day (45%).

(iii) Those showing additional spectral lines from a cool FGK Main Sequence or Subgiant companion that have slowly varying or nearly constant velocities, indicating periods of many months to years.

A lot of work was done to analyze the He-abundance (Fontaine et al., 2019) and its sequences (Lei et al., 2019a). The sequences also show differences between field hot Subdwarfs and extreme Horizontal Branch stars in globular clusters (Lei et al., 2020).

1.2.2 Observed chemical abundances

Analysis from asteroseismology (Charpinet et al., 2005), spectroscopy (Wade et al., 2005; Dorsch et al., 2018; Dorsch et al., 2019), and photometry (Johnson et al., 2014) of field hot Subdwarf stars found nonsolar He abundances. The spectral chemical analysis of hundreds of hot Subdwarfs by Edelmann et al. (2003) and Németh et al. (2012), and updated by Lei et al. (2019a,b, 2020) using LAMOST data, found that hot Subdwarfs can be grouped into two chemical regimes, He-rich and He-poor. They present a linear correlation between the He over H ratios $\log(n\mathrm{He}/n\mathrm{H})$ and the effective temperatures T_{eff}, which suggests the following fitting formula to He-enriched (Equation 1.1) and He-deficient (Equation 1.2) hot Subdwarf stars:

$$\log\left(\frac{n\mathrm{He}}{n\mathrm{H}}\right) = -3.53 + 1.35\left(\frac{T_{\mathrm{eff}}}{10^4\mathrm{K}} - 2.0\right) \tag{1.1}$$

$$\log\left(\frac{n\mathrm{He}}{n\mathrm{H}}\right) = -4.26 + 0.69\left(\frac{T_{\mathrm{eff}}}{10^4\mathrm{K}} - 2.0\right) \tag{1.2}$$

These sequences also support the evidence that He-enriched Subdwarfs-O are more common than the He-deficient ones (Heber, 2009).

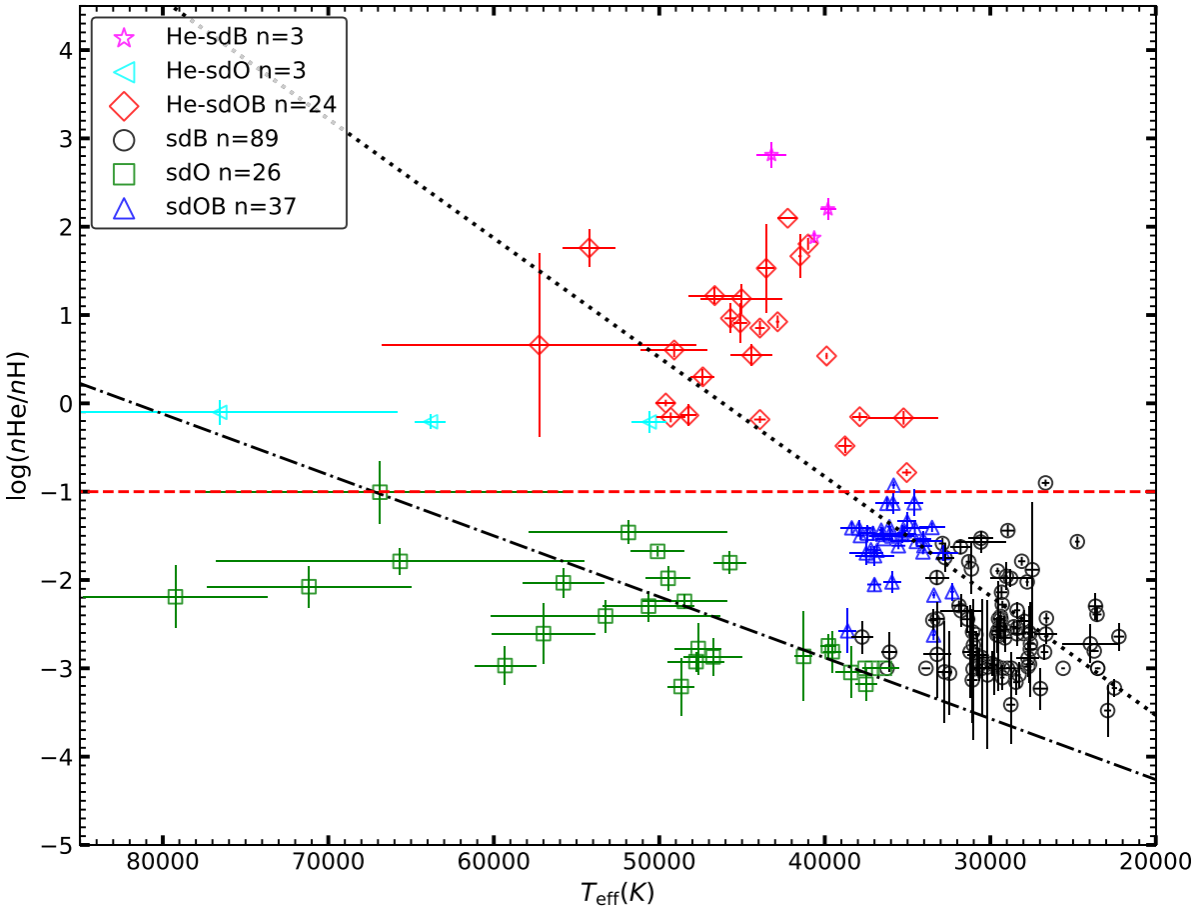

Figure 1.3: $T_{\rm eff}$–log(nHe/nH) diagram. The black dotted line and dotted–dashed line are the linear regression lines fitted by Edelmann et al. (2003) and Németh et al. (2012), respectively for He-enriched and He-deficient hot Subdwarf. The red dashed line is the solar He abundance. From Lei et al. (2020); © ApJ.

Figure 1.3 shows the parameter diagrams for the 182 single-lined hot Subdwarf stars in Lei et al. (2020). The majority of stars are in a region that is well-defined by the zero-age Horizontal Branch and terminal-age Horizontal Branch, demonstrating that these stars are undergoing helium burning in their cores; the 89 Subdwarf-B stars appear as black circles. The 37 Subdwarf-OB stars present higher effective temperatures and log g than Subdwarf-B stars and they are shown as blue up triangles. The 26 Subdwarf-O stars and the 3 He-Subdwarf-O stars present the highest effective temperatures in the sample, exhibited in green squares and aqua left triangles, respectively. The 24 He-Subdwarf-OB stars are clustered with intermediate parameters and they are indicated as red diamonds. Although they are located in the area close to the He-Subdwarf-OB stars, the 3 He-Subdwarf-B stars, in magenta stars, present the sample's highest He abundance. They also show the two separate He sequences from Equations 1.1 and 1.2, a He-enriched sequence represen-

ted by the dotted line and a He-deficient sequence represented by the dotted–dashed line. Additionally, Lei et al. (2019a) identified that the He-weak sequence exclusively encompasses Subdwarf-O stars, whereas the He-rich sequence contains all the other hot Subdwarf categories.

1.2.3 Subdwarfs as observed in Globular Clusters

In observed color-magnitude diagrams of globular clusters, hot Subdwarf stars often share the same locus as Extreme or Extended Horizontal Branch stars. The morphology of the Horizontal Branch in globular clusters depends on several factors. It is more extended for low metallicities, as lower opacities lead to a higher efficiency of energy transport within the stars. This affects the overall evolution of any star, particularly during the post-main sequence phases. Stars with lower masses also undergo a helium core flash at the tip of the red Giant Branch, thereby impacting where they fall within the Horizontal Branch. This has implications for the evolution and properties of hot Subdwarf stars concerning the helium content of cluster populations. The helium content, identified as a potential second parameter, is challenging to test in early-type stars. However, measurements from the spectral lines of blue Horizontal Branch stars in a specific temperature range offer a direct determination of this content, revealing helium enrichment in NGC 2808 Blue Horizontal Branch stars (Heber, 2009).

Figure 1.4 compares evolutionary models with the observed color-magnitude diagram for NGC 2808 (Heber, 2009, 2016). For the construction of the evolutionary models, Lee et al. (2005) considered four distinct populations with different helium abundances (Y) but the same metallicity (Z=0.0014) (Yi, 2008). Figure 1.4 a shows the observed color-magnitude diagram and four isochrones with distinct helium content (Y = 0.23, 0.31, 0.36, and 0.43) and an age of 10.1 Gyr. The cluster shows an exceptionally wide distribution of Horizontal Branch stars. It can be precisely reproduced in theory, for example, by assuming a large range of helium abundance. The Horizontal Branch is divided into regions that characterize stars with similar He content and physical parameters. As can be seen in Figure 1.4 b, the modeled color-magnitude diagram shows the red clump in grey, the red Horizontal Branch in red, the blue Horizontal Branch in green, and the extreme Horizontal Branch such as hot Subdwarfs in blue.

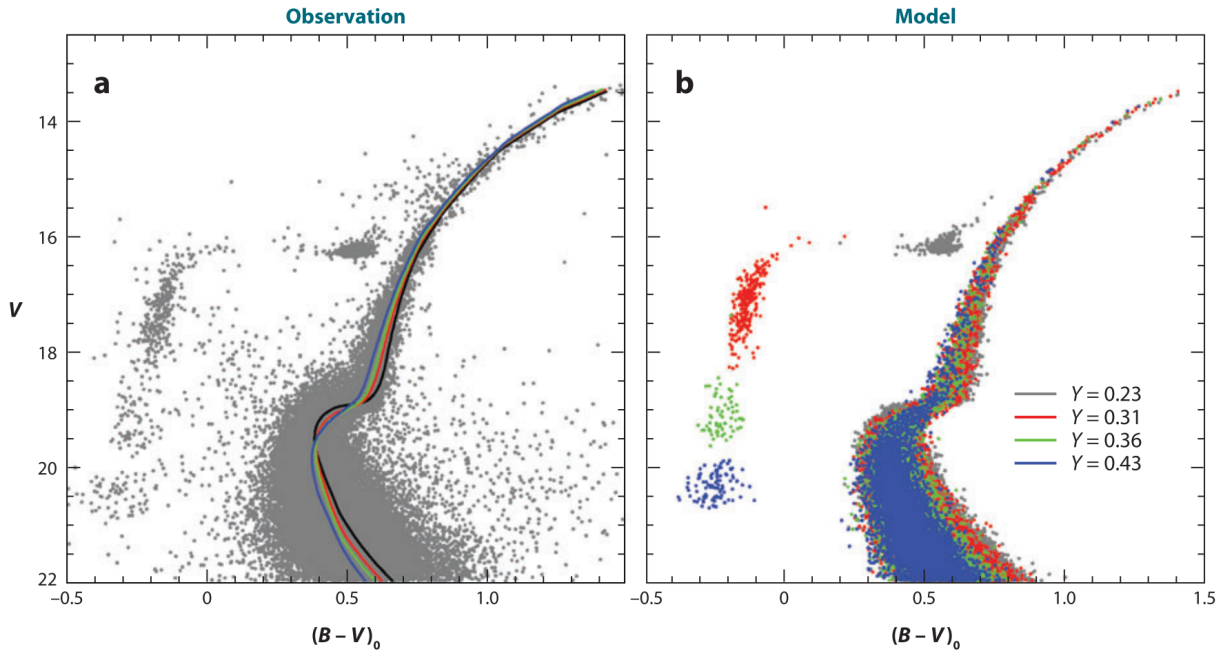

Figure 1.4: The observed and modeled color-magnitude diagrams of the globular cluster NGC 2808. (a) Observed color-magnitude diagram compared to four isochrones with different helium abundances but the same metallicity (Z=0.0014) and age (10.1 Gyr). (b) Modeled color-magnitude diagram produced by four distinct populations with different helium content (Y = 0.23, 0.31, 0.36, and 0.43). In Heber (2009, 2016) from Lee et al. (2005) and Yi (2008); © ARA&A.

Globular clusters such as NGC 2808 display multiple stellar populations, reflected in their color-magnitude diagrams, and ongoing surveys, like the HST UV legacy survey, aim to unravel complexities and enhance understanding, suggesting multiple episodes of star formation (Heber, 2016). This is important as insights to understand the formation channels and evolutionary paths of these stars.

1.2.4 Evolutionary paths

Hot Subdwarf stars, generally old, reach far beyond typical Main Sequence stars. Hot Subdwarfs are characterized as remnants of stars that have exhausted their nuclear hydrogen (Lynas-Gray, 2004). The evolution of hot Subdwarf stars follows a trajectory from low- to intermediate-mass progenitors, reaching the Helium Main Sequence, a stage characterized by central Helium burning and equivalent to the Horizontal Branch phase. According to canonical evolutionary models, the structure of the hot Subdwarf stars is believed to be an exposed Helium core of approximately half a solar mass, featuring a thin inert hydrogen envelope (Heber, 2009). This characteristic prevents hot Subdwarf stars from ascending

the Asymptotic Giant Branch. Hot Subdwarf stars are often found at the blue end of the Horizontal Branch or mixed with post-Horizontal Branch stars in the Hertzsprung-Russell diagram. The distribution of stars along the Horizontal Branch is primarily influenced by variations in the envelope and total mass, with the hottest stars exhibiting minimal hydrogen envelope mass (Heber, 2016).

Standard evolution of low-mass stars typically undergo the He core flash at the Red Giant Branch tip, but if enough mass is lost, they appear directly at blue positions in the Hertzsprung-Russell diagram. The most accepted formation scenario is of an extremely hot Horizontal Branch star that lost nearly all of its H outer layers during the Red Giant phase (Mengel et al., 1976). After this, the exposed He-core evolves towards the White Dwarf cooling sequence by avoiding the Asymptotic Giant Branch (Wade et al., 2005; Heber, 2009; Fontaine et al., 2012). Post-Extreme Horizontal Branch evolution leads to higher temperatures until the White Dwarf cooling sequence is reached, resulting in increased gravity. Despite being sometimes misidentified as low-mass White Dwarfs, hot Subdwarfs "are the stripped cores of red giants, which managed to ignite He while retaining just a little bit of H as their envelope" (Heber, 2016). In this case, they can experience the Helium flash while descending the White Dwarf cooling sequence, forming "hot flashers" near the Horizontal Branch (Iben, 1984).

Although the origin of such a large mass-loss rate is still unclear (Heber, 2009), hot Subdwarfs are typically found as part of binary systems (Han et al., 2002; Pelisoli et al., 2020). The significant number of Subdwarf type-B [6] stars found in close binary systems indicate their likely formation through processes involving binary interaction. Hot Subdwarf stars probably experienced mass transfer followed by common envelope ejection in a binary system during the Horizontal Branch, leaving the stellar core exposed (Green et al., 2008; Geier et al., 2010). More recent investigations support this scenario, such as the observational evidence of hot Subdwarf type-O [7] and type-B formation from the product of binary interactions (Pelisoli et al., 2020). Also, the expected evolutionary path suggests that Subdwarfs-O evolve from Subdwarfs-B (Heber, 2009).

As the two (or three) stars orbit around a common center of mass, they may not follow the evolution of isolated stars. Hot Subdwarfs evolutionary models provide insights into

[6] Subdwarf type-B: typically have strong He neutral spectral lines.

[7] Subdwarf type-O: typically have strong ionized He spectral lines.

the mechanisms of the stellar life cycles, especially binary interaction (Heber, 2009). Some adjustments are needed for core composition during this evolutionary stage, the models are widely used, limiting certain calculations.

Although the He-enriched Subdwarf-O stars cannot be explained by evolutionary models, they can connect He-deficient Subdwarf-B stars on or near the Extreme Horizontal Branch to He-deficient Subdwarf-O stars. Nevertheless, canonical models fail to explain Extreme Horizontal Branch formation due to the difficulty of removing a red Giant's entire envelope through a single mechanism (Heber, 2009, 2016).

Non-canonical models to explain the formation of Blue or Extreme Horizontal Branch stars hypothesize that the outer convective envelope penetrates the H-burning shell, mixing He into the H envelope (Heber, 2009, 2016). However, the origin of such a He mixing mechanism remains unclear.

Employing population synthesis of interacting binaries, three channels were proposed for the formation of Subdwarf-B stars (Han et al., 2002, 2003). They can evolve through one or two phases of the common envelope, stable Roche lobe overflow, or the merger of two He-core low-mass White Dwarfs.

The common-envelope channel involves the formation of Subdwarf-B stars from progenitors near the tip of the Red Giant Branch. This occurs when the Giant fills its Roche lobe, leading to dynamical mass transfer. A critical condition for the Roche lobe overflow process is a mass ratio of approximately 1.2 between the donor and the secondary stars. The resulting common envelope is formed in cases where the mass transfer rate is sufficiently high and the companion star cannot accrete all the matter. Despite these phenomena, even a detailed physical description of common-envelope evolution still shows differences in the results of mass distributions. As such, observational constraints are crucial to determine the appropriate formalism and obtain physical parameters (Heber, 2009, 2016). See the review by Heber (2009) and Heber (2016) for more details.

The close-binary evolution mechanisms are schemed in Figure 1.5. Figure 1.5.a shows two phases of mass transfer stages for binaries with small mass ratios. The first Roche-lobe overflow is stable, whereas the second one is unstable. Due to friction with the envelope, the two components spiral together until ejecting, resulting in a closer binary with an orbital period typically between 0.1 and 10 days. This binary is composed of the remnant core of the Giant, now a Subdwarf-B star, and a Main Sequence companion. Further common-

envelope phases may occur, potentially forming a White Dwarf and Subdwarf-B close binary. Figure 1.5.b illustrates the close binary evolution for initial mass ratios exceeding 1.2–1.5. In such cases, the initial phase of the mass transfer becomes unstable, leading to the ejection of the common envelope. This process gives rise to an Subdwarf-B star with a non-degenerate companion, often a Main Sequence star. Figure 1.5.c exemplifies cases where mass transfer is dynamically stable, and no common envelope forms. The companion gradually accretes material from the Roche-lobe-filling Red Giant, transforming itself into a Subdwarf-B star after the mass transfer concludes. This mechanism results in Subdwarf-B binaries characterized by Main Sequence companions and extended orbital periods ranging from 10 to 500 days. The occurrence of a second stable Roche-lobe overflow phase is not expected to significantly contribute to the Subdwarf-B population (Heber, 2009, 2016).

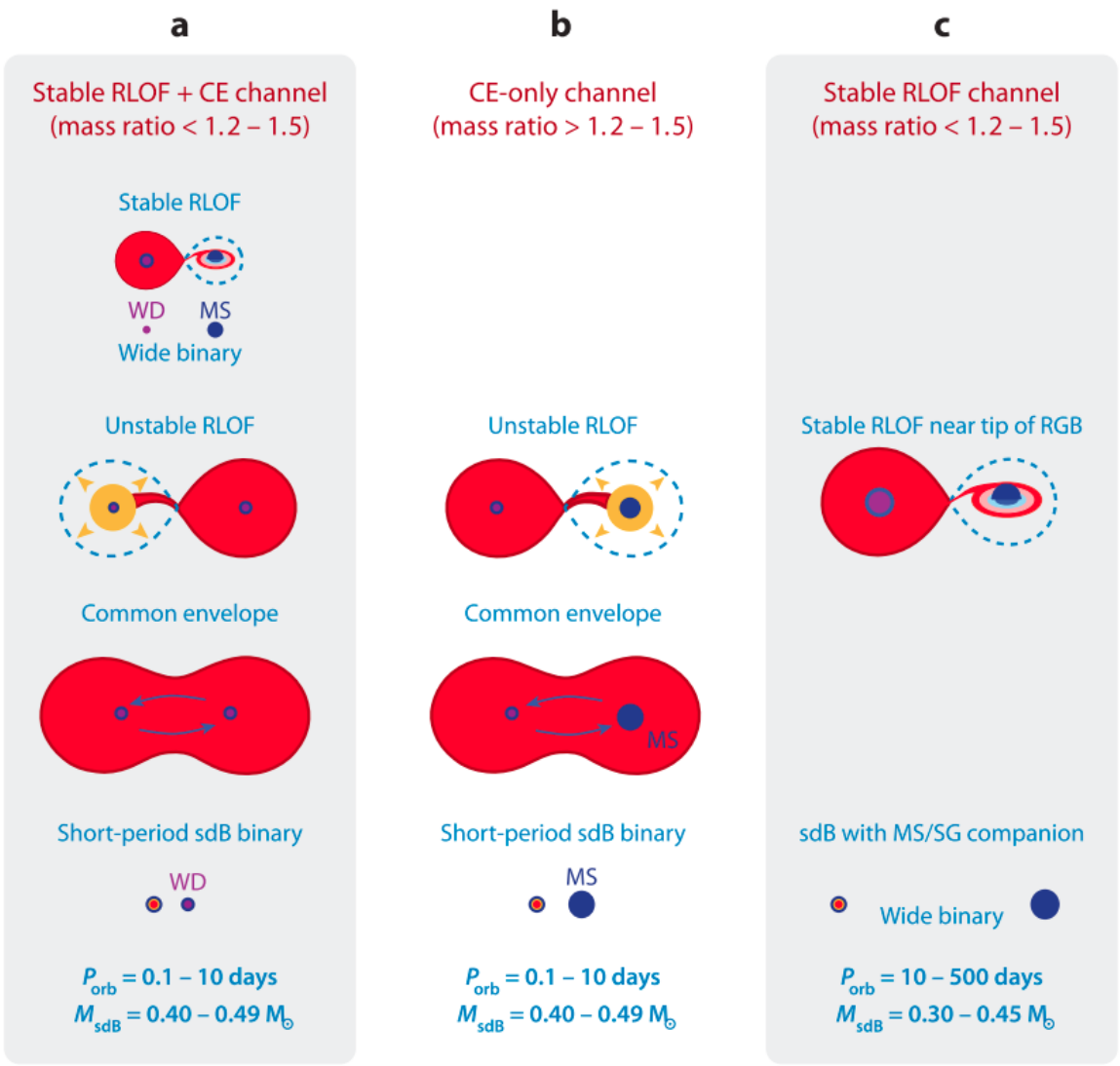

Figure 1.5: Scheme of the close-binaries Subdwarf-B formation channels evolving from top to bottom. (a) For small initial mass ratios, two phases of mass transfer to the ejection of the common envelope (CE). (b) For larger initial mass ratios the first mass-transfer phase is unstable and the common envelope is ejected. (c) For low initial mass ratios the Subdwarf-B star may also be formed in the first stable Roche-lobe overflow (RLOF). From Heber (2009); © ARA&A.

An alternative evolutionary scenario suggests that the merger of two low-mass He-core White Dwarfs might form isolated hot H-rich Subdwarfs-B (Hall and Jeffery, 2016; Schwab, 2018). Henceforth, both the hot-flasher scenario and the binary-merger scenarios remain plausible for individual Subdwarf-B and He-enriched Subdwarf-O stars. However, neither aligns perfectly with observational evidence (Heber, 2016). Also, a small fraction of Subdwarfs-B in close binaries (Wade et al., 2005) fall out of the Red Giant Branch before He ignition, perhaps because they are low-mass stars that do not support the burning of He in their cores (Heber, 2009).

1.2.5 Model atmospheres main assumptions

The atmosphere of a star is the outermost layer of its structure. A stellar atmosphere can be modeled by radiative transfer. This is represented by the second-order Equation 1.3, which relates the mean intensity (I) at a specific frequency (ν) and the source function, which is the ratio between the total emission coefficient (η) and the total absorption (α) coefficients. The equation is solved through the optical depth (τ) from the bottom to the top along the normal of a plane-parallel atmosphere

$$\frac{\partial^2(f_\nu I_\nu)}{\partial^2 \tau_\nu} = I_\nu - \frac{\eta_\nu}{\alpha_\nu} \tag{1.3}$$

The radiative transport in a layer of the stellar atmosphere is schematically shown in Figure 1.6.

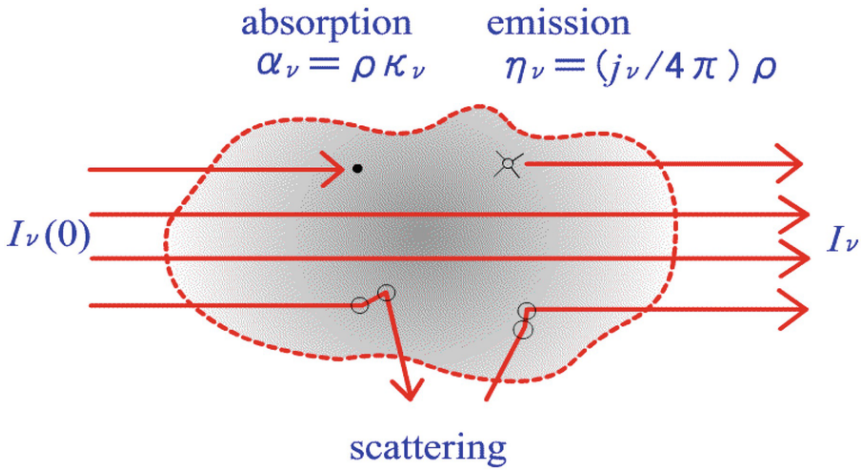

Figure 1.6: Radiative transport in a layer of the stellar atmospheres. From Kato and Fukue (2020); © Springer Nature Singapore.

The stellar model assumes hydrostatic equilibrium, in other words, the total pressure (gas + radiation + turbulent) balances the gravity (Hubeny and Mihalas, 2014). The energy balance is given by the radiative equilibrium equation in stable layers. Energy conservation is also assumed in the convective unstable atmospheres, where the radiative gradient is greater than the adiabatic gradient (Hubeny, 1988; Hubeny and Lanz, 2017a).

The majority of atmosphere models (Kurucz, 1994; Castelli and Hubrig, 2004; Gustafsson et al., 2008, e.g.) are built adopting local thermodynamic equilibrium (LTE), which is considering the Saha-Boltzmann statistics equilibrium (Hubeny and Mihalas, 2014). As a simplification, all layers of the atmosphere structure are ruled by the same local

temperature (kinetic ion temperatures, excitation temperature, ionization temperature), which means thermodynamic equilibrium. In this case, the local temperature is the only parameter that defines the partition energy in the atmosphere. This assumption is acceptable for atmospheres such as those in the range of $5\,500 \leq T_{\rm eff}[K] \leq 20\,000$ and $2.0 \leq \log g \leq 5.0$, typical of Horizontal Branch stars.

As LTE assumptions have approximations, the models may differ significantly from the realistic statistical equilibrium. The atomic transitions would be trapped by the high opacity at the line center and can be redistributed into a line's wings. The opacity is composed of the contributions of the extinction (bound-bound, bound-free, and free-free transitions) and the scattering (electrons and Rayleigh) as absorption coefficients (Hubeny and Lanz, 2017a). Non-local thermodynamic equilibrium (NLTE) assumptions are required to build hotter models, producing a difference in the line-core photons absorbed and emitted at specific physical depths (Hubeny and Mihalas, 2014).

In the NLTE case, it is implied that the assumption of LTE fails and the populations are now permitted to differ from the local Saha-Boltzmann equilibrium values. The mass density as well as electron density have influenced the solution of the radiation field transferred from the bottom to the top of the atmosphere. Models with more sophisticated physics, in which the kinetic equilibrium is based on the quantum statistics of NLTE, better represent a variety of atmosphere conditions, depending on temperature, density, and abundances (Hubeny and Mihalas, 2014).

In NLTE models, each explicit atomic, ionic, and molecular level population influences other particles in the gas to solve the kinetic equilibrium equation (Hubeny and Lanz, 2017a). The opacities are computed in detail from atomic data at the beginning of the iterations and re-evaluated afterward (Hubeny and Lanz, 2017b), by considering small frequency steps to sample the lines. The populations may depend on other transitions and therefore a given transition of interest may be influenced by many others in the same particle species, or by transitions in other atoms and molecules if these possess overlapping frequencies (Rutten, 2003).

Considerable improvements in NLTE atmosphere models have been achieved over the last five decades. The first NLTE spectra of hot atmospheres in the early 1970s (Mihalas and Hummer, 1974) were built based on pure H atmosphere structures, and the metal lines were considered only in the spectral synthesis. Analysis by Lanz and Hubeny (1995)

took H, C, and Fe into account for the opacity of hot and high-gravity NLTE atmosphere models. They found critical differences in effective temperature determinations and line profiles arising from the inclusion of explicit atomic species (i.e. with the kinetic equilibrium equation solved) in the atmospheric structure. The hot Subdwarfs' atmospheres have more evident NLTE effects due to their lower surface gravities (when compared to White Dwarfs; Lanz et al. 1997). They built spectra considering line blanketing with H/He, CNO, Si, Fe, and Ni as implicit ions and concluded that this approach significantly improved the line profile analysis. Hubeny et al. (1998) showed that NLTE metal-line-blanketing effects produce a conspicuous difference (typically up to 20%) in the line profiles seen in the ultraviolet spectra of hot White Dwarfs. By considering explicit metal ions such as H/He, CNO, Si, and Fe in the atmosphere structure a better emergent flux match was achieved.

It is ideal to have homogeneous and widely available model spectra for the stellar atmospheres to improve our knowledge of their fundamental physical parameters and evolution. Such models should be computed as detailed as possible regarding the radiative transfer, considering non-local thermodynamic equilibrium (NLTE), and fully line-blanketed atmosphere structures (Lanz and Hubeny, 1995; Lanz et al., 1997).

NLTE atmosphere structures and hot Subdwarf spectra were calculated by Németh et al. (2014), covering specific temperature ($20\,000 \leq T_{\rm eff}[{\rm K}] \leq 56\,000$) and gravity ranges ($5.0 \leq \log g[(cgs)] \leq 6.3$). The opacities of H, He, and a few metal ions were included to compute the atmosphere structure in these models. However, only a small and nonhomogeneous collection of detailed hot Subdwarf model spectra was available. High-temperature spectral grids may also be calculated by other codes, e.g. the Tübingen NLTE Model Atmosphere package (Rauch et al., 2018)[8].

Our developments in stellar atmosphere models are presented in Chapter 2. We will present an extensive high-spectral-resolution grid of NLTE synthetic spectra for hot Subdwarfs from the infrared to the ultraviolet. In Chapter 3 we are going to present an application on the study of hot Horizontal Branch stars in the analysis of the globular clusters NGC 2808 and NGC 7089.

[8] `http://dc.zah.uni-heidelberg.de/theossa/q/web/form`

1.3 Motivation

Studying galaxy evolution involves complexities tied to assumptions about stellar populations, stellar evolution models, and unknown factors. Challenges arise from considerations like mass loss, convection, and choices such as stellar spectra, wavelength coverage, and resolution. Simulating integrated spectra across wavelengths provides insights into globular cluster properties and enhances our understanding of the chemical enrichment history, formation, and evolution of our Galaxy. Testing these methods on resolved Galactic systems is essential for accurately reproducing their properties. This multidisciplinary approach not only serves as a vital tool but also holds potential implications for understanding other galaxies. Furthermore, it contributes to explaining the evolution of ultraviolet light in such systems over time, extending its relevance to high-redshift elliptical galaxies.

It has been known that good reproduction of integrated stellar systems requires the inclusion of hot low-mass stars, rare phases which are not yet well described by isochrones. Attempts at studying their contribution exist in literature, but recent advances in modern theoretical libraries open an opportunity to revisit this debate.

1.4 Goals

The main goal of this thesis is to investigate how evolved hot high-gravity stars brighter than the turn-off improve the modeling of the integrated spectrum of Galactic old stellar populations. Ultimately, we intend to answer the question: How much do hot low-mass stellar components contribute to the integrated spectrum of the old stellar population?

The outcomes of this research are to improve stellar population synthesis models, infer ages more reliably, and break the degeneracy between age and Horizontal Branch morphology. As an extragalactic motivation, it is possible to apply this method to study unresolved sources, such as dwarf galaxies or globular clusters in the local Universe.

Chapter 2

Modeling spectra of Subdwarfs

This Chapter provides details of producing stellar atmosphere models and synthetic spectra of Subdwarfs, based on the publications by Pacheco et al. (2021, 2023), and explores the key outcomes of this research. The complete grid is available on our SpecModel website [1] as well as on the SVO's Theoretical Spectra Web Server [2] and the Vizier [3] databases.

2.1 Atmosphere models

The Pacheco et al. (2021) grid of 96 Subdwarf-structure models is composed of eight effective temperatures ($T_{\rm eff}$: 10,000, 15,000, 20,000, 25,000, 30,000, 35,000, 45,000, and 65,000 K), each one computed in three surface gravities ($\log g$ [cgs]: 4.5, 5.5, and 6.5) and four different chemical abundances: solar and He-rich, solar and He-poor, halo and He-rich, halo and He-poor. Moreover, in Pacheco et al. (2023), we computed a new set of 54 models with three more effective temperatures ($T_{\rm eff}$: 17,500, 22,500 and 27,500 K), three surface gravities ($\log g$ [cgs]: 4.5, 5.0, and 5.5) and the same four chemical abundances.

The atmosphere structure models were computed by `TLUSTY` code v205 and v208 (for convective 10,000 K models; Hubeny 1988; Hubeny and Lanz 2011b). It calculates a self-consistent solution of the equations describing the radiative (or radiative plus convective) transfer and physical state of the atmosphere. The geometry of the model is plane-parallel with homogeneous chemical abundances (Hubeny and Lanz, 1995).

The most popular Subdwarf models available have been built in LTE. In LTE, all energy partitioning, such as atomic, ionic, and molecular level populations, is given by

[1] Spectral Models of Stars and Stellar Populations, `http://specmodels.iag.usp.br/`.

[2] Spanish Virtual Observatory, `http://svo2.cab.inta-csic.es/theory//newov2/`.

[3] Vizier, `https://vizier.u-strasbg.fr/viz-bin/VizieR`

Saha-Boltzmann equations, being defined by the local temperature. The LTE conditions may differ from those derived in actual statistical equilibrium; therefore, level populations in NLTE were calculated. Departures from LTE may be especially significant for high-temperature Subdwarf atmospheres (Hubeny and Lanz, 1995; Lanz and Hubeny, 1995; Lanz et al., 1997) as also found in DA-type WD atmospheres (Levenhagen et al., 2017).

The starting point was to compute an LTE gray structure model, which is then used as an input to build the NLTE line-blanketed models (Hubeny, 1988; Hubeny et al., 1994). We considered H, He, C, N, O, Ne, Mg, Al, Si, S, and Fe as explicit ions (see Table 2.1) contributing to the opacity. The set of ionization states for the selected atomic species was chosen based on ionization energies, model-effective temperatures, and candidate-permitted transitions from **?**. The atomic data of each ion included as an explicit species in the NLTE atmosphere models are summarized in Table A.1 (see details in Lanz and Hubeny 2003, Lanz and Hubeny 2007).

Table 2.1 - Explicit species included in the NLTE atmosphere models.

	Effective Temperature [10^3K]										
Ions	10.0	15.0	17.5	20.0	22.5	25.0	27.5	30.0	35.0	45.0	65.0
H^-	✓	✓	✓	✓							
H	✓	✓	✓	✓	✓	✓	✓	✓	✓	✓	✓
He	✓	✓	✓	✓	✓	✓	✓	✓	✓	✓	✓
He II	✓	✓	✓	✓	✓	✓	✓	✓	✓	✓	✓
C	✓	✓	✓	✓	✓	✓					
C II	✓	✓	✓	✓	✓	✓	✓	✓	✓	✓	✓
C III	✓	✓	✓	✓	✓	✓	✓	✓	✓	✓	✓
C IV						✓	✓	✓	✓	✓	✓
N	✓	✓	✓	✓	✓	✓					
N II	✓	✓	✓	✓	✓	✓	✓	✓	✓	✓	✓
N III	✓	✓	✓	✓	✓	✓	✓	✓	✓	✓	✓
N IV						✓	✓	✓	✓	✓	✓
N V						✓	✓	✓	✓	✓	✓
O	✓	✓	✓	✓	✓	✓					
O II	✓	✓	✓	✓	✓	✓	✓	✓	✓	✓	✓

Table 2.1 - Continued. Explicit species included in the NLTE atmosphere models.

	Effective Temperature [10^3K]										
Ions	10.0	15.0	17.5	20.0	22.5	25.0	27.5	30.0	35.0	45.0	65.0
O III		✓	✓	✓	✓	✓	✓	✓	✓	✓	✓
O IV						✓	✓	✓	✓	✓	✓
O V						✓	✓	✓	✓	✓	✓
Ne	✓	✓	✓	✓	✓	✓					
Ne II	✓	✓	✓	✓	✓	✓					
Ne III						✓	✓	✓	✓	✓	✓
Ne IV						✓	✓	✓	✓	✓	✓
Mg II	✓	✓	✓	✓	✓	✓	✓	✓	✓	✓	✓
Al II	✓	✓	✓	✓	✓	✓	✓	✓	✓	✓	✓
Al III	✓	✓	✓	✓	✓	✓	✓	✓	✓	✓	✓
Si II	✓	✓	✓	✓	✓	✓					
Si III	✓	✓	✓	✓	✓	✓	✓	✓	✓	✓	✓
Si IV		✓	✓	✓	✓	✓	✓	✓	✓	✓	✓
S II	✓	✓	✓	✓	✓	✓					
S III	✓	✓	✓	✓	✓	✓	✓	✓	✓	✓	✓
S IV		✓	✓	✓	✓	✓	✓	✓	✓	✓	✓
S V						✓	✓	✓	✓	✓	✓
S VI										✓	✓
Fe II	✓	✓	✓	✓	✓	✓					
Fe III	✓	✓	✓	✓	✓	✓	✓	✓	✓	✓	✓
Fe IV		✓	✓	✓	✓	✓	✓	✓	✓	✓	✓
Fe V						✓	✓	✓	✓	✓	✓
Fe VI						✓	✓	✓	✓	✓	✓

The structure models are susceptible to chemical abundances via opacities, electron, and mass densities. The explicit atoms and ions included to compose the level and super levels are the essential ingredients to compute detailed NLTE structure models. They

impact the cross-section computation, justifying the careful choice of the most important ions for each model.

As described by Lanz and Hubeny (2007), the LTE fluxes are about 10% higher than the NLTE predictions, which is most noticeable in the near-UV. Lanz and Hubeny (2007) also mentioned that the lower NLTE fluxes of hot stellar atmosphere models result from the overpopulation of the H I ($n = 2$) level at the depth of formation of the continuum flux. Hence implying a more considerable Balmer continuum opacity.

The adopted abundances are expressed as solar ([Fe/H] = 0.0; Asplund et al. 2009) or Galactic halo ([Fe/H] =-1.5 and [α/Fe] = +0.4) as well as He-rich (Edelmann et al., 2003) and He-poor abundances (Németh et al., 2012; Lei et al., 2019a). The He over H ratios follow the fitting formulas 1.1 and 1.2 described in the previous Chapter. Our choice of solar and halo metallicity is not intended to describe Subdwarf typical abundances. Instead, these solar and halo points set a broad Z range, probing its effect on the continuum and line profiles. It is well established that atmospheric Subdwarf metal abundances have little or virtually no memory of their parent main sequence surface abundances (e.g. Moehler, 2001; Németh et al., 2012; Byrne et al., 2018). Metals at the Subdwarf surface vary greatly depending on previous binary evolution and diffusion processes, leading to diverse abundance patterns (e.g., O'Toole and Heber 2006) with loose observational constraints. He-rich and He-poor abundance variations were chosen based on linear fits as a function of temperature based on Lei et al. (2019a) (see Table 2.2). Note that `TLUSTY` (Hubeny, 1988; Hubeny and Lanz, 2011b) uses the solar chemical abundances as defined by Grevesse and Sauval (1998) as default values, and we rearranged all the chemical species to the solar abundance as defined by Asplund et al. (2009). The atmosphere structures (available upon request to the authors) may be interpolated in metallicity and specific modified metal abundances used in custom spectral synthesis.

The time spent on computational work increases, and the convergence is more difficult when the complexity of the heavy elements is included in the `TLUSTY` atmosphere code (Hubeny, 1988; Hubeny and Lanz, 2011b). As a reference, each one of the 96 structures was computed and analyzed in a typical time scale of a day.

Table 2.2 - Numerical He Abundances.

$T_{\rm eff}$[K]	$\log(n_{\rm He}/n_{\rm H})$ poor	$\log(n_{\rm He}/n_{\rm H})$ rich
10 000	-4.98	-3.81
15 000	-4.35	-3.13
17 500	-4.05	-2.80
20 000	-3.72	-2.46
22 500	-3.41	-2.12
25 000	-3.09	-1.78
27 500	-2.78	-1.45
30 000	-2.46	-1.11
35 000	-1.83	-0.43
45 000	-0.57	0.92
65 000	1.95	3.62

The broadening of lines was treated carefully considering the Lyman and Balmer line profile tables from Tremblay and Bergeron (2009). The high-frequency limit for lines that are taken into account in the opacity sampling was set to $6 \times 10^{11} \times T_{\rm eff}$ or the highest bound-free edge frequency, if greater. Opacity-sampling steps smaller than the thermal broadening were set. The microturbulent velocity was set to 10 km s^{-1}. The opacity-sampling approach was used to compute the superline cross-sections with better accuracy. Also, the iron peak lines were treated in a line-blanketed model.

The only exception to the description above was the atmosphere models with 10,000 K, which require a convective treatment (Fontaine et al., 1981; Bergeron et al., 1992); a mixing-length theory parameter equal to the pressure-scale height ($\alpha_{\rm MLT} = 1.0$) was used. For the 10,000 K case, the final structure model was computed in LTE without a microturbulent velocity.

Most models were computed using the hybrid complete-linearization and accelerated lambda-iteration (CL/ALI) method (Hubeny and Lanz, 1995; Hubeny, 2003), which is the default procedure for computing fully consistent, NLTE metal-line-blanketed atmosphere models in `TLUSTY` (Hubeny, 1988). When the convergence was not achieved directly from CL/ALI, we computed the atmosphere structure models using the Rybicki scheme (Hubeny and Mihalas, 2014), which is also suitable for treating high-temperature and high-gravity atmospheres, with better convergence behavior in some cases.

The effective temperature as a function of the mass depth is shown in Figure 2.1. The

structure models in Figure 2.1 have a surface gravity ($\log g$) equal to 4.5. The outermost mass depth corresponds to the Rosseland optical depth $\tau = 10^{-7}$ while the innermost depth has $\tau = 100$, logarithmically sampled in 70 layers. The color-bar scale indicates the effective temperature from the bottom 10,000 K in yellow to the top 65,000 K in purple. The hottest structures are more extended toward the inner thick region than the cooler model. The dotted lines represent the starting model computed using LTE assumptions, where we can see the almost isothermal behavior in the external region for models with different effective temperatures. On the other hand, the dashed lines represent the structure computed using the NLTE assumptions and line blanketing of the explicit species. In the latter, a slight temperature inversion on their outer regions can be seen in some cases, which is important to the line-core profile formation. The inner region converges to the solution with minor differences if we compare the LTE and NLTE structures when mass depths are shown. If we look at a specific line optical depth, the differences between LTE and NLTE structure models are much more significant.

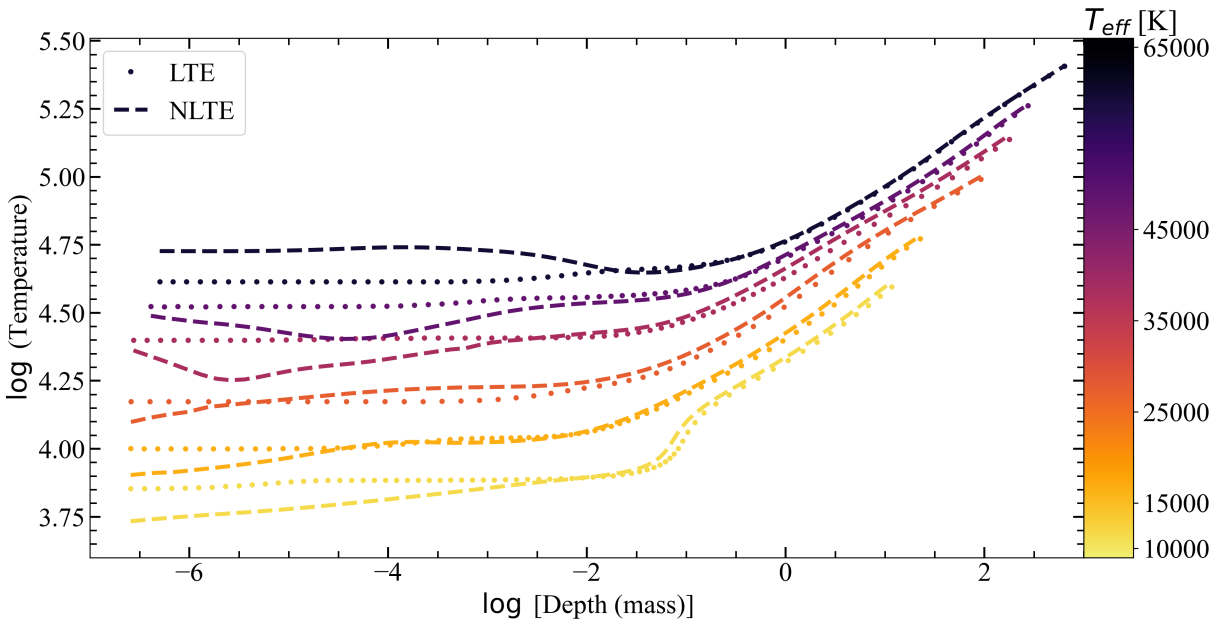

Figure 2.1: Structure models of the temperature [K] as a function of mass depth [g cm^{-2}] in a logarithmic scale computed using LTE (dotted lines) and NLTE (dashed lines) assumptions. The effective temperatures are shown in the colored scale from bottom (10,000 K) to top (65,000 K). These models have solar and He-rich abundances and $\log g$ [cgs] = 4.5. From Pacheco et al. (2021).

Figure 2.2 also shows the effective temperature as a function of the mass depth and it has the same color-bar scale as in Figure 2.1. The structure models in Figure 2.1 have a surface gravity ($\log g$) equal to 6.5, representing a more compact object. In this case, the

atmosphere structure is less extended if compared to Figure 2.1.

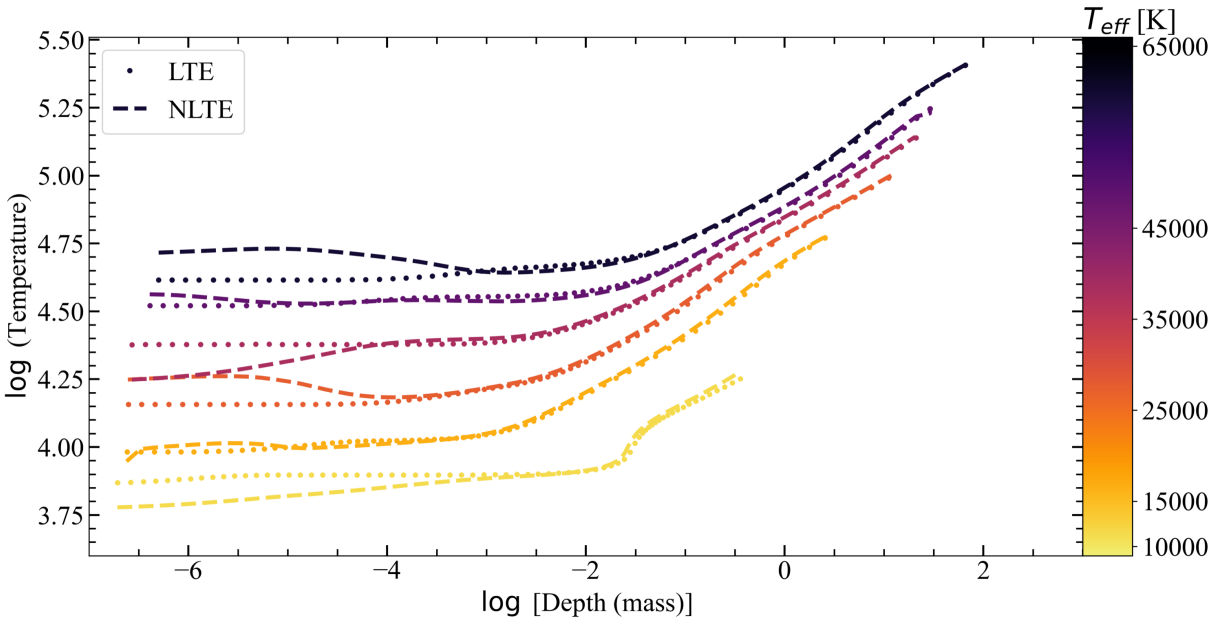

Figure 2.2: Structure models of the temperature [K] as a function of mass depth [g cm^{-2}] in a logarithmic scale computed using LTE (dotted lines) and NLTE (dashed lines) assumptions. The effective temperatures are shown in the colored scale from bottom (10,000 K) to top (65,000 K). These models have a halo and He-rich abundances and $\log g$ [cgs] = 6.5. From Pacheco et al. (2021).

The electron and mass densities are shown in Figure 2.3, having a similar profile as a function of the mass depth. The effects of surface gravity on the atmospheric height are evident. The cooler structure models, such as the example of 10,000 K in Figure 2.3 a) and b) have an inversion on the density profiles near log [Depth (mass)] = −1, this is due to the effect of convection that was considered for these specific temperatures. As the example of 65,000 K in Figure 2.3 c) and d), the hot structure models have densities with a power-law dependency on the mass depth.

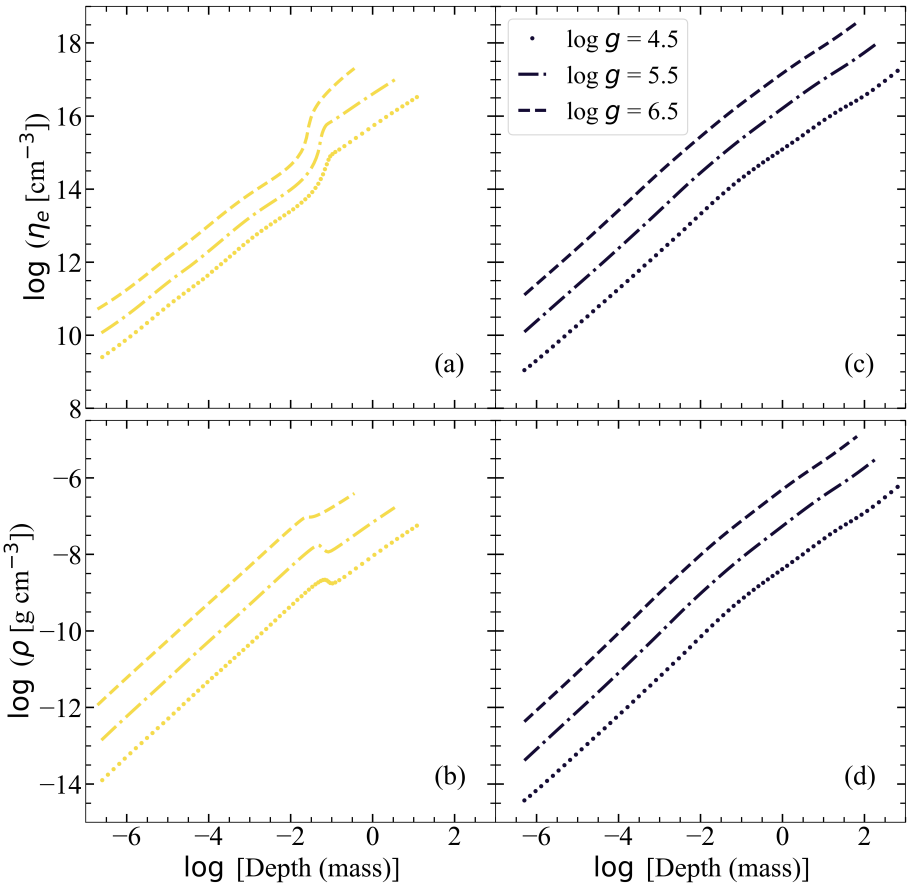

Figure 2.3: Structure models of the electron density (top) and mass density (bottom) as a function of mass depth [g cm^{-2}] in a logarithmic scale. We are comparing different surface gravity models computed using NLTE assumptions. These models have halo and He-rich abundances. a), b) $T_{\rm eff}$ = 10,000 K; c), d) $T_{\rm eff}$ = 65,000 K. From Pacheco et al. (2021).

An Inglis-Teller diagram for the grid was produced, which is a classical tool for evaluating model sequences' behavior over a gravity range. It involves the electron density (η_e) and the maximum N level that originates a distinguishable Balmer absorption line, which helps diagnose our model's quality. We interpolated the model electron density to a specific optical depth $\tau = 0.1$, counting the highest visible term in the final synthetic spectra. The linear regression has a slope -4.64. A linear least-squares fit of the electron density and the maximum number of the absorption lines near the Balmer's discontinuity is shown in Figure 2.4.

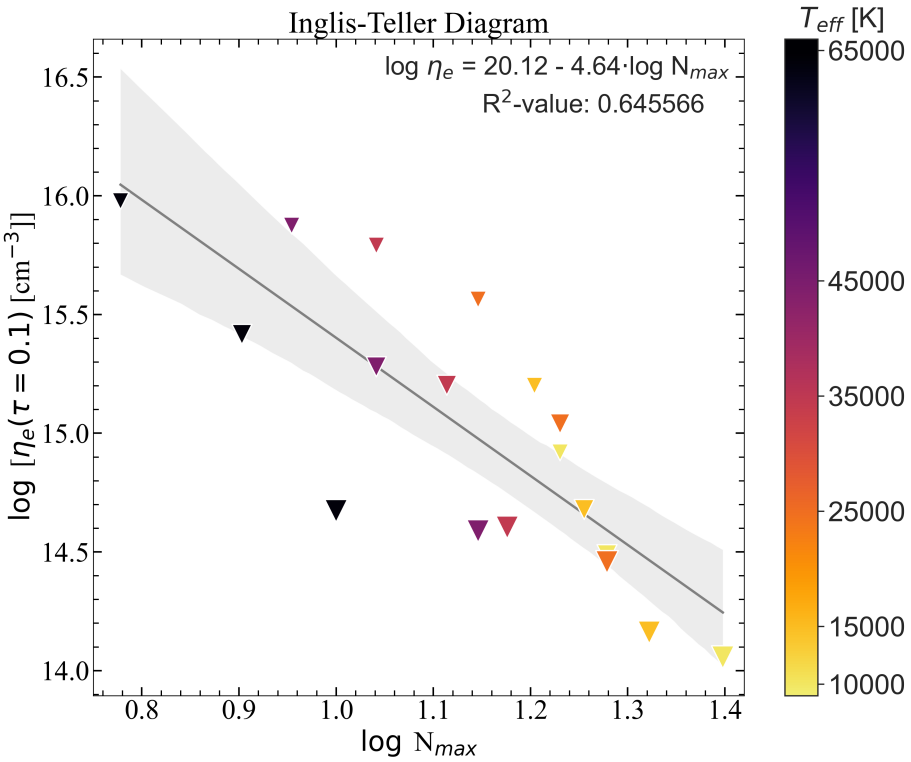

Figure 2.4: An Inglis-Teller diagram of models with halo and He-rich abundances. It shows the electron density (η_e) as a function of the maximum N level that originates a distinguishable Balmer absorption line. The color-bar scale is the same as in Figures 2.1 and 2.2. The bigger symbols represent the surface gravity ($\log g$) equal to 6.5 and the smaller symbols represent the surface gravity ($\log g$) equal to 4.5. The black line is the linear regression with a slope -4.64 and the grey area is the dispersion. From Pacheco et al. (2021)

We also performed convergence analyses for all the 144 Subdwarf-structure models computed. The most critical convergence criterion is the magnitude of the relative changes of the components of the state vector, which is defined as a set of all structural parameters (e.g., temperature, particle number densities, and the mean radiation intensities in discretized frequency points) in a given discretized depth point (Hubeny and Lanz, 2011b). The necessary condition for convergence is that the maximum relative change of all state vector components in all 70 depths is smaller than 10^{-3}. However, a supplementary condition is the conservation of the total flux concerning the total theoretical flux, $\sigma \mathrm{T_{eff}}^4$. The output parameters such as the number of depths, column mass, temperature, and densities in each depth and relative changes between iterations are used in the convergence analysis, as well as in the emergent flux in all frequency points used by the `SYNSPEC` code (Hubeny and Lanz, 2011a) to build synthetic spectra.

Figure 2.5 shows the structure convergence for the model with $\mathrm{T_{eff}} = 45\,000$K, $\log g =$

5.5, and halo and He-poor abundances, as a relative change of temperature (upper) and maximum in state vector (bottom). The two left panels show the relative change as a function of column mass. The colors represent the iterations until number 27 (in pink and black dashed lines), the converged model with the lowest relative change in the state vector. The middle panels also show the relative change in the log scale following the same color pattern, with the lower pink line overlapped by the black dashed line representing the converged model. The right panels show the maximum relative change in the logarithmic scale of the state vector decreasing up to 10^{-3} after 27 iterations. The dominant change in the maximum state vector is the particle number density.

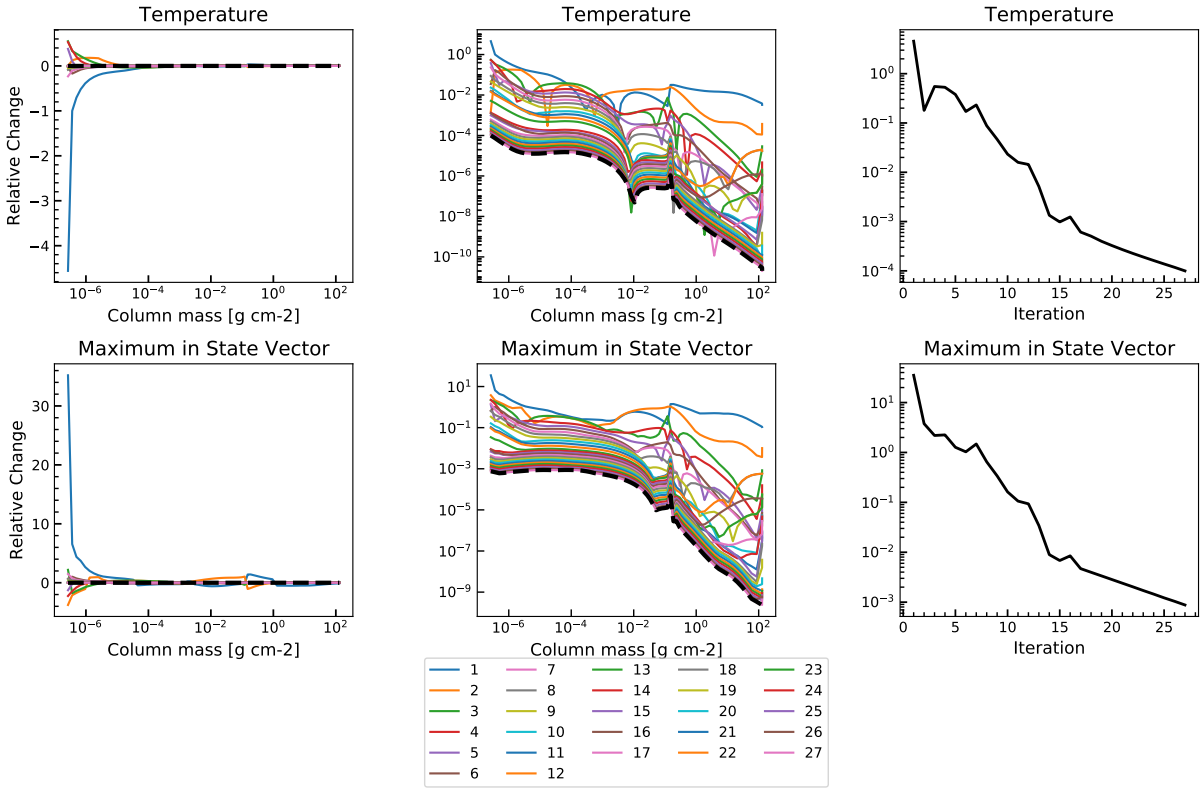

Figure 2.5: The convergence of a structure model with $T_{\rm eff} = 45\,000$K, log$g = 5.5$ and halo and He-poor abundances show the relative change of temperature (upper) and maximum in state vector (bottom). *Left*: the linear relative change as a function of column mass. *Middle*: the relative change in log scale as a function of column mass for each one of the 27 iterations. The black dashed line represents the relative change in the converged structure model. *Right*: the relative change in log scale as an iteration function.

The output parameters such as the number of depths, column mass, temperature, and densities in each optical depth and relative changes between iterations are used in the convergence analysis, as well as the emergent flux in all frequency points is used by the

SYNSPEC code (Hubeny and Lanz, 2011a) to build synthetic spectra, as described below.

2.2 Synthetic spectral models

We computed the grid of synthetic spectra with the SYNSPEC code designed to synthesize the emergent spectra from atmosphere model structures. We used the NLTE atmosphere structure from TLUSTY models (Hubeny, 1988; Hubeny and Lanz, 2011b) described in Section 2.1. We considered NLTE assumptions for the evaluation of the level and superlevel populations. The reference atomic line list is Coelho (2014), based on Coelho et al. (2005) and line lists from R. Kurucz [4] and F. Castelli [5] (see, e. g. Kurucz 2017; Castelli and Hubrig 2004.

The hydrogen and hydrogenic lines are treated as a part of the continuum, and their profiles are computed using tables from Tremblay and Bergeron (2009). The quasi-molecular satellites of Lα, Lβ, and Hα (λ = 1 215.67, 1 025.18 and 6 562.79 Å, respectively), are considered. In that case, additional input files containing the corresponding data were used (Allard et al., 2009).

The four He I triplet lines, (λ = 4 026, 4 387, 4 471, and 4 921 Å) were treated using special line-broadening tables (Barnard et al., 1974; Shamey, 1969). The He II lines are treated as the approximate hydrogenic ion by analytical values of the Stark + Doppler profile (Hubeny et al., 1994), which improves the accuracy of the line profile for $T_{\rm eff}$ > 10 000 K, and the line profiles are given by the Stark-broadening tables of Schöning and Butler (1989). Also, we considered Stark broadening computed by Tremblay and Bergeron (2009).

The spectral grid coverage is between 1 000 – 10 000 Å with steps of 0.01 Å. The resulting spectrum was subsequently processed with the ROTIN code (Hubeny and Lanz, 2011a), which resamples the original synthetic spectrum with no rotational velocity and no instrumental degradation considered.

We show the normalized emergent flux (in arbitrary units) given as a function of wavelength for the spectral coverage from 1 000 to 9 000 Å in Figure 2.6. A forest of lines is seen in this particular sampling, where no instrumental degradation is included. They are synthetic spectra with $T_{\rm eff}$ equal to 65 000, 45 000, 35 000, 30 000, 25 000, 20 000,

[4] http://kurucz.harvard.edu/linelists.html

[5] http://wwwuser.oats.inaf.it/castelli/linelists.html

15 000, and 10 000 K (from top to bottom) and $\log g$ [cgs] = 5.5 with halo and He-rich abundances (see equation 1.1).

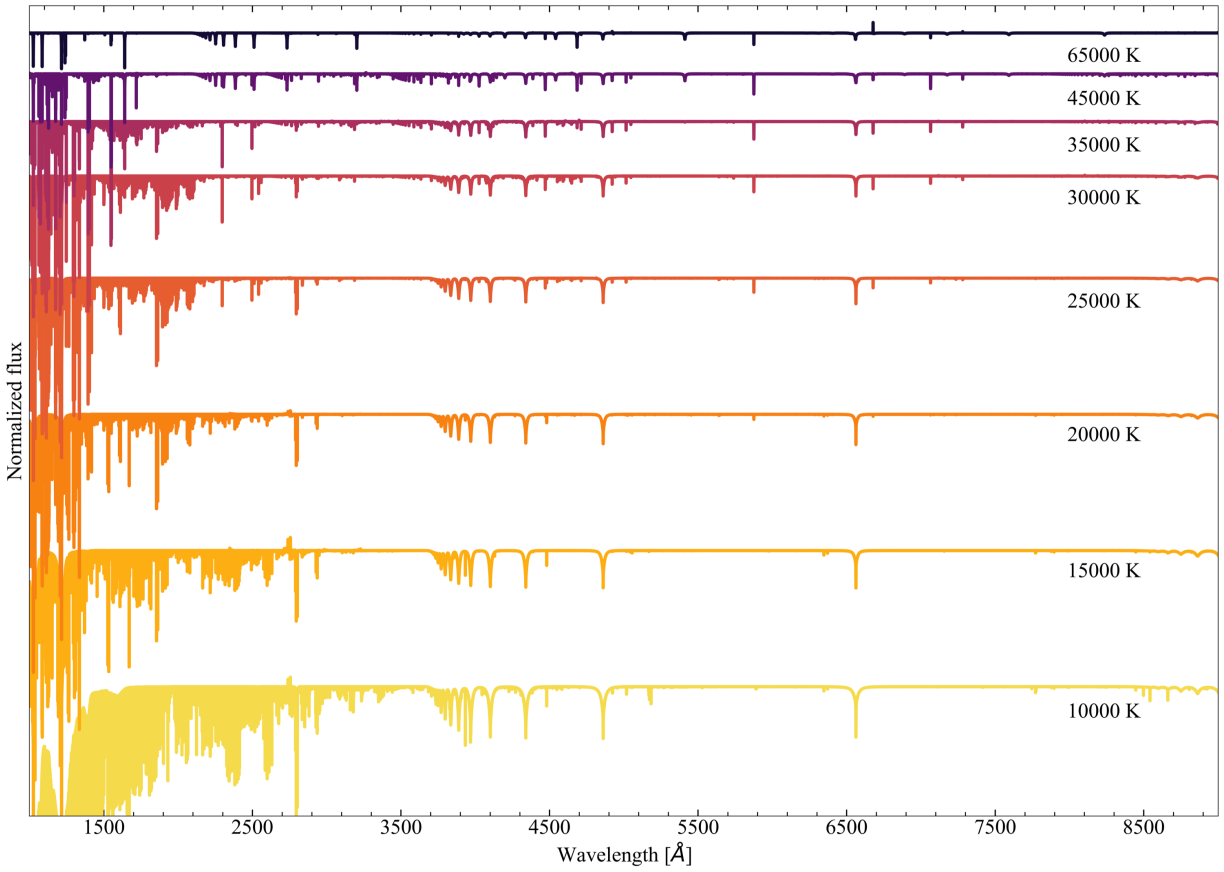

Figure 2.6: Sample spectra with coverage from 1 000 – 9 000 Å without instrumental broadening for different temperatures from top (65 000K) to bottom (10 000K), $\log g$ [cgs] = 5.5 with halo and He-rich abundances. From Pacheco et al. (2021).

In Figure 2.7, we can compare the different spectral types in the near-UV region between 1 000 and 2 000 Å, where for the visual effect, it is degraded to a Gaussian instrumental profile with full width at half maximum (FWHM) equal to 5 Å. The hotter spectra have a bluer continuum, and the He lines dominate. The Stark broadening is more evident on the cooler spectra, where a stronger Lyman series is present, besides its quasi-molecular absorption features.

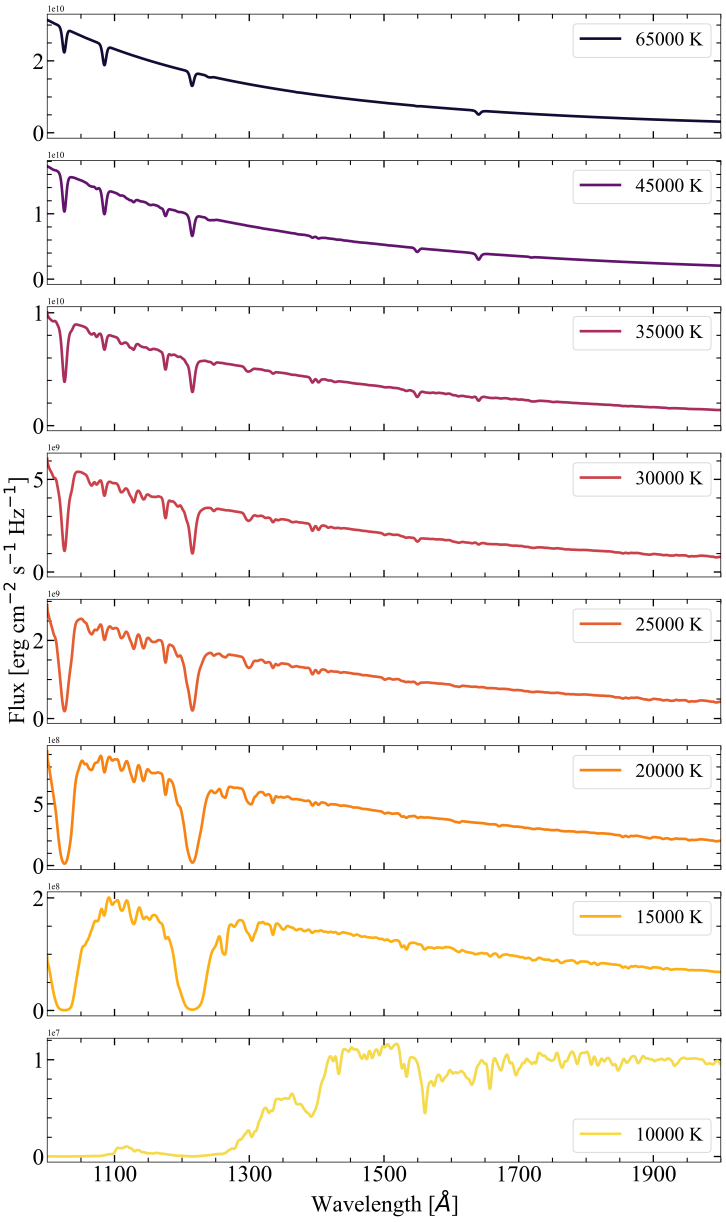

Figure 2.7: Sample spectra in the UV region (1 000 – 2 000 Å) with FWHM resolution = 5 Å for different temperatures: from top (65 000K) to bottom (10 000K), and $\log g$ [cgs] = 5.5 with halo and He-rich abundances. From Pacheco et al. (2021).

In Figure 2.8, we can compare the different spectral types on the Balmer break region between 3 500 – 6 750 Å, where for visual effect, the resolution is degraded by a Gaussian instrumental profile with FWHM equal to 5 Å. As expected, the H is mostly ionized, and the Balmer series is weaker in the hotter spectra. The cool models are not favorable to the formation of strong He lines. Moreover, the spectra presented in Figure 2.8 follow the He-abundance sequence from Németh et al. (2012), which shows low He abundance even for the He-rich sequence of cool Subdwarfs.

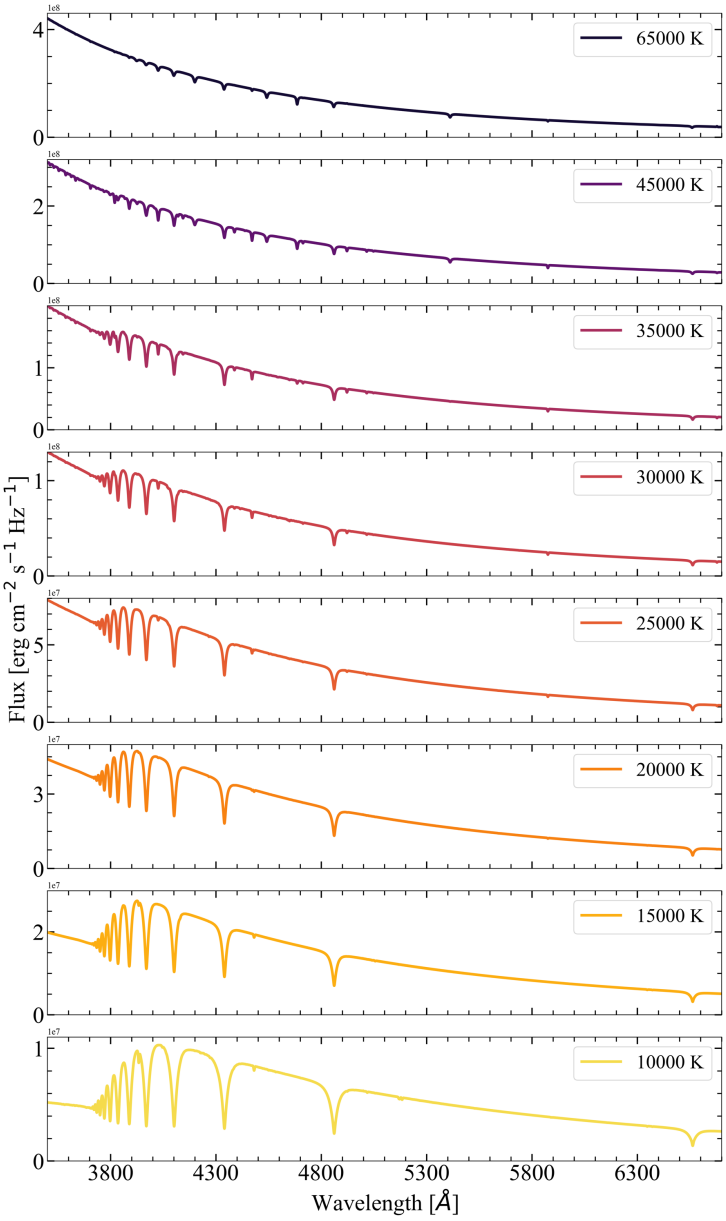

Figure 2.8: Sample spectra in the optical region (3 500 – 6 750 Å) with FWHM resolution = 5 Å for different temperatures: from top (65,000K) to bottom (10,000K), and $\log g$ [cgs] = 5.5 with halo and He-rich abundances. From Pacheco et al. (2021).

To illustrate the grid, we present a simple comparison of model spectra with the spectra of the Lamost 442708048, Lamost 183405148, and HD 4539 Subdwarfs (see Figures 2.9 and 2.10). No interpolation in the grid was performed, as the intent was not to determine exact abundances or stellar parameters but rather to exhibit the grid potentialities. The targets were selected from the Subdwarf catalog in Lei et al. (2019a) and Hubble Space Telescope's (HST)/Space Telescope Imaging Spectrograph (STIS) Legacy Archive data. They are located in the solar neighborhood.

According to Lei et al. (2019a), the target Lamost 442708048 has $T_{\rm eff}$ = 26 620±70 K, $\log g$ = 5.53±0.01 [cgs], log (n_{He}/n_H) =-2.78±0.05, $E(B-V)$ = 0.018 and, from the Gaia Collaboration et al. (2018) parallax, its distance is 317±5 pc. We performed a comparison with models near these values, within the boundaries of our grid, as $T_{\rm eff}$ = 25 000 K, $\log g$ = 5.5 [cgs], [Fe/H] = 0, and log (n_{He}/n_H) =-3.09 (see Figure 2.9 (a)). Lamost 183405148 has, according to Lei et al. (2019a), $T_{\rm eff}$ = 46 270±330 K, $\log g$ = 5.88±0.04, log (n_{He}/n_H) = 0.29±0.01, $E(B-V)$ = 0.021, and from its parallax (Gaia Collaboration et al., 2018) the distance is 333±9 pc. The closest model spectrum adopted corresponds to $T_{\rm eff}$ = 45 000 K, $\log g$ = 5.5 [cgs], [Fe/H] = 0, and log (n_{He}/n_H) = 0.92 (see Figure 2.9 (b)).

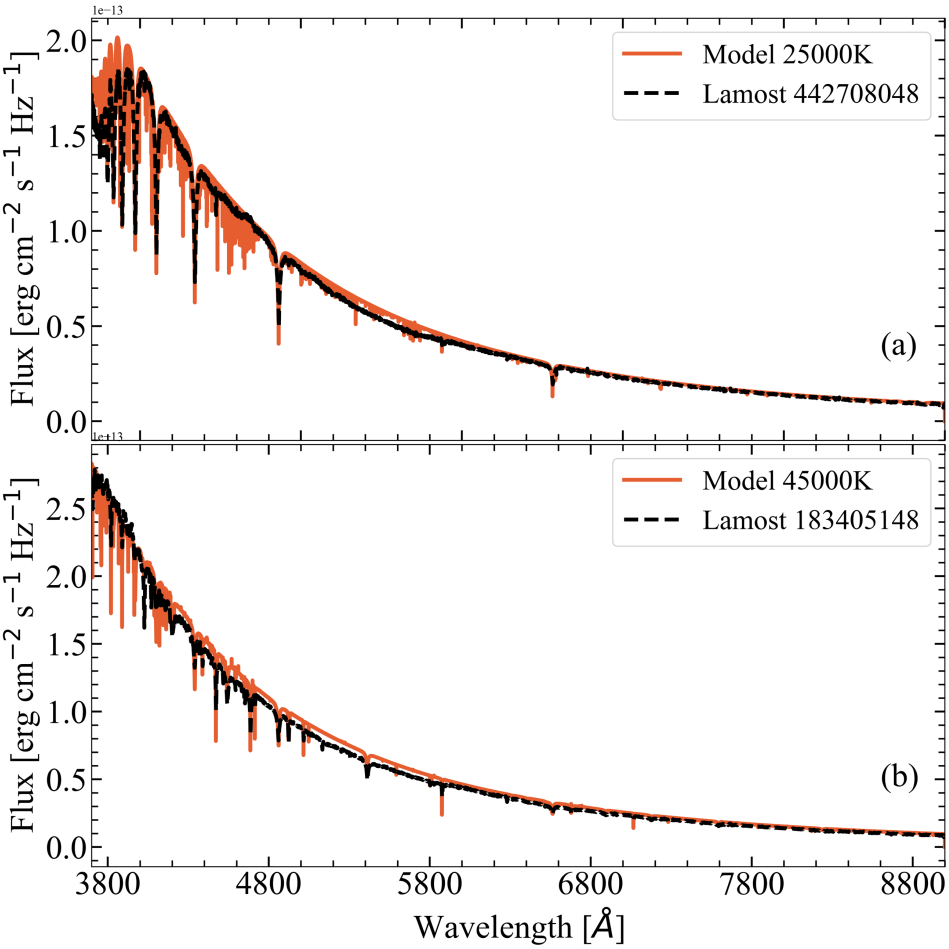

Figure 2.9: Top: comparison between the observed spectrum of Subdwarf Lamost 4427080 (dashed black) and the model spectrum with $T_{\rm eff}$ = 25 000 K and $\log g$ = 5.5 (solid orange). Bottom: comparison between the observed spectrum of Lamost 183405148 (dashed black) and the model spectrum with $T_{\rm eff}$ = 45 000 K and $\log g$ = 5.5 (solid orange). From Pacheco et al. (2021).

In Figure 2.10, HST/STIS Legacy Archive data on the bright Subdwarf HD 4539 were used to illustrate the models in the FUV. Parameters for this sdB are: $T_{\rm eff} = 26\,000 \pm 500$ K, $\log g = 5.2 \pm 0.1$, $\log (n_{He}/n_H)$ =-2.32±0.05, $E(B-V) = 0.04 \pm 0.01$ (Sale et al., 2008) and $d = 171.6 \pm 2.1$ pc (Gaia EDR3; Gaia Collaboration et al. (2021)). The models were scaled to match the continuum flux in the middle of each spectral range. He-poor branch and halo low-Z abundances were assumed here while $T_{\rm eff}$ and $\log g$ were linearly interpolated from model nodes to the literature values. Rotation, instrumental resolution, and exact chemical composition were neglected, which would explain the significant differences found in the lines and continua offsets. Using the Gaia distances and reddening values above, stellar radii compatible with typical values for Subdwarfs in eclipsing binaries (e.g., Rebassa-Mansergas et al. (2019) could be found. A line and/or continuum fitting of spectra can be performed with the XTGRID facility (Nemeth, 2019).

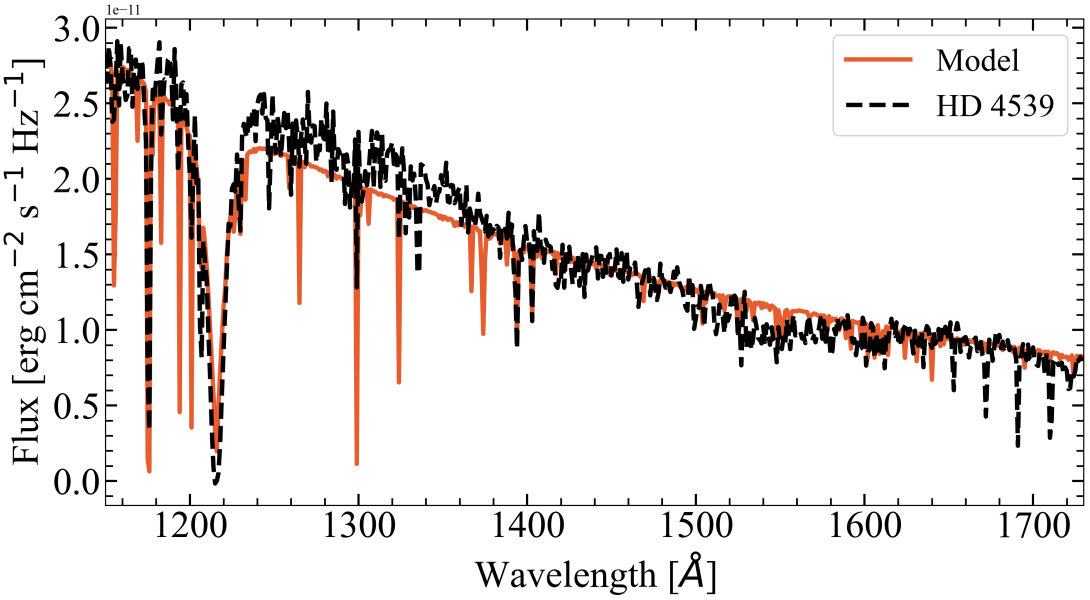

Figure 2.10: Comparison between the observed HST/STIS UV spectrum of HD 4539 (dashed black) and an interpolated model spectrum with $T_{\rm eff}$ 26,000 K and $\log g = 5.2$ (solid orange). From Pacheco et al. (2021).

2.3 Synthetic magnitudes

Synthetic magnitudes have been computed for several standard photometric bands to trend the grid's behavior in the color indices space and provide a comparison with photometry data. We used the filter response functions available on the Filter Profile

Service at the Spanish Virtual Observatory[6] (Rodrigo et al., 2012a; Rodrigo and Solano, 2020a) to convolve our synthetic integrated fluxes in the AB and Vega systems. The filters were interpolated in the spectra wavelength steps within the Shannon-Whittaker scheme. Photon-counting integrated fluxes were assumed (Bessell et al., 1998). Vega's zero points were previously evaluated from Calspec's standard spectrum (Bohlin et al., 2014).

Figure 2.11 illustrates our models in two color-color panels: panel (a) was chosen to trace the overall continuum inclination, and panel (b) traces the behavior of the Balmer jump. In panel (a), we show the F469N - F673N versus FQ757N - FQ750N colors of the HST/Wide Field Camera 3 (WFC3) photometric system. The dependence on effective temperature is evident. Those indices measure how lower-temperature synthetic models have a flatter continuum in the optical region. The point-size scale represents the surface gravity, where larger symbols relate to lower gravity ($\log g = 4.5$), and smaller symbols stand for higher gravity ($\log g = 6.5$), revealing a linear dependence in the color space. Finally, the circles represent solar abundance, and down-pointing triangles represent low halo metallicity, which has no clear separation on the diagram. In Figure 2.11 (b), the Strömgren photometric system indices were used. Zero-points were derived from Vega *uvby* magnitudes (Hauck and Mermilliod, 1998) and its calibrated spectrum from the STScI CALSPEC database (Bohlin et al., 2014). The color-color diagram of Figure 2.11 (b) was constructed with u (349.6nm) - v (410.3nm) and v - b (466.6nm) colors. It shows a temperature dependence of the Balmer break, which is more evident and also gravity-dependent for cooler atmospheres.

[6] `http://svo.cab.inta-csic.es/main/index.php`

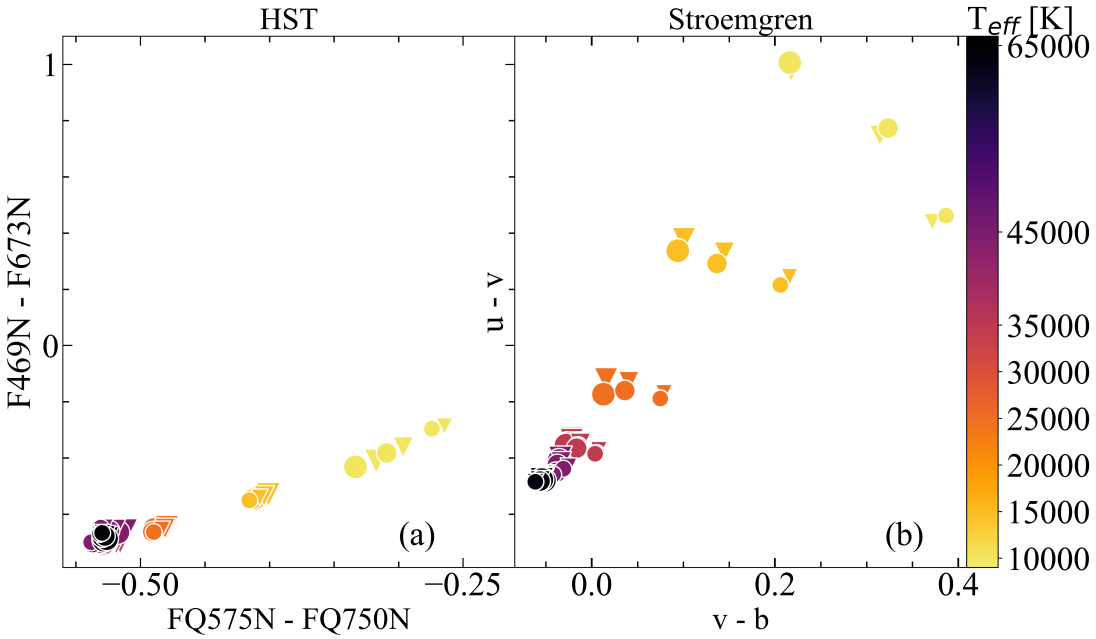

Figure 2.11: Color-color diagrams with the scale showing the effective temperatures, while the point-size scale shows the surface gravities (larger to lower gravity (4.5) and smaller to the higher gravity (6.5)); the circles indicate solar abundances and down-pointing triangles the low halo metallicity. (a) Color-color diagram for HST/WFC3 indices F469N - F673N and FQ757N - FQ750N. (b) Color-color diagram for classical Strömgren u (349.6nm) - v (410.3nm) and v - b (466.6nm) indices, aiming to probe the Balmer discontinuity. Bases on Pacheco et al. (2021).

The study of the 5874 hot Subdwarf stars with Gaia Data Release 2 by Geier (2020) is the most complete sample of Subdwarfs. From this catalog, we selected data from 3450 targets (1482 with determined effective temperature and colors) observed by the Sloan Digital Sky Survey (SDSS) photometric system to compare with the grid synthetic magnitudes. The color-color diagram in Figure 2.12 is composed of g - r and u - g colors without any color cutoff. Observational data with a determined effective temperature are shown as dots scaled by hue, while those with an undetermined effective temperature are gray crosses. Our 96 synthetic colors are displayed in the same hue, style, and size scales as in Figure 2.11, matching the sdO, sdB, and sdOB previously classified by Geier (2020). The upper data sequence represents the Subdwarf composite binaries with main-sequence star companions.

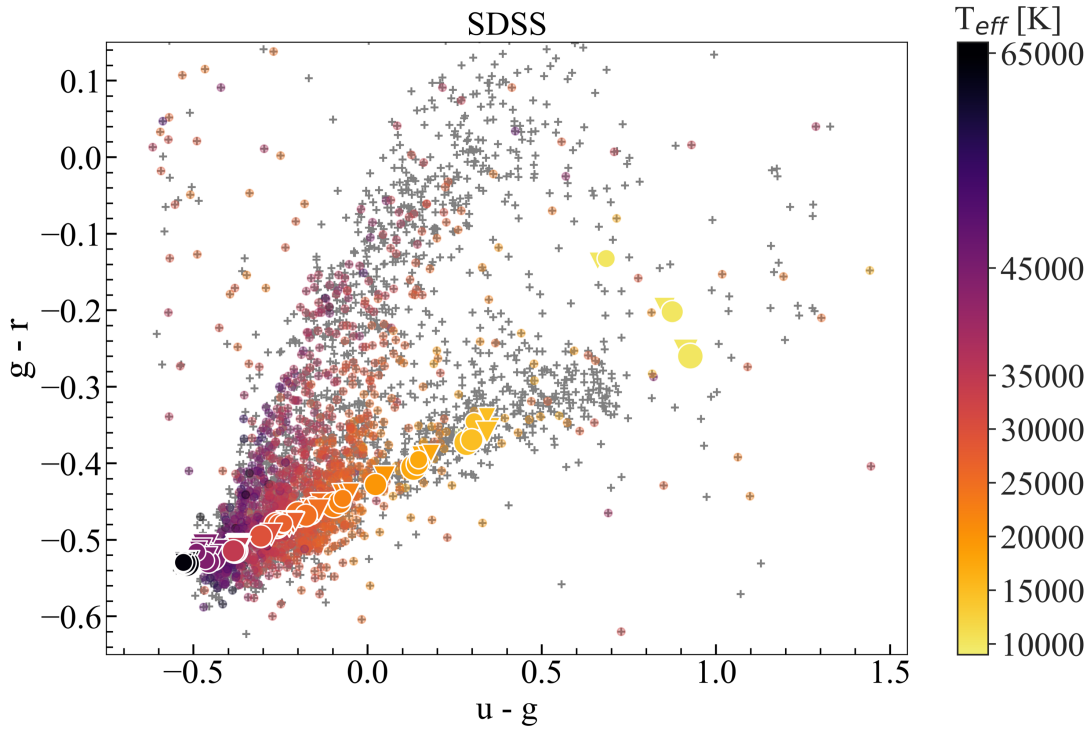

Figure 2.12: Color-color diagram (g - r vs. u - g) composed of observational data on Subdwarfs from SDSS (see text) with a hue scale representing determined effective temperatures, while the gray crosses showed an undetermined effective temperature. The synthetic colors from our grid are plotted with the same hue, style, and size scales as in Figure 2.11. Based on Pacheco et al. (2021) and Pacheco et al. (2023).

2.4 Summary

We presented a grid of NLTE, fully blanketed theoretical spectra, and synthetic photometry for hot and moderately cool Subdwarf stars. The atmosphere models were computed considering line blanketing of H, He, C, N, O, Ne, Mg, Al, Si, S, and Fe. The effective temperatures are $T_{\rm eff}$ = 10,000, 15,000, 17,500, 20,000, 22,500, 25,000, 27,500, 30,000, 35,000, 45,000, and 65,000 K, while the surface gravities are $\log g$ [cgs] = 4.5, 5,0, 5.5, and 6.5. The two representative chemical abundances are solar and Galactic halo, each with extreme scenarios for He-rich and He-poor stellar atmospheres.

The main differences between LTE and NLTE atmosphere structures are shown for these objects. They have significant differences in the outermost atmospheres, leading to distinct line-core profile formation.

The complete high-resolution spectral synthesis is performed from the UV to near-IR (1000 to 10,000 Å) in 0.01 Å steps. We provided an illustrative analysis for the UV and

the optical regions by comparing our models with observed spectra from LAMOST and HST/STIS Legacy Archive data.

The behavior of the color indices was analyzed using the HST/WFC3 and the Strömgren photometric systems. A clear separation in effective temperature can be seen, as well as gravity for lower-temperature models, as provided by the Balmer discontinuity. We also matched our synthetic magnitudes against SDSS Subdwarf data with a fair agreement.

These results pave the way for both spectroscopic and photometric analyses of fundamental parameters in isolated or binary objects, which, in turn, may provide a more detailed insight into the atmosphere models themselves. The entire spectral grid and synthetic indices are available in the IAG-USP [7], SVO [8], and Vizier [9] databases.

Classical stellar population synthesis analysis can use the homogeneous spectral grid to understand better the blue and ultraviolet properties of old stellar populations.

[7] Spectral Models of Stars and Stellar Populations, `http://specmodels.iag.usp.br/`.

[8] Spanish Virtual Observatory, `http://svo2.cab.inta-csic.es/theory//newov2/`.

[9] Vizier, `https://vizier.u-strasbg.fr/viz-bin/VizieR`

Chapter 3

Modeling spectra of stellar populations

This Chapter provides details of stellar population synthesis and our novel methodology to compute integrated spectra, based on the publication by Pacheco et al. (2024). We will explore the key characteristics of the studied globular clusters, synthetic stellar flux libraries, and the results regarding the comparison between modeled and observed integrated spectra (Pacheco et al., 2024, Pacheco et al. a,b, *in prep*).

We modeled the integrated spectra of simple stellar populations based on the color-magnitude diagram methodology described in Martins et al. (2019) (see as well Section 1.1.2). In short, the color-magnitude diagram of a Galactic globular cluster represents the locus of the stars in an HR diagram without the need for isochrones and assumptions of the initial mass function. Martins et al. (2019) mapped the observational data of the globular clusters in two steps: 1) the color-magnitude diagram is converted to the Kiel plane via color-temperature and gravity transformations from literature and 2) each star in the Kiel diagram is associated with a stellar spectrum in a library, minimizing the distance between the model and observation in the $T_{\rm eff}$–$\log g$ plane.

Therefore, the method requires two ingredients: 1) a good-quality color-magnitude diagram of an old globular cluster and 2) a library of stellar spectra covering all the relevant parameter space (in evolutionary phases and/or temperature and gravities).

3.1 Stellar globular clusters

We use Galactic old globular clusters as proxies for studying integrated, "simple" stellar populations. Despite these sources being composed of multiple stellar populations (see e.g., Bastian and Lardo, 2018), this is a step towards accurately reproducing the integrated light

under more realistic assumptions. Analyzing these Galactic globular clusters allows us to validate our methods regarding integrated stellar populations by comparing them with resolved observations. For this work, we selected the Galactic globular cluster observed by the Hubble Space Telescope featuring extended Horizontal Branches.

3.1.1 NGC 2808

NGC 2808 is located in the constellation of Carina in the South Hemisphere (α, δ = 138.0071°, −64.8645°; Gaia Collaboration et al. 2018). Figure 3.1 shows a composite image of multiple exposures, taken by the HST Advanced Camera for Surveys and the Wide Field Camera (ACS/WFC) instrument, using two filters (Piotto et al., 2002). The color results were assigned by combining monochromatic images: Blue (F475W), Green (F475W + F814W), and Red (F814W).

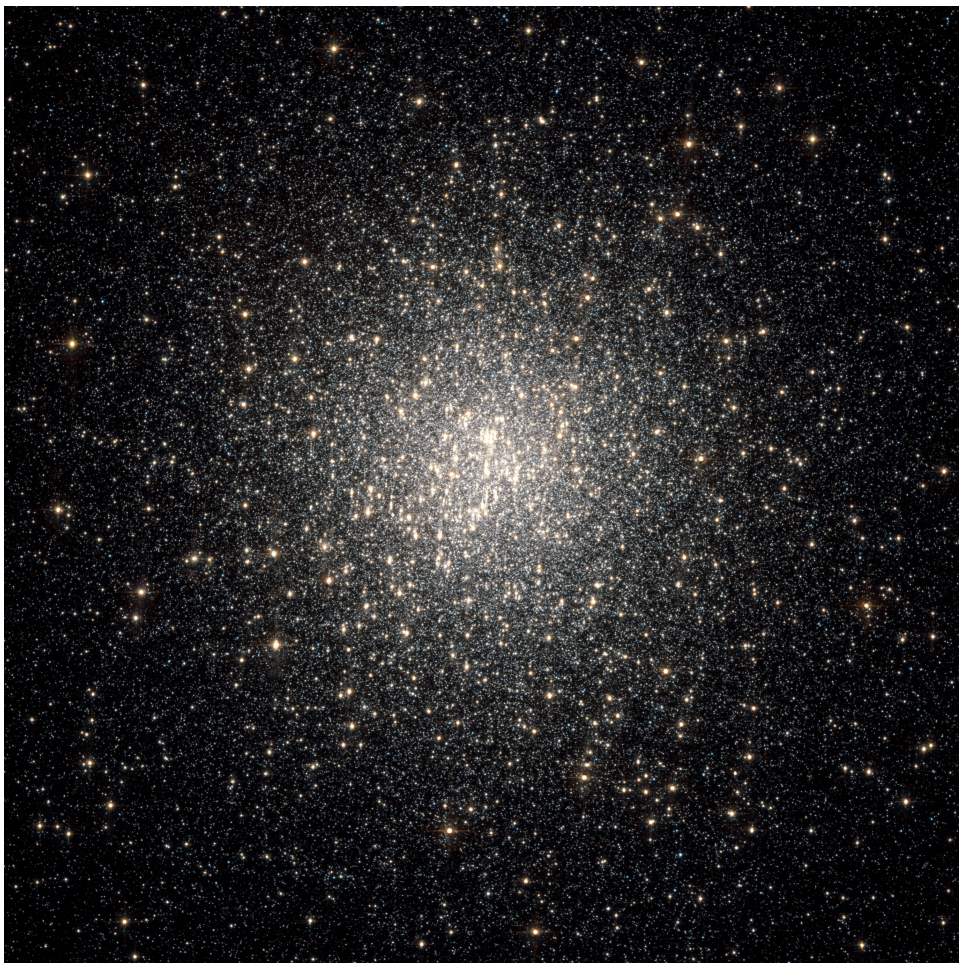

Figure 3.1: HST image of the NGC 2808. Science credit: Piotto et al. (2002). Image credit: ESA/Hubble & NASA; A. Sarajedini and G. Piotto.

NGC 2808 is one of Milky Way Galaxy's oldest well-known globular clusters, 11.5 ± 0.4 Gyr old (Limberg et al., 2022). Its stars originated in a timeframe of 200 million years. Also, as one of the most massive clusters, it exhibits over 1 million stars and has a mass of $8.5 \cdot 10^5$ $M_\odot$(McLaughlin and van der Marel, 2005).

There is evidence of up to five stellar populations and different abundances in NGC 2808. Carretta (2015) found a metallicity of [Fe/H] $= -1.129 \pm 0.005 \pm 0.034$ (± statistical ± systematic error). However, Colucci et al. (2017) presented differences between the mean abundances from Fe I and Fe II lines, with final abundances of [Fe I/H] $= -1.04 \pm 0.04$ and [Fe II/H] $= -0.85 \pm 0.04$. A recent study by Lardo et al. (2022) confirms a metallicity spread for several globular clusters, and Lardo et al. (2023) shows that NGC 2808 has a variation equal to 0.25 ± 0.06 dex. They also presented the mean abundance of [Fe/H]= -1.03 ± 0.07 for the first population. Nevertheless, using high-resolution spectra from APOGEE DR17, Limberg et al. (2022) show a mean metallicity [Fe/H] $= -1.09 \pm 0.01$ with dispersion of 0.05 dex, and this will be the reference value hereafter.

3.1.2 M2

M2 is located in the constellation of Aquarius, in the South Hemisphere (α, δ = 323.3497°, −0.8177°; Gaia Collaboration et al. (2018)). Limberg et al. (2022) shows a reddening variation across M2 field of view. A composite image is shown in Figure 3.2, taken by HST ACS/WFC instrument using three filters Piotto et al. (2002). The colored image combines UV (F275W) and optical (F336W and F438W) filters.

NGC 7089 (M2) is also one of the largest and oldest globular clusters in the Milk Way Galaxy, 11.5 ± 0.3 Gyr old (Limberg et al., 2022). Milone et al. (2014) found evidence of up to seven stellar populations to explain M2 chemical evolution.

The iron abundance distribution for M2 presented by Yong et al. (2014) displays a prominent peak around [Fe/H] $= -1.7$, accompanied by smaller peaks at approximately −1.5 and −1.0, where the latter group was not firmly established. However, Lardo et al. (2016) showed that M2 iron abundance is bimodal, with the first component at [Fe/H] $= -1.5$ and a small fraction of stars at [Fe/H] $= -1.1$. Limberg et al. (2022) show a mean metallicity [Fe/H] $= -1.46 \pm 0.02$ with dispersion of 0.05 dex, which will be the reference value hereafter.

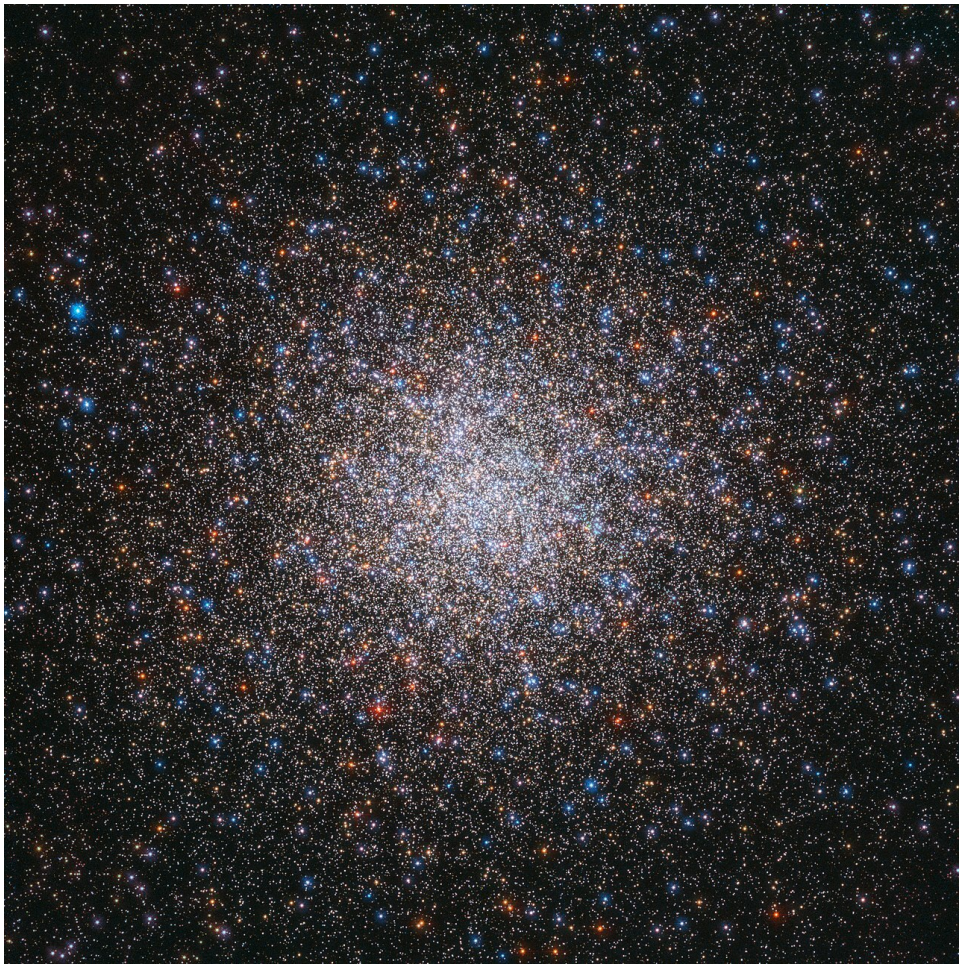

Figure 3.2: HST image of the NGC 7089 (M2). Science credit: Piotto et al. (2002). Image credit: ESA/Hubble & NASA; A. Sarajedini and G. Piotto.

3.2 Stellar flux libraries

We used three synthetic stellar spectral libraries in this study, namely Castelli and Kurucz (2003); Coelho (2014); Pacheco et al. (2021) and Pacheco et al. (2023).

Spectra from Pacheco et al. (2021, 2023) were employed to represent the Extreme Horizontal Branch for both globular clusters, NGC 2808 and M2. This library was described in detail in Chapter 2. This is a grid of detailed stellar atmosphere models and spectra for extremely blue Horizontal Branch stars. This grid of models includes NLTE atmosphere models, high−resolution NLTE spectra, and synthetic photometry, covering a temperature range of $10\,000 \leq T_{\rm eff}$ [K] $\leq 65\,000$, surface gravities of $4.5 \leq \log g$ [cgs] ≤ 6.5, and two extreme scenarios of helium abundances (helium-rich and helium-poor). We also considered two sets with different metallicities: a solar metallicity case ([Fe/H]$= 0$) and one with halo stellar metallicity ([Fe/H]$= -1.5$, with an enhancement of $[\alpha/{\rm Fe}] = +0.4$). In

the following analysis, we used spectral models with chemical parameters representing the typical Galactic halo with the helium-rich sequence for all the studied globular clusters.

We chose models from Coelho (2014) grid to represent the other evolutionary phases of NGC 2808. Coelho (2014) computed a theoretical stellar library that covers a temperature range of $3\,000 \leq T_{\rm eff}[{\rm K}] \leq 25\,000$ and includes solar and α-enhanced compositions. This library provides a wide range of atmospheric parameters, such as a surface gravity range of $-0.5 \leq \log g[{\rm cgs}] \leq 5.5$ and 12 different chemical mixtures covering $0.0017 \leq {\rm Z} \leq 0.049$. These spectra models have a resolving power (R) of 20 000 and cover the wavelength range from 2 500 Å to 9 000 Å with a constant sampling of 0.2 Å. From this set of parameters, we used metallicity of [Fe/H] $= -1.0$ and enhancement of $[\alpha/{\rm Fe}] = +0.4$.

The model grid from Castelli and Kurucz (2003) was chosen to represent the evolutionary phases of M2. Castelli and Kurucz (2003) computed statistical surface fluxes that cover a temperature range of $3\,500 \leq T_{\rm eff}[{\rm K}] \leq 50\,000$ and includes solar and α-enhanced compositions. This library provides a wide range of atmospheric parameters. These low-resolution spectral energy distributions mimic a resolving power (R) of approximately 250 and cover the wavelength range from 1 Å to 100 200 Å with a variable spatial sampling across the spectra. From this set of parameters, we used wavelengths from 1 000 Å to 10 000 Å, the metallicity of [Fe/H] $= -1.5$, and enhancement of $[\alpha/{\rm Fe}] = +0.4$. In the wavelength range of interest, the sampling comprises of points every 10 Å at 1 000 Å and 20 Å at 10 000 Å.

We selected only the metallicity closest to the target globular cluster from each grid. Table 3.1 presents the number of models used in this work, with their respective range of wavelength λ, atmosphere parameters $T_{\rm eff}$ and $\log g$, chemical abundances [Fe/H] and $[\alpha/{\rm Fe}]$, resolving power R [1], and wavelength sampling.

[1] at $\lambda = 5\,000$ Å.

Table 3.1 - Synthetic parameters used in the analysis.

Library	Pacheco et al. (2021, 2023)	Coelho (2014)	Castelli and Kurucz (2003)
# of models	36	328	476
λ [Å]	1 000 to 10 000	2 500 to 9 000	1 000 to 10 000
$T_{\rm eff}$ [K]	10 000 to 65 000	3 000 to 26 000	3 500 to 50 000
$\log g$ [cgs]	4.5 to 6.5	−0.5 to 5.5	0.0 to 5.0
[Fe/H]	−1.5 *	−1.0	−1.5
[α/Fe]	+0.4	+0.4	+0.4
$R_{mean} = \frac{\lambda}{\Delta\lambda}$	250 000	20 000	250
Sampling [Å]	0.01	0.2	10 to 20

* He-enriched: see Table 2.2.

3.2.1 Synthetic photometry

We used the procedure described in Section 2.3 to compute synthetic magnitudes. We adopted the VEGA system and incorporated the respective zero points, which serve as a reference flux value for a particular photometric band. Zero point (ZP) is defined as the flux of an object that produces a magnitude of precisely zero when measured in that specific filter. We used the Spanish Virtual Observatory (SVO), which provides standardized and comprehensive access to astronomical data, for this Section. It includes photometric filters, transmission curves, and calibration, facilitating multi-wavelength studies (Rodrigo et al., 2012b; Rodrigo and Solano, 2020b). The details about the identification associated with each filter, instrument information, effective, minimum, and maximum wavelengths, and their flux zero points are presented in the Table 3.2.

Table 3.2 - Information about HST spectral filters.

Filter	Instrument	λ_{eff} [Å]	λ_{min} [Å]	λ_{max} [Å]	ZP_λ [erg/cm^2/s/Å]
F275W	WFC3/UVIS	2 720.87	2 286.17	3 120.27	3.74×10^{-9}
F336W	WFC3/UVIS	3 359.43	3 014.02	3 706.78	3.26×10^{-9}
F438W	WFC3/UVIS	4 323.73	3 894.93	4 710.01	6.73×10^{-9}
F606W	ACS/WFC	5 810.77	4 626.09	7 179.31	2.87×10^{-9}
F815W	ACS/WFC	7 972.92	6 867.80	9 626.12	1.14×10^{-9}

A convolution between the flux of the synthetic spectrum (f) and each filter transmission (t) was performed to compute the synthetic magnitudes. The resulting function ($f \cdot t$) addresses the alteration introduced by one function shape to the other, selectively

simulating the passage of light at specific wavelengths through the filters while blocking others. In addition, we computed the area under the curve of each synthetic spectrum, which was subsequently employed in the spectral normalization process.

We calculated the synthetic photometry of the three synthetic spectral grids for five different HST filters: F275W, F336W, F438W, F606W, and F814W. The transmission curves for each filter through the wavelengths are shown in Figure 3.3.

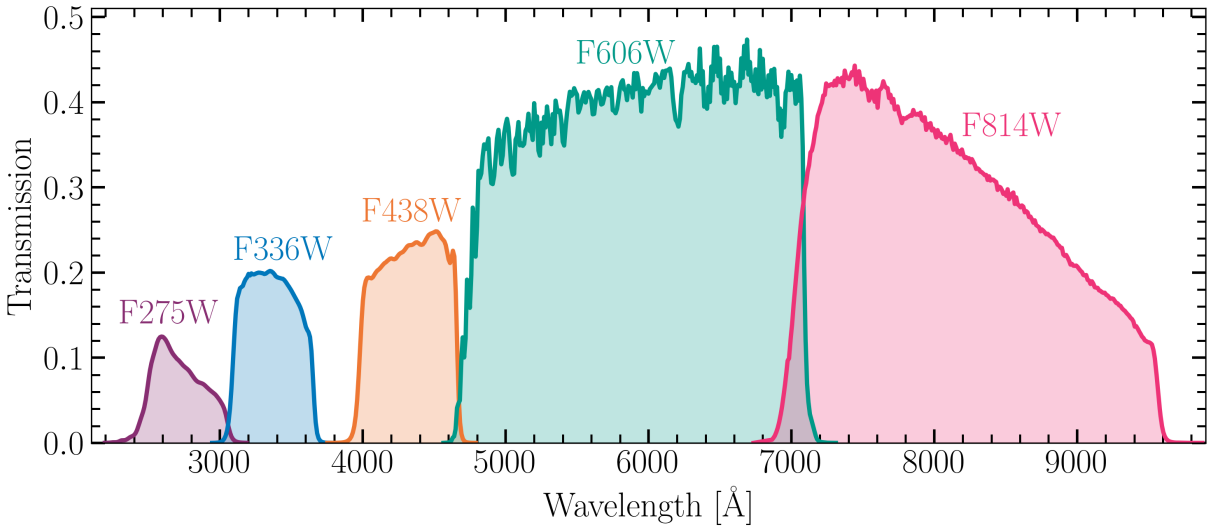

Figure 3.3: HST photometric transmission curves for the bands: F275W, F336W, F438W, F606W, and F814W.

3.3 Photometric data of the globular clusters

We used multi-photometric observations of Galactic globular clusters of the Hubble Space Telescope (Piotto et al., 2015; Nardiello et al., 2018). The data covers a wide range of wavelengths, from ultraviolet (UV) to near-infrared (IR). It has F275W, F336W, and F438W bands observed by the new Wide Field Camera 3 (WFC3) in the channel for ultraviolet and visible light (UVIS). It also includes F606W and F814W bands observed by the Advanced Camera for Surveys (ACS) in the Wide Field Channel (WFC). See Figure 3.3 and Table 3.2 for instrumental details about the filters.

We selected stars that are likely cluster members, with a membership probability greater than 90% (Nardiello et al., 2018). We applied a threshold for the photometric errors, excluding observations with uncertainty exceeding the typical magnitude error limit of 0.07 mag for F275W, 0.05 mag for F336W, and 0.03 mag for F438W, F606W, and F814W

bands.

We subtract the interstellar effects from the observed photometry by calculating the reddening values for each filter. We chose the Fitzpatrick and Massa (2007) extinction law defined from 910 to 6 000 Å. Therefore, it is optimized from the UV to the visible wavelengths. To compute the reddening, we used the package `extinction` that has implemented empirical interstellar dust extinction laws in Python (Barbary, 2016). The photometric extinction was based on the color excess E(B-V) of 0.22 and 0.06 for NGC 2808 and M2, respectively (Usher et al., 2017).

3.4 Novel methodology

We synthetise integrated spectra based on color-magnitude diagrams (Santos et al., 1990, 1995; Schiavon et al., 2004; Martins et al., 2019). This methodology avoids the caveats of isochrones that cannot explain evolved stellar populations, such as Extreme Horizontal Branch, and we do not use the initial mass function assumptions.

We propose here a two-step adaptation to the method presented in the literature, as described below.

3.4.1 Tagging the evolutionary phase

We categorized the photometric data into distinct groups for each globular cluster to represent stellar evolutionary stages. We chose six regions to represent the different evolutionary stages:

- Main Sequence (MS): the stars cooler and fainter than the visual turn-off;
- Giant Branch and Asymptotic Giant Branch (GB): the stars cooler than the visual turn-off and brighter than the MS;
- Red Horizontal Branch (RHB): the Horizontal Branch stars between the Horizontal Branch gap and the GB;
- Blue Straggler (BS): the plume of stars brighter than the turn-off and fainter than the HB;
- Blue Horizontal Branch (BHB): the intermediate Horizontal Branch, and;

- Extreme Horizontal Branch (EHB): the stars hotter than the knee of the Horizontal Branch in the ultraviolet color (F275W–F336W).

These phases are classified based on their observational features in different filters. The selection process to create those sub-samples was done by using `TOPCAT` (Tool for OPerations on Catalogues And Tables, Taylor 2005). Tables 3.3 and 3.4 present a comprehensive range of photometric cutoffs in various magnitudes and colors to select the sub-samples for NGC 2808 and M2, respectively.

Table 3.3 - Cutoffs (in *mag*) of the NGC 2808's evolutionary phase sub-samples by using the `TOPCAT`.

	MS	GB	RHB	BS	BHB	EHB
F275W	≥ 18.0	–	≤ 17.8	≥ 18.6	≤ 17.0	–
F336W	≥ 17.5	≤ 18.8	≤ 15.9	≥ 18.6	≤ 17.3	–
F606W	–	–	15.0 to 15.8	15.8 to 18.8	≤ 18.0	–
F814W	≥ 17.15	≤ 17.5	–	–	–	–
$C_{F(275-336)W}$	0.0 to 2.0	≥ 0.75	≥ 0.5	-0.5 to 0.9	-0.4 to 0.5	≤ -0.4
$C_{F(336-438)W}$	-1.0 to 1.0	≥ -0.2	–	-0.7 to 0.0	–	–
$C_{F(438-606)W}$	0.0 to 2.0	≥ -0.7	≤ 1.0	0.0 to 0.75	≤ 0.4	–
$C_{F(606-814)W}$	0.0 to 1.3	≥ 0.35	0.3 to 0.7	-0.05 to 0.35	≤ 0.3	≤ 0.0
$C_{F(336-814)W}$	–	–	–	–	–	≤ 0.35
Notes	no GB	–	–	–	–	

Table 3.4 - Cutoffs (in *mag*) of the M2's evolutionary phase sub-samples by using the `TOPCAT`.

	MS	GB	RHB	BS	BHB	EHB
F275W	≥ 18.4	–	≤ 18.0	$\geq 18.69.0$	≤ 17.2	–
F336W	≥ 17.9	≤ 18.95	≤ 16.5	≥ 18.9	≤ 17.5	–
F606W	–	–	15.0 to 15.8	16.2 to 19.2	≤ 18.2	–
F814W	≥ 17.45	≤ 17.65	–	–	–	–
$C_{F(275-336)W}$	0.15 to 2.15	≥ 0.8	≥ 0.5	-0.5 to 0.9	-0.4 to 0.5	$\leq$ -0.4
$C_{F(336-438)W}$	-0.85 to 1.85	$\geq$ -0.25	–	-0.5 to 0.2	–	–
$C_{F(438-606)W}$	0.15 to 2.15	$\geq$ -0.75	≤ 1.05	0.0 to 0.75	≤ 1.05	–
$C_{F(606-814)W}$	0.15 to 1.45	≥ 0.4	0.4 to 0.75	-0.05 to 0.4	≤ 0.4	≤ 0.0
$C_{F(336-814)W}$	–	–	–	–	–	≤ 0.35
Notes	no GB	–	–	–	–	

The resulting color-magnitude diagrams with the sample of stars tagged by their evolutionary phases of the NGC 2808 are presented in Figure 3.4.

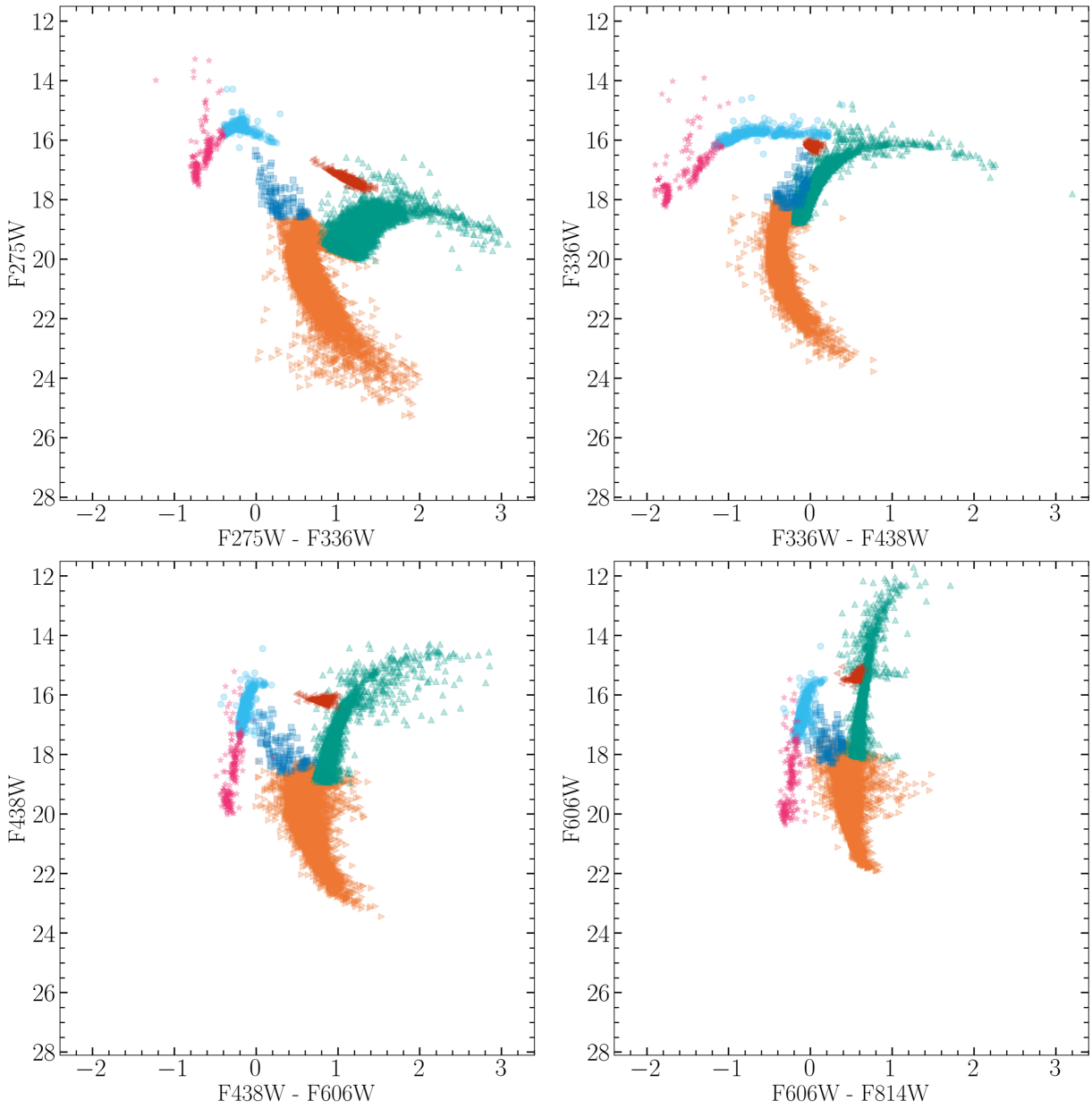

Figure 3.4: Color-magnitude diagram of the NGC 2808 colored by subsets: Main Sequence in orange right triangles, Giant Branches in teal up triangles, Red Horizontal Branch in red left triangles, Blue Straggleres in blue squares, Blue Horizontal Branch in cyan points and Extreme Horizontal Branch in magenta stars.

The resulting color-magnitude diagrams with the sample of stars tagged by their evolutionary phases of the M2 are presented in Figure 3.5.

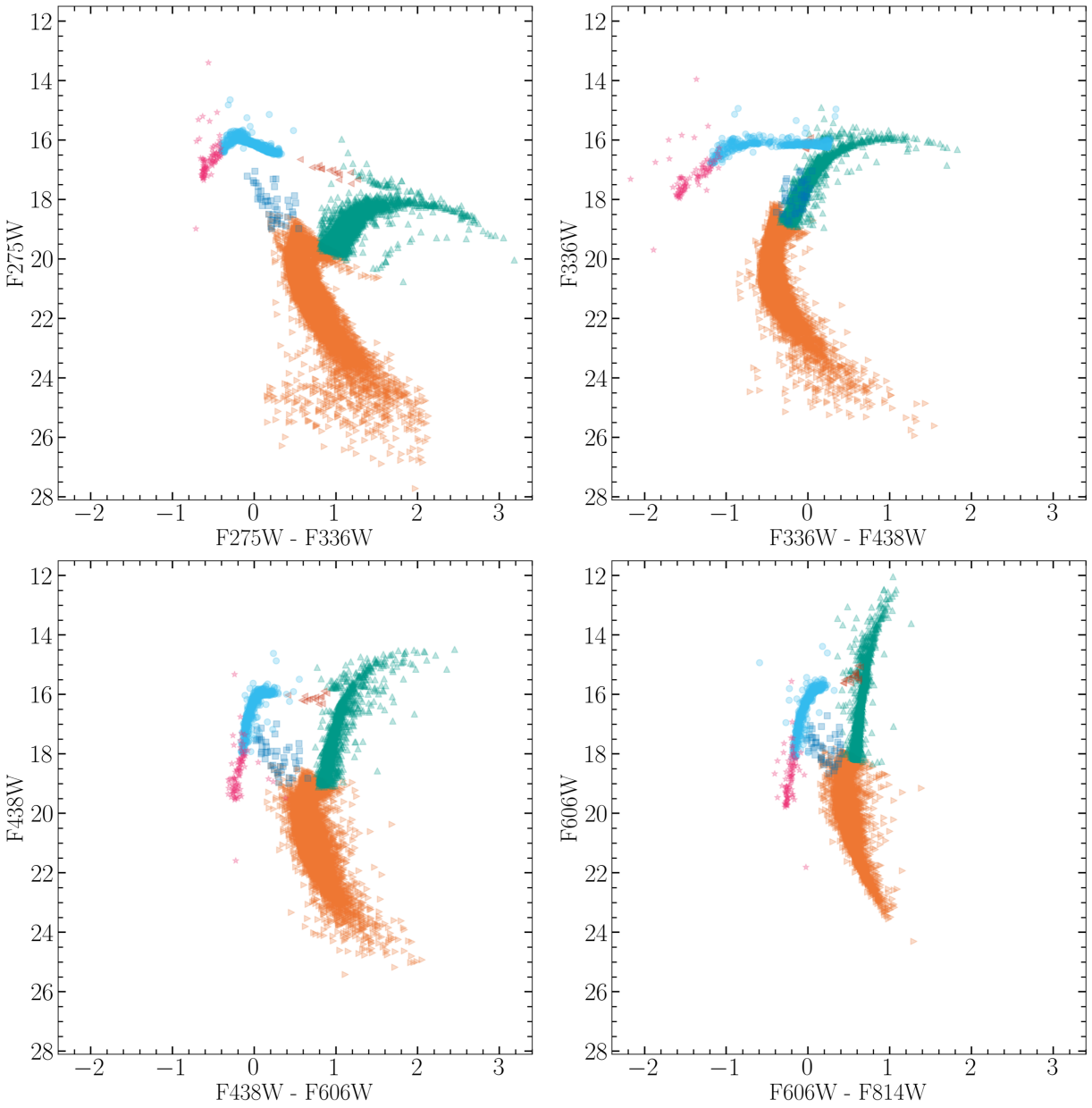

Figure 3.5: Color-magnitude diagram of the M2 colored by subsets: Main Sequence in orange right triangles, Giant Branches in teal up triangles, Red Horizontal Branch in red left triangles, Blue Straggleres in blue squares, Blue Horizontal Branch in cyan points and Extreme Horizontal Branch in magenta stars.

3.4.2 Matching observed to synthetic stars

Usually, the methodologies based on color-magnitude diagrams use power law transformations from the observational plane (color and magnitude) to the theoretical plane ($T_{\rm eff}$ and $\log g$). Martins et al. (2019) used the high-order fitting functions of the Worthey and Lee (2011) calibration for transforming the data into the Kiel diagram. The primary source of error in color-temperature calibration is finding a suitable polynomial to trace

the intricate variations in colors accurately. Also, the fitting process involves a substantial number of stars for each fit. Notably, uncertainties for cool dwarf stars are more significant than uncertainty in giants due to the small number of dwarf calibrations to estimate it (Worthey and Lee, 2011). A significant limitation in this calibration is its applicability only to Main Sequence and Giant Branch stars, which only covers some of the required parameters for our analysis

We propose to circumvent this translation by directly matching each observed star to a synthetic spectrum in a multi-dimensional color plane and avoiding uncertainties associated with the isochrones. In our proposed method, both synthetic and observational photometry were combined in pairs of filters to build a ten-dimensional space: F275W − F336W, F275W − F438W, F275W − F606W, F275W − F814W, F336W − F438W, F336W − F606W, F336W − F814W, F438W − F606W, F438W − F814W, and F606W − F814W. This accounts for the variations in all ten attributes to determine the overall separation between the two points in this higher-dimensional space. The new method facilitates the model selection with the closest representation of physical parameters for each star of a globular cluster.

A model representing each star is selected by minimizing its color distance. We computed the geometrical distance between synthetic and observed colors in this ten-dimensional space, as shown in equation 3.1:

$$d = \sqrt{{d_1}^2 + {d_2}^2 + {d_3}^2 + {d_4}^2 + {d_5}^2 + {d_6}^2 + {d_7}^2 + {d_8}^2 + {d_9}^2 + {d_{10}}^2} \tag{3.1}$$

where d_1 to d_{10} indicate the 10 colors. The closest model was located with the aid of the K-nearest neighbors algorithm implemented in `scikit-learn.neighbors` python package (Pedregosa et al., 2011).

Figure 3.6 shows five color-color diagrams representing all the ten colors used in the analysis of the NGC 2808. The distribution of our sample of observed stars by evolutionary phases is hued in the same pattern as in Figure 3.4. The synthetic colors from Coelho (2014) are shown in grey crosses, and from Pacheco et al. (2021, 2023) are shown in black diamonds, representing an excellent coverage of the space parameters. The diamond symbols show the whole coverage of the libraries, not only the models selected to match the observed stars. The bottom-left panel shows the histograms of distances (in magnitudes) between the star and its associated model. The histogram is normalized by the number of

stars in each evolutionary phase, where the vertical axis represents the percentage of stars in that specific evolutive stage. We find that, for all evolutionary phases, the distributions of distances show a narrow profile around 0.2 *mag*, as shown in the last panel of Figure 3.6.

Figure 3.7 shows the same figure for M2. We used the Castelli and Kurucz (2003) library instead of the Coelho (2014), as the latter do not reach the low metallicity of this cluster. The peaks of the distance distributions for this case are around 0.1mag, which is smaller than that of the NGC 2808 for all the evolutionary phases. This is a consequence of Castelli and Kurucz (2003)'s library having a higher density and colors in the $T_{\rm eff}$–$\log g$ parameter space, thus achieving bluer colors.

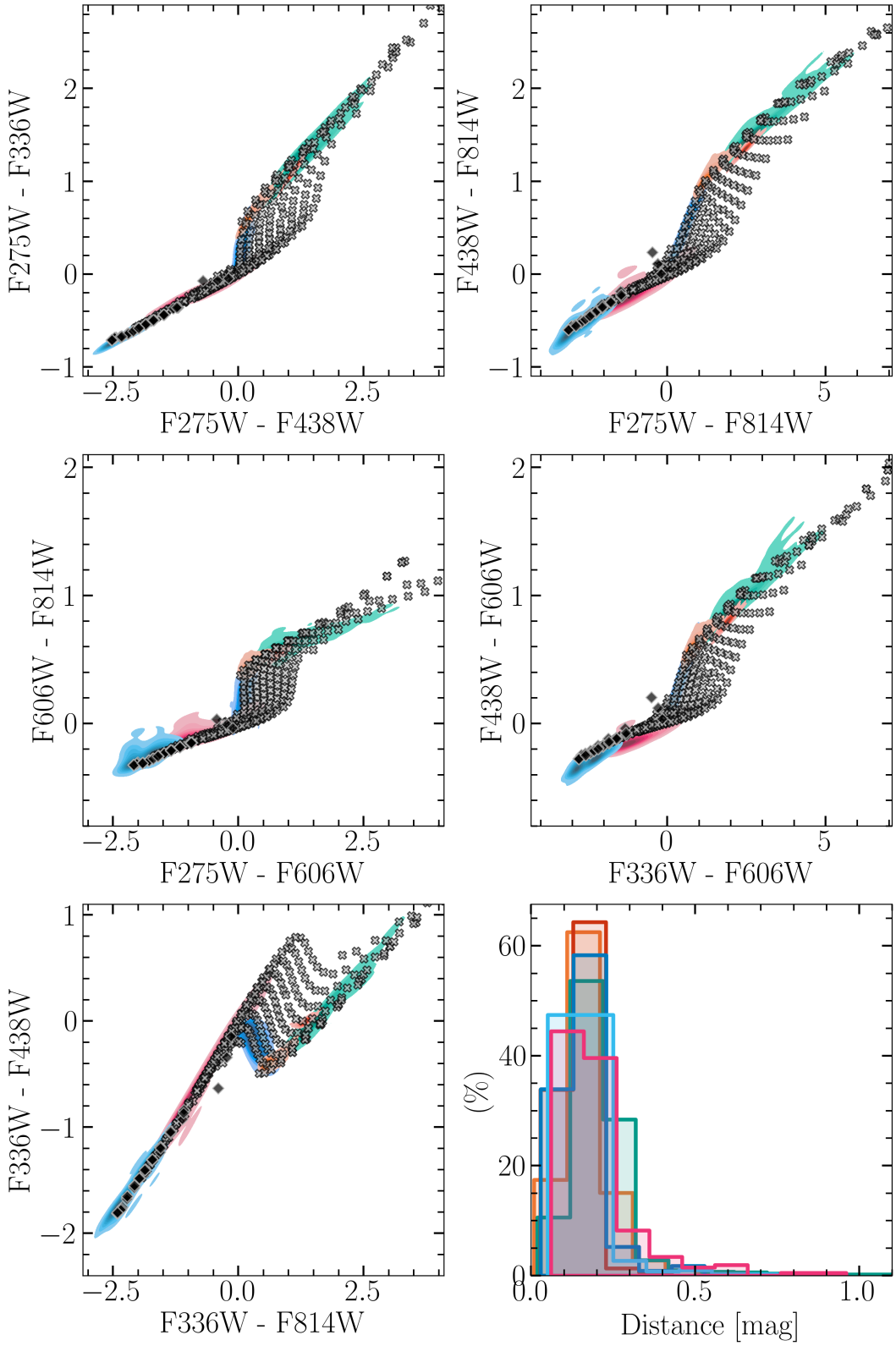

Figure 3.6: Color-color diagrams of the NGC 2808 hued by subsets: Main Sequence in orange, Giant Branches in teal, Red Horizontal Branch in red, Blue Straggleres in blue, Blue Horizontal Branch in cyan and Extreme Horizontal Branch in magenta. *Bottom left:* histogram of the distributions of distances between observed and synthetic colors normalized by the number of stars in each evolutionary phase. It follows the same color scheme as the other panels.

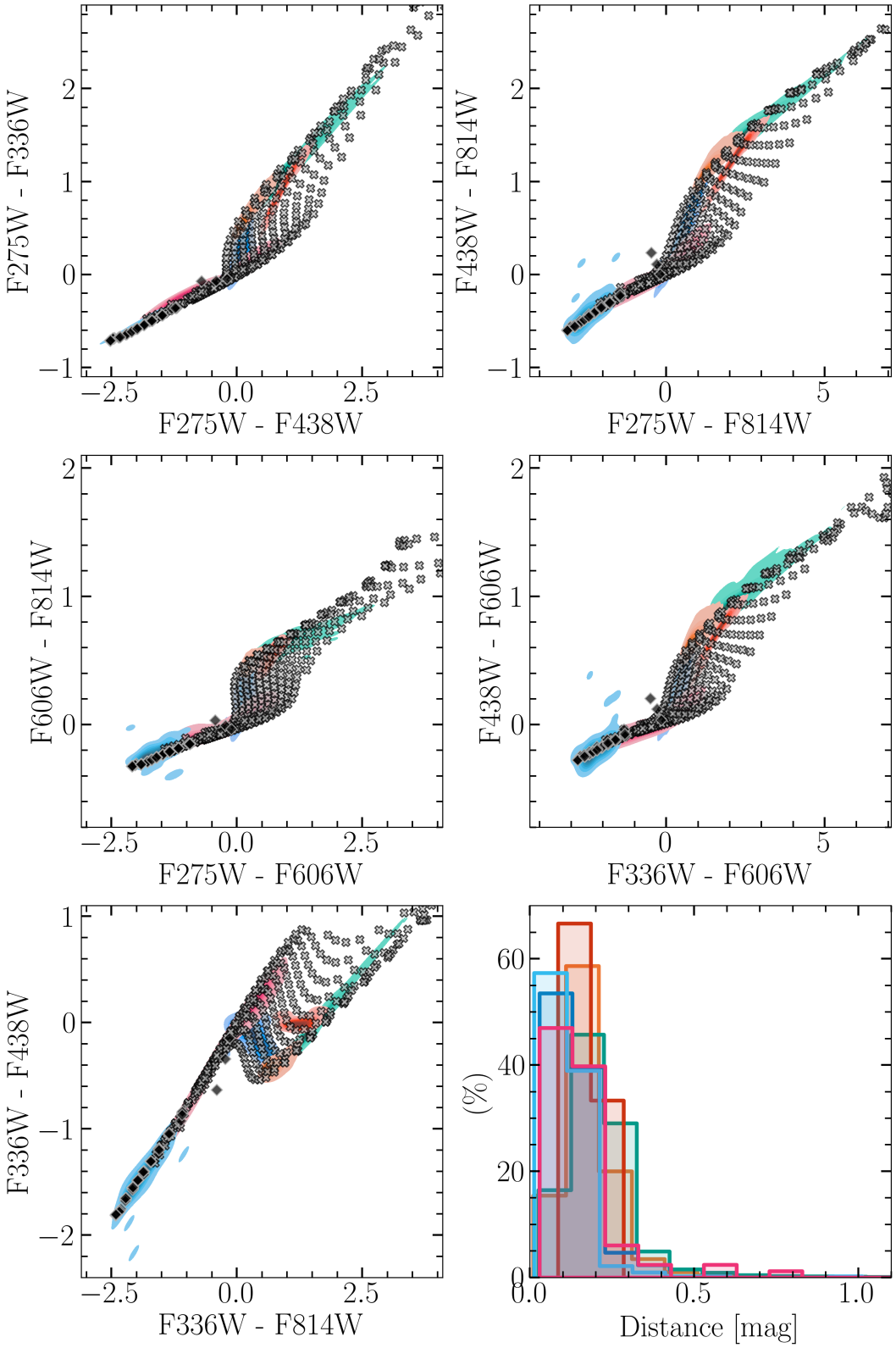

Figure 3.7: Color-color diagrams and histogram of the distributions of distances of the M2 hued by subsets in the same scheme as in Figure 3.6.

3.5 Synthetic integrated spectra

Once each star in the Color-Magnitude Diagram is matched to a stellar spectrum, the modeled integrated flux $F_{SSP}(\lambda)$ of the globular cluster is given by the expression 3.2:

$$F_{SSP}(\lambda) = \sum_{i=1}^{N} f_{star}(\lambda) \cdot 10^{-0.4(M_i - M_s)}, \tag{3.2}$$

where $f_{star}(\lambda)$ is the synthetic spectrum that represents the i^{th} star, and N is the total number of stars in the globular cluster (Schiavon et al., 2004; Martins et al., 2019). The composite spectrum includes the weight given to each selected synthetic stellar spectrum by the transmission filter in a chosen photometric band (F438W). The weighting factor is obtained based on the differences between the model magnitude, M_i, and its corresponding observed stellar magnitude, M_s. We integrated the spectra for six sub-samples, one per evolutionary phase as described in Section 3.4.

The integrated light spectra of the Main Sequence, Giant Branches, red Horizontal Branch, Blue Straggler, Blue Horizontal Branch, and Extreme Horizontal Branch are shown in Figure 3.8 for NGC 2808, respectively in orange, teal, red, blue, cyan and magenta. The resolving power in this case is limited to the resolving power of Coelho (2014) grid, namely R $\approx$ 20 000.

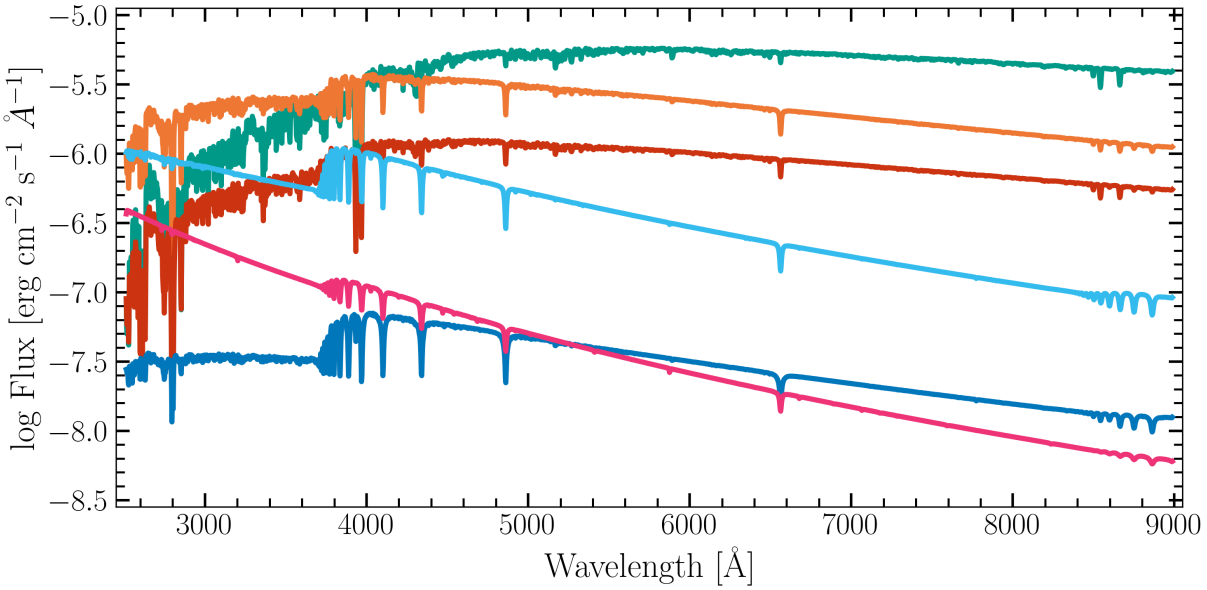

Figure 3.8: Integrated spectra for each evolutionary phase of the NGC 2808 colored as follows: Main Sequence in orange, Giant Branches in teal, red Horizontal Branch in red, Blue Stragglers in blue, blue Horizontal Branch in cyan and extreme Horizontal Branch in magenta.

Figure 3.9 shows the integrated light spectra for the six sub-samples of evolutionary phases of the M2. Compared to Figure 3.8, it follows the same color scheme and covers a wider wavelength range from the far ultraviolet to the infrared. The resolving power in this case is limited to the resolving power of Castelli and Kurucz (2003) grid (R ≈ 250).

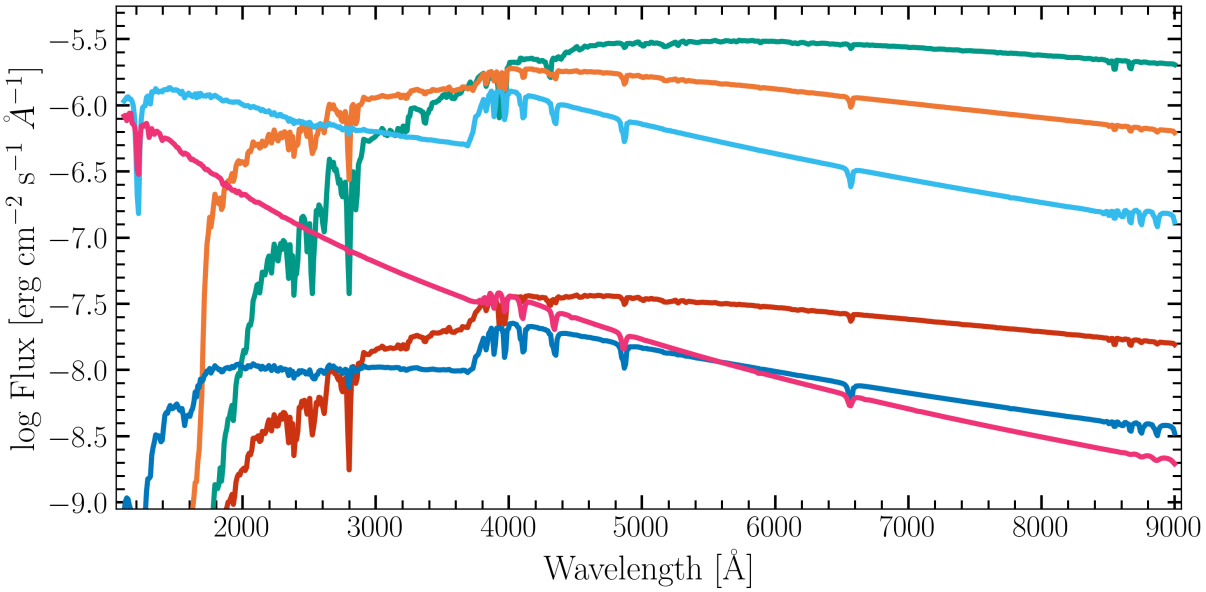

Figure 3.9: Integrated spectrum for each evolutionary phase of the M2. The colors follow the same scheme as in Figure 3.8.

The light from Main Sequence and Giant Branch dominates in the redder range, spanning both visible and infrared wavelengths. On the other hand, the Blue and Extreme Horizontal Branch are more prominent in the bluer range, thus affecting the UV part of the simple stellar population. This exhibition shows the impact of different evolutionary phases, revealing the diversity in the overall integrated light of a stellar population.

3.6 Results

3.6.1 The impact on the absorption lines

To quantify the contribution of each hot stellar component within the simple stellar population, we integrated simple stellar populations by considering different combinations of evolutionary phases. We computed a typical spectrum of a simple stellar population named base, consisting of the Main Sequence, Giant Branch, and Red Horizontal Branch. Additionally, we intended to analyze the effects of adding other hot evolutionary phases

to the base spectrum. We added the Blue Straggler, Blue Horizontal Branch, or Extreme Horizontal Branch to the base spectrum. Then, we compute a simple stellar population composed of all the evolutionary phases. With these five simple stellar populations, we can compare the relative fluxes, indicating the difference in the contribution of the simple stellar population compared to the base simple stellar population.

Models based on NGC 2808: In Figure 3.10, we show the five simple stellar populations based on the color-magnitude diagram of NGC 2808 that were degraded to R $\approx$ 1 000 for overall visualization. The grey solid line represents the base spectrum, the Blue Horizontal Branch is shown in a cyan dashed line, Blue Stragglers are displayed as the blue dot-dash line, and Extreme Horizontal Branch is illustrated as a magenta dotted line. The Blue Horizontal Branch has the most substantial contribution at the blue end of the model, amounting to 16.9%

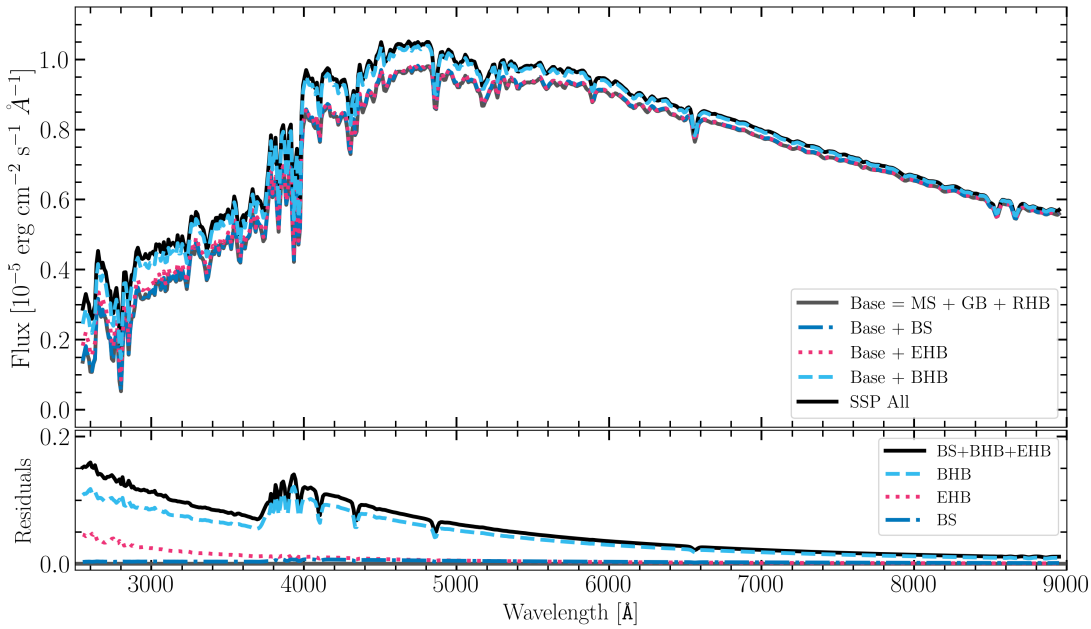

Figure 3.10: Simple stellar population base, others including Blue Straggler, Blue Horizontal Branch, or Extreme Horizontal Branch into the base spectrum, and the final spectrum with all the evolutionary phases for NGC 2808. The bottom panel shows the residuals comparing each stellar population to the base spectrum.

For better visualization of the line profiles, we show in Figures 3.11 and 3.16, the comparisons with a resolving power of R $\approx$ 6 000. The color scheme in the following figures is the same as in Figure 3.10. The bottom panels present the residuals, hence the difference between each simple stellar population with hot components and the base ones.

Figure 3.11 shows the Hα absorption line at 6 562.5Å normalized at 6 520.0Å. There are some differences in the wings of the line by including the hot stellar components. The differences are more prominent when the blue Horizontal Branch is added to the base spectrum. But, by including extreme Horizontal Branch and Blue Straggler stars, the wings are even broader with differences up to 0.6%. This is likely due to the inclusion of higher gravity atmospheres with significant pressure broadening.

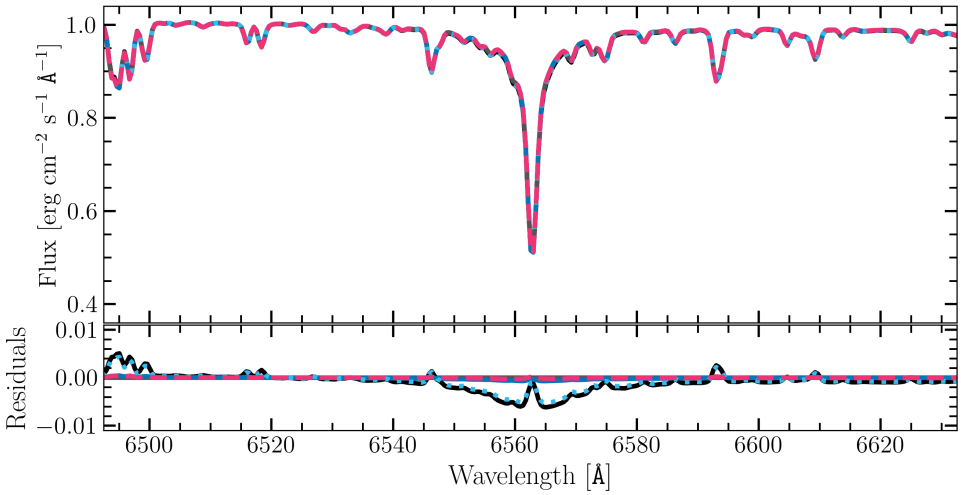

Figure 3.11: Hα absorption line at 6 562.5Å.

Figure 3.12 shows the Hβ absorption line at 4 860.7Å normalized at 4 820Å. In this case, the differences in the line wings are up to 2%.

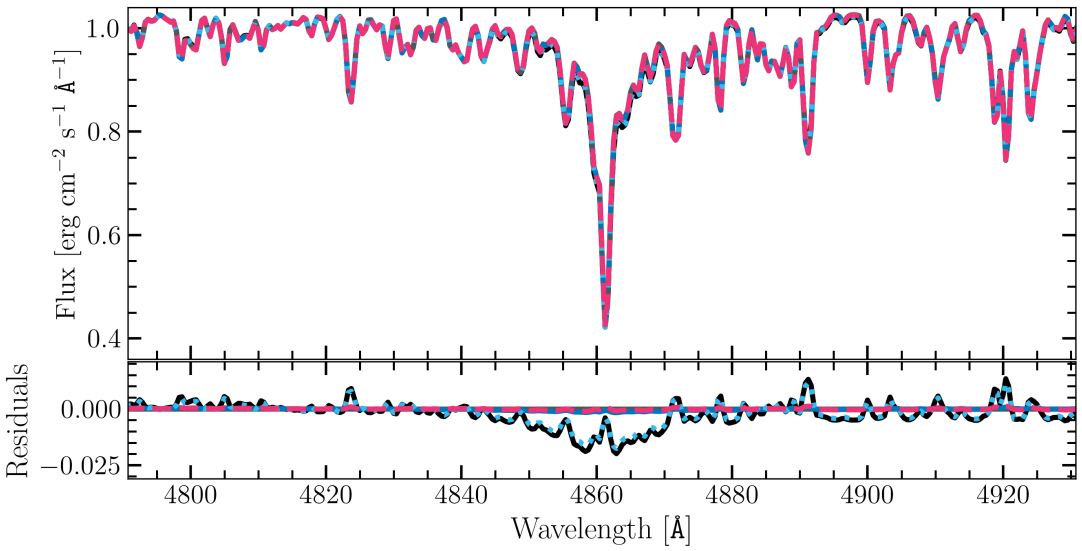

Figure 3.12: Hβ absorption line at 4 860.7Å.

Figure 3.13 shows the Hγ absorption line at 4 340.1Å normalized at 4 320Å. In this case, the differences in the line wings are up to 3%.

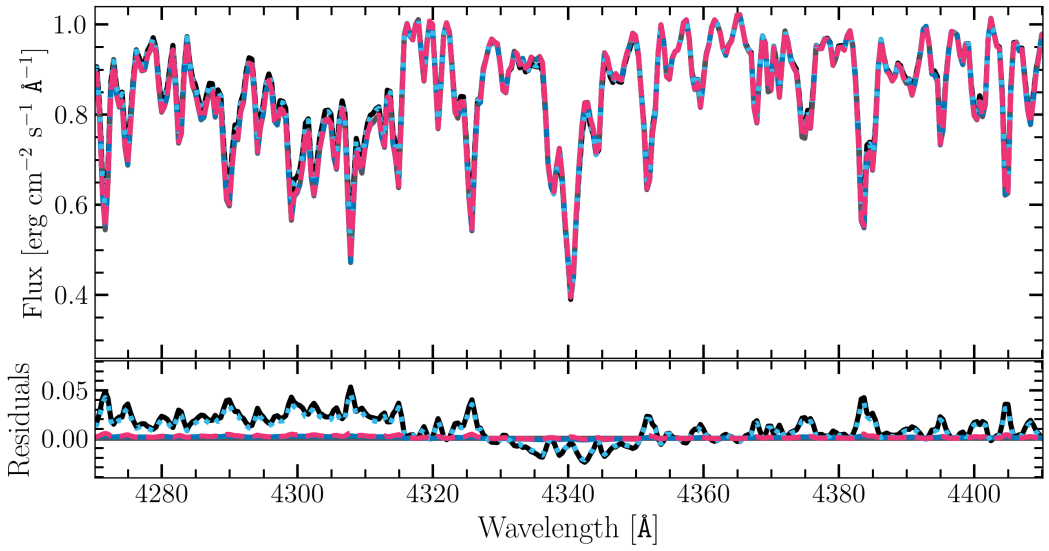

Figure 3.13: Hγ absorption line at 4 340.1Å.

Figure 3.14 shows the Hδ absorption line at 4 101.2Å normalized to 4 140Å. In this case, the differences in the line wings are up to 3%.

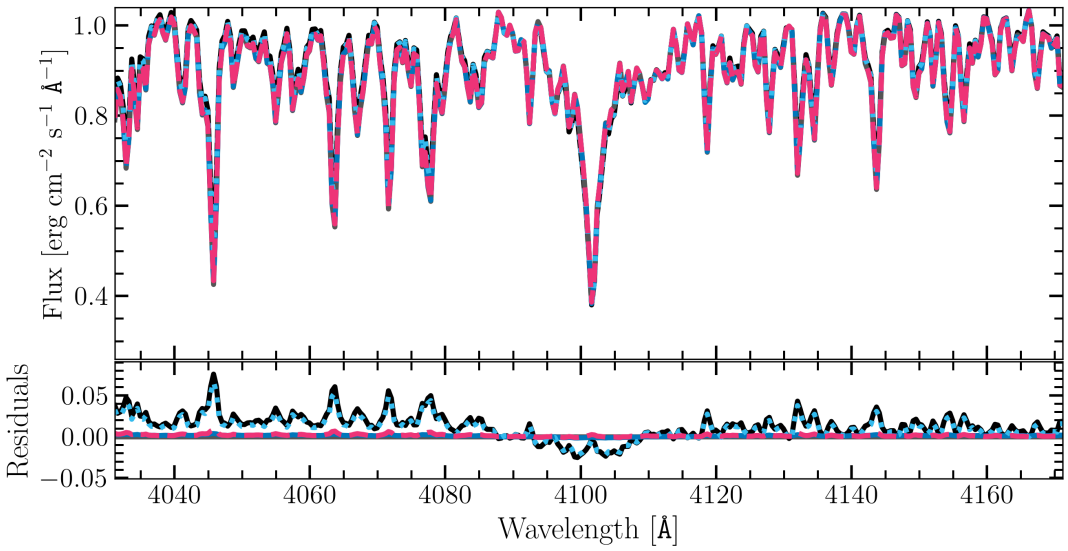

Figure 3.14: Hδ absorption line at 4 101.2Å.

Figure 3.15 shows the Ca absorption lines H and K normalized at 4 000Å. In this case, the differences are more prominent in the line center with narrower lines when the extreme Horizontal Branch is included and weaker lines with the inclusion of the blue Horizontal Branch. Such differences are up to 10%.

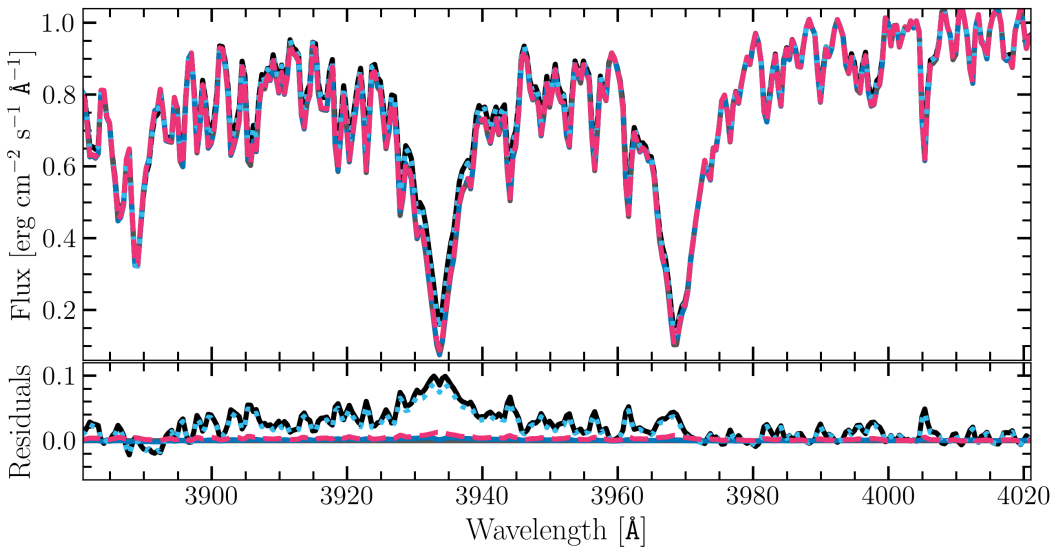

Figure 3.15: Doublet of Ca II absorption lines H at 3 968.5 Å and K at 3 933.7 Å.

Figure 3.16 shows the Mg absorption lines normalized at 2 830Å. In this case, as in the Ca lines, the differences in the line center are up to 20% with weaker lines with the

inclusion of the Horizontal Branch and other hot components.

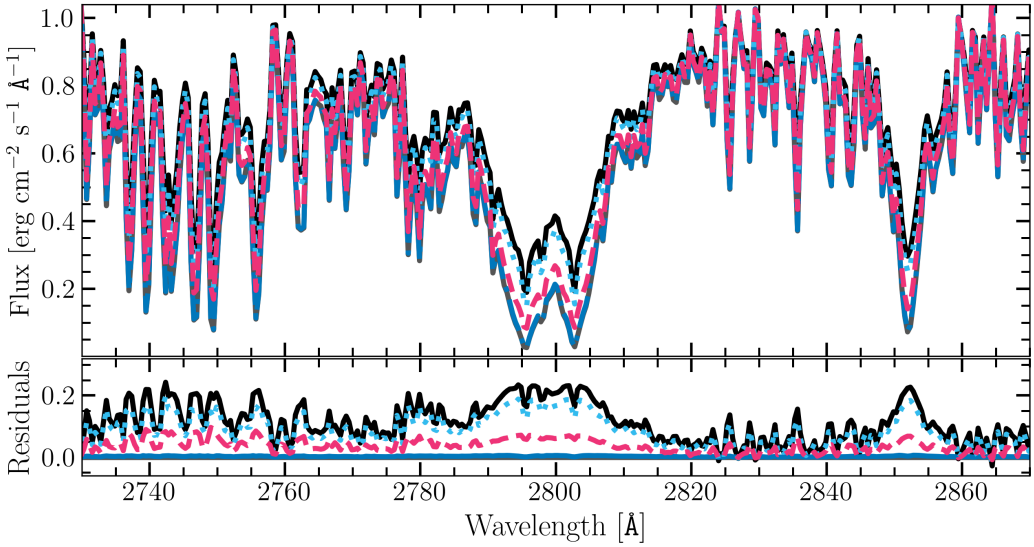

Figure 3.16: Mg II doublet absorption lines h at 2797 Å and k at 2 803 Å. Also, the Mg I absorption line at 2 852 Å.

The differences in the line profiles are even more prominent towards the ultraviolet.

Models based on M2: In Figure 3.17, we show the five simple stellar populations based on the CMD for M2, colored by the same scheme as in Figure 3.10. The results are similar to those findings for NGC 2808, but we have covered further into the ultraviolet parts of the spectrum. In this case, as mentioned in Section 3.5, the resolving power of the models of M2 is approximately 250. The Extreme Horizontal Branch flux is comparable to the Blue Horizontal Branch in the far-ultraviolet, supporting the need for including the hot components in the synthesis.

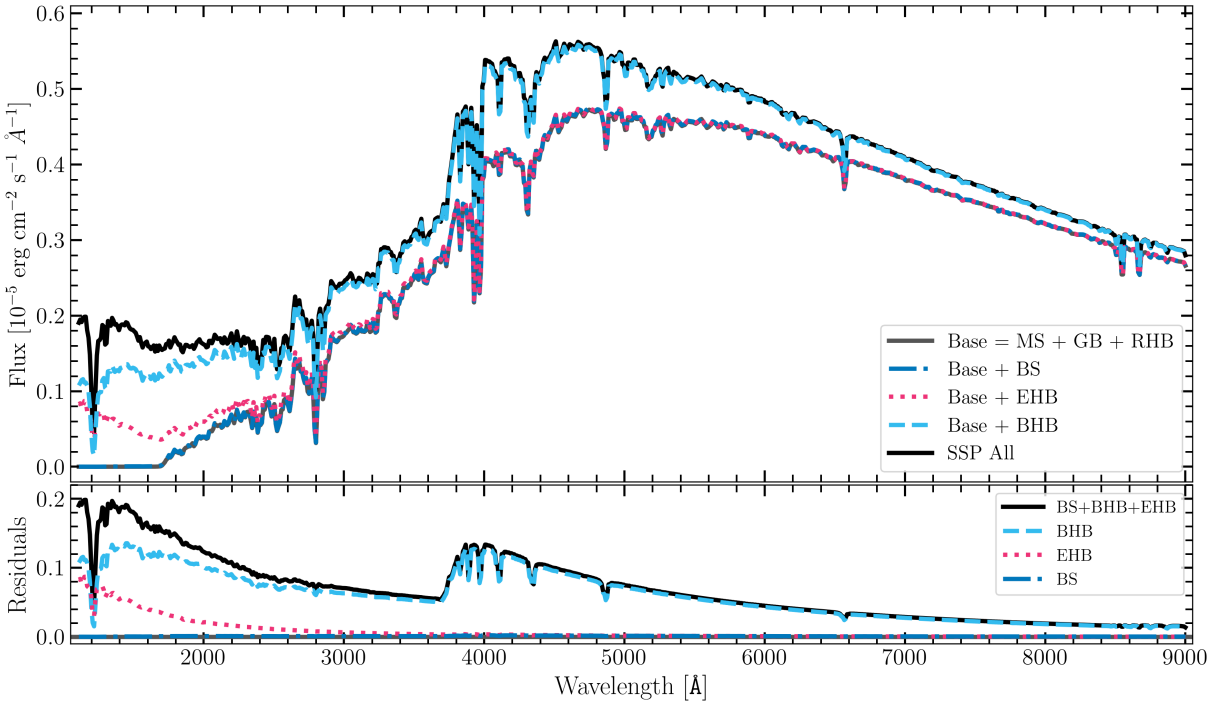

Figure 3.17: Simple stellar populations with different components for M2.

Figure 3.18 shows the Hα absorption line at 6 562.5Å normalized at 6 520.0Å. In this case, the differences in the line wings are up to 1.5%.

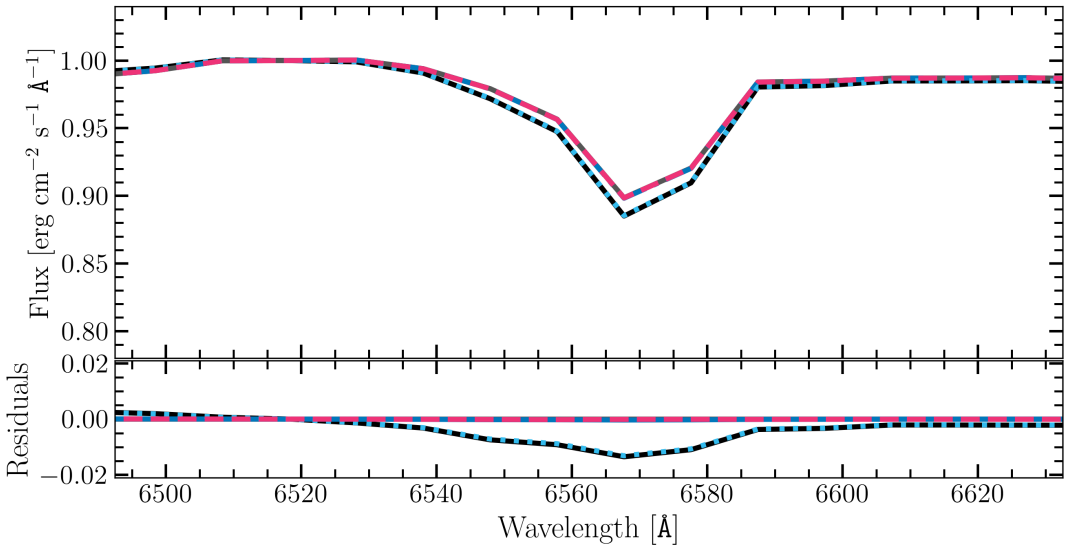

Figure 3.18: Hα absorption line at 6 562.5Å

Figure 3.19 shows the Hβ absorption line at 4 860.7Å normalized at 4 820Å. In this case, the differences in the line wings are up to 3%.

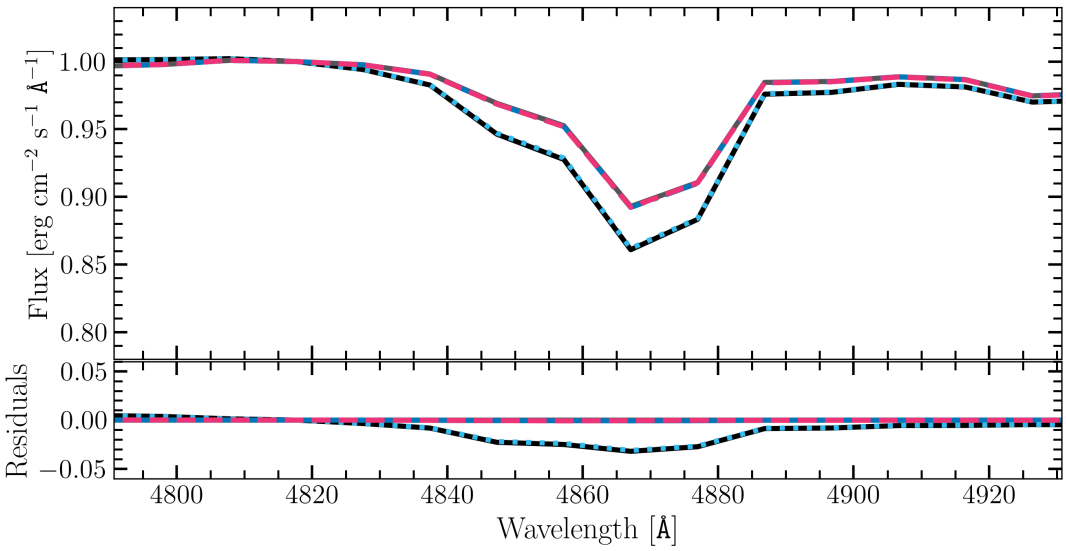

Figure 3.19: Hβ absorption line at 4 860.7Å.

Figure 3.20 shows the Hγ absorption line at 4 340.1Å normalized at 4 370Å. In this case, the differences in the line wings are up to 5%.

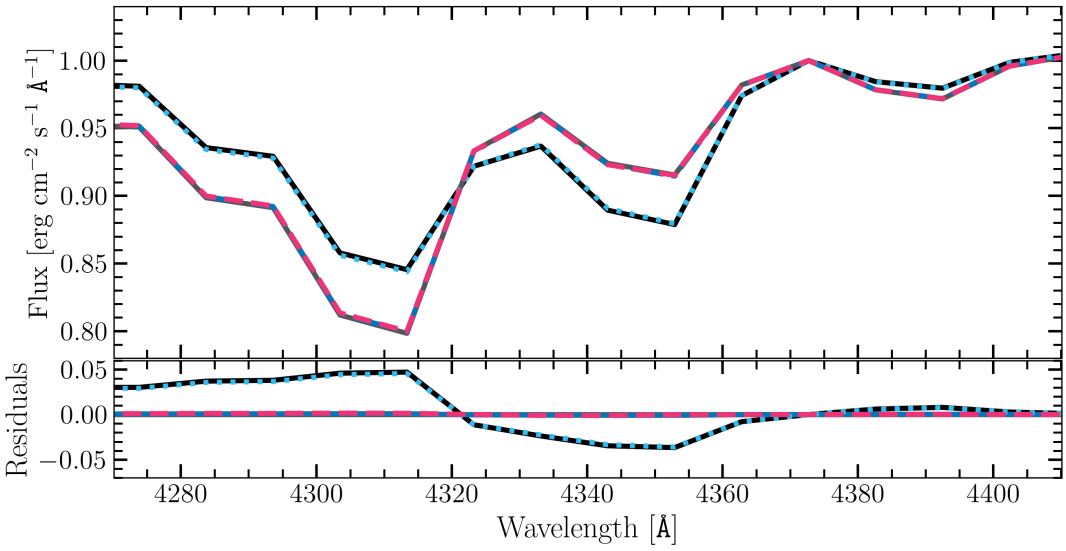

Figure 3.20: Hγ absorption line at 4 340.1Å.

Figure 3.21 shows the Hδ absorption line at 4 101.2Å normalized at 4 140Å. In this case, the differences in the line wings are up to 5%.

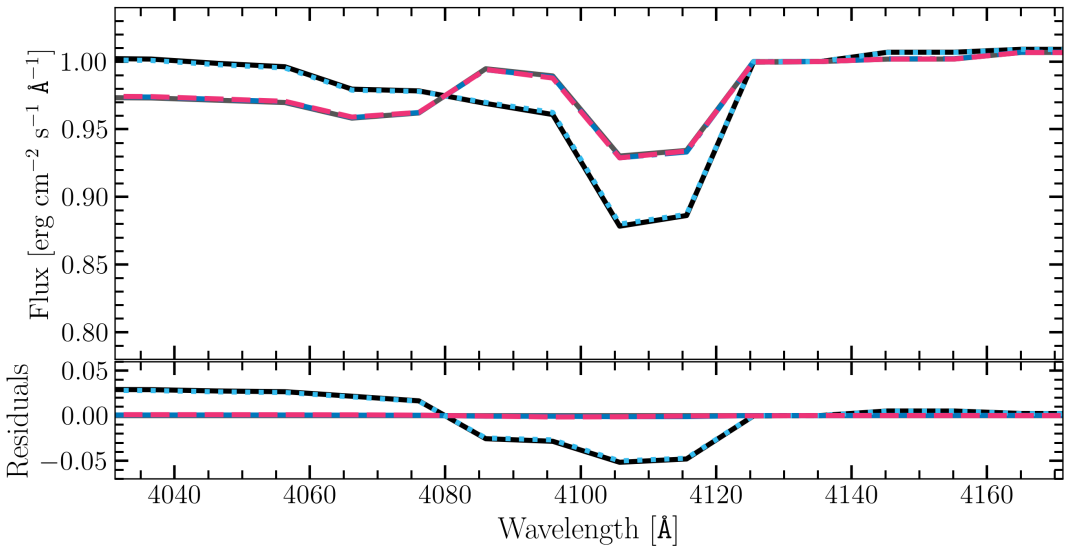

Figure 3.21: Hδ absorption line at 4 101.2Å.

Figure 3.22 shows the Ca absorption lines H and K normalized at 4 010Å. In this case, as in the NGC 2808 analysis, the differences are more prominent in the line center with shallower lines when the blue Horizontal Branch is included. The differences are up to 11%.

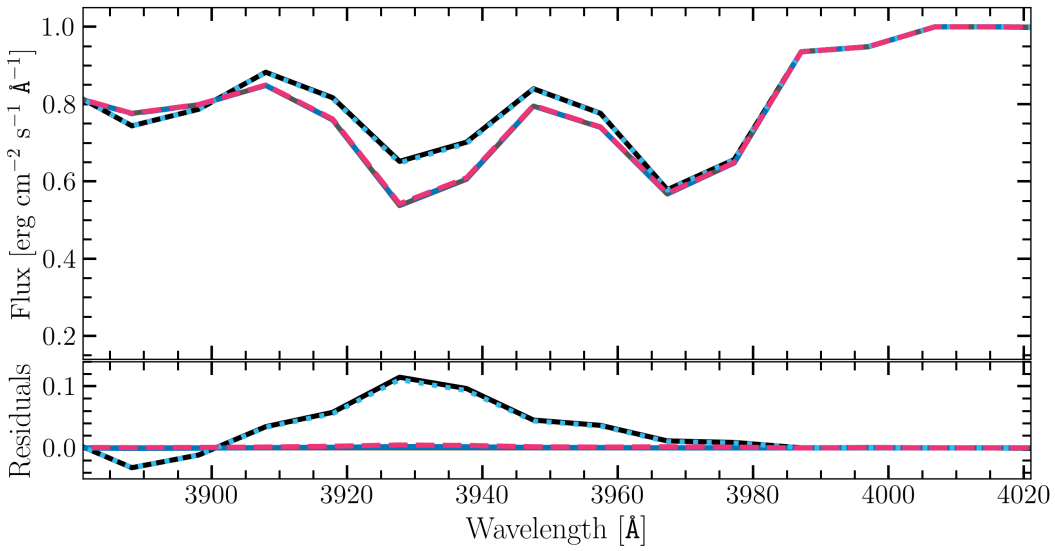

Figure 3.22: Doublet of Ca II absorption lines H at 3968.5 Å and K at 3933.7 Å.

Figure 3.23 shows the Mg absorption line normalized at 2 830Å. In this case, the differences in the line core reach 25%.

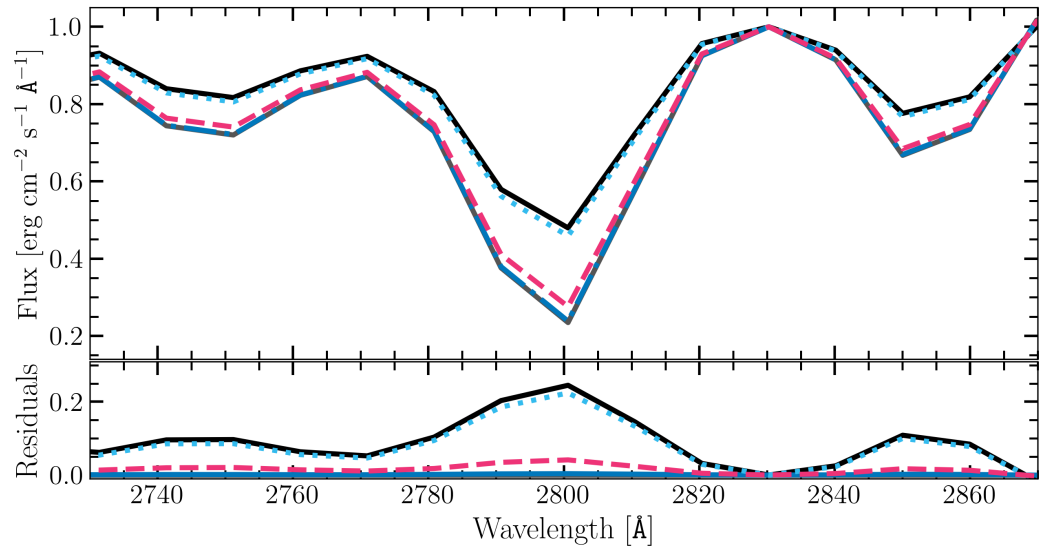

Figure 3.23: Mg II doublet absorption lines h at 2797 Å and k at 2803 Å. Also, the Mg I absorption line at 2852 Å.

Figure 3.24 show the Lyman α absorption line normalized at 1 145Å. The differences are more significant in this case when including the extreme Horizontal Branch to the base spectrum. The light is dominated by blue and extreme Horizontal Branch stars.

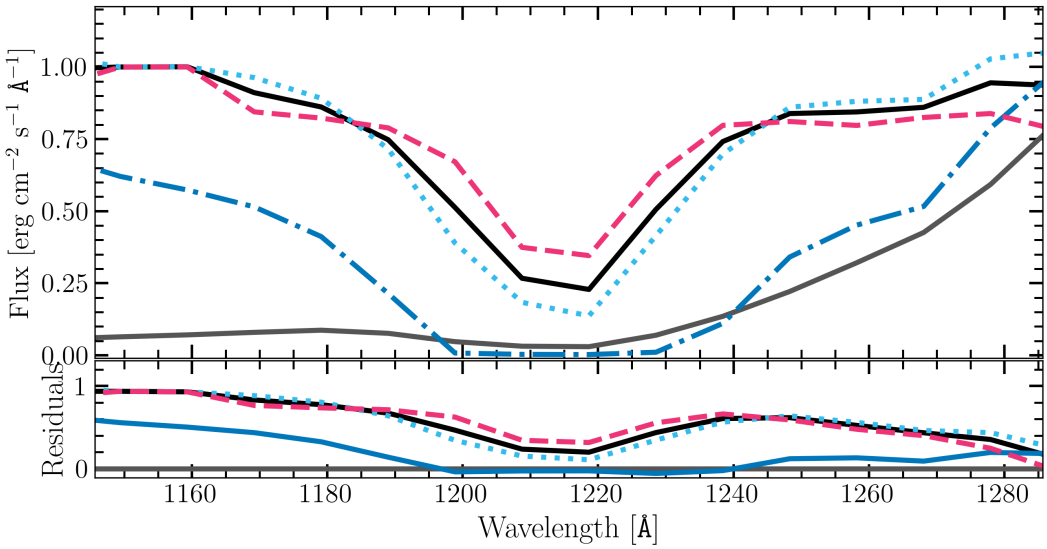

Figure 3.24: Lyman α absorption line at 1215.7 Å.

In summary, stark broadened lines show clear differences in flux and width, while metal lines are mostly affected in their intensity.

3.6.2 Comparison with observations

There are integrated light spectra of the Galactic globular cluster NGC 2808 available in the literature (Schiavon et al., 2005; Usher et al., 2017). However, the field of view of the Blanco Telescope used to extract the integrated spectrum is different from the Hubble Space Telescope used to tag the evolutionary phases in the color-magnitude diagram. Therefore, the modeled spectrum is not comparable to the observed spectrum, but it is a sanity check for our stellar population models.

Figure 3.25 shows the Schiavon et al. (2005) observed spectrum in grey and our synthetic simple stellar population in magenta, which comprises all evolutionary phases. We can see a fair agreement between Schiavon et al. (2005) and synthetic simple stellar population spectra, including the bluest region of the spectrum.

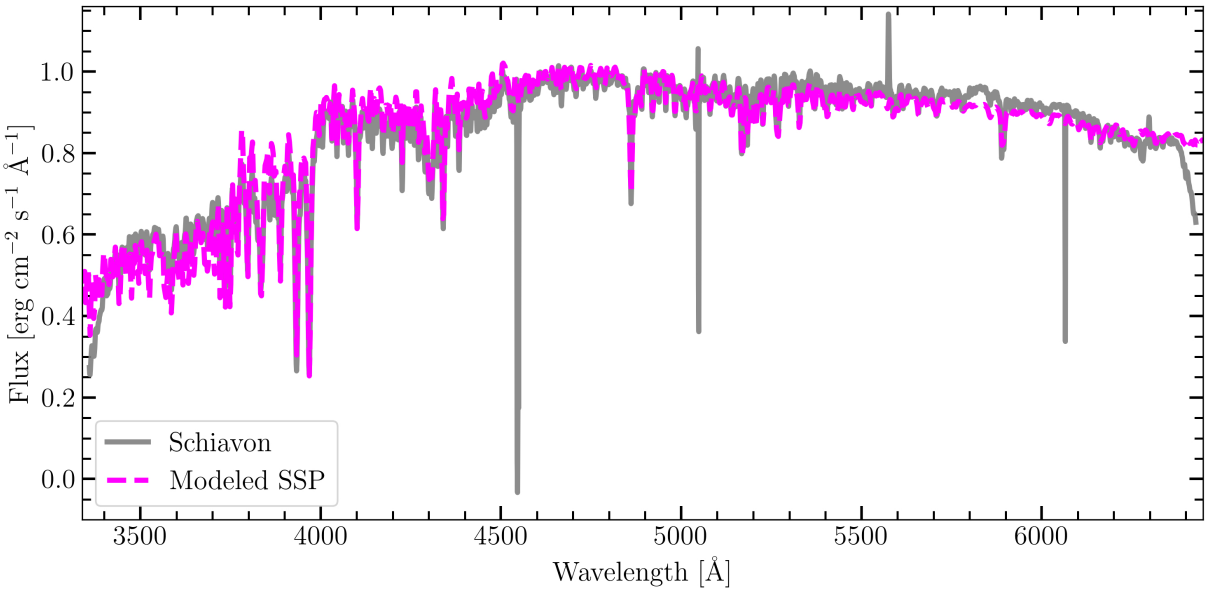

Figure 3.25: Synthetic simple stellar population in magenta compared to the observed integrated spectrum of NGC 2808 in the optical and infrared regions.

The same comparison for M2 also shows a good agreement with the observations (Figure 3.26). In this case, the match could be extended to the ultraviolet using the optical integrated spectrum (Schiavon et al., 2005; Usher et al., 2017) and ultraviolet spectrum observed by IUE. This was the first time the integrated light spectrum of a globular cluster was modeled in this level of detail from the ultraviolet to the optical range.

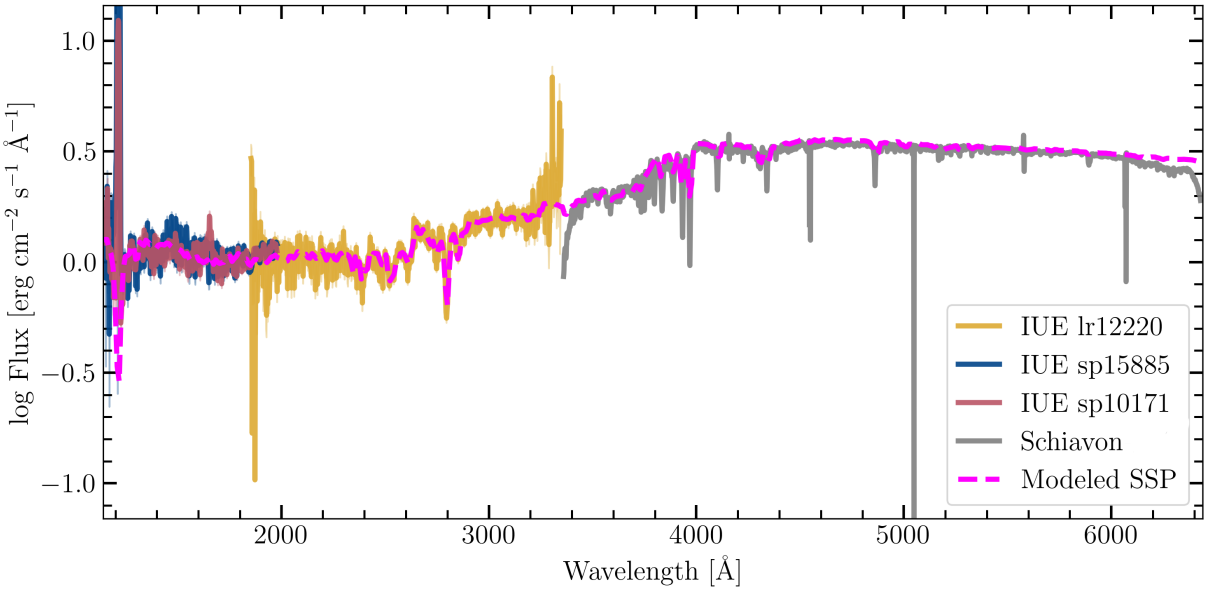

Figure 3.26: Synthetic simple stellar population in magenta compared to the observed integrated spectrum of M2 from the far-ultraviolet to infrared regions.

3.7 Summary

We modeled the integrated light of different evolutionary phases relevant to Galactic globular clusters, based on high-quality color-magnitude diagrams and state-of-the-art synthetic stellar libraries. We took care to include hot and high gravity models in stellar synthesis, thus being able to simulate simple stellar populations with different morphologies of the Horizontal Branch. This allowed us to quantify the impact of Blue and Extreme Horizontal Branches in the integrated flux, which can reach up to 100% in the far-ultraviolet, wavelengths below 1 700Å (Pacheco *et al.* (b), in prep). We expect that this approach brings improvement in stellar population synthesis models, helping to break the degeneracy between age and Horizontal Branch morphology which is known to affect the integrated light of old stellar populations.

Chapter 4

Conclusions

The central topic of this doctoral research was to study the integrated light properties of old stellar populations, carefully considering hot-evolved stars such as Subdwarfs. These stars are important to consider in population synthesis as they may be present within old stellar populations and contribute significantly to the ultraviolet and blue parts of the spectrum. However, stellar population synthesis based on isochrones does not often consider their contribution, due to the current inability of stellar evolution tracks to predict their presence in stellar populations from first principles. Failing to consider these components may result in underestimating ages in integrated light studies.

To overcome this limitation, a homogeneous library of hot, low-mass high-gravity atmosphere structure models and synthetic spectra was computed, extending from the ultraviolet to near-infrared. The radiative transfer in the atmosphere models underwent meticulous customization, which included non-LTE modeling for the energy states of important atoms (H, He, C, N, O, Ne, Mg, Al, Si, S, and Fe) to correctly calculate their contribution to the opacity. This is particularly significant in calculations of models for the hottest stars, which produce a difference in the line-core photons absorbed and contribute to the bluer continuum. The high-resolution spectra were computed considering an extended line-blanketed synthesis of the emergent spectra, and this grid was published in Pacheco et al. (2021) and complemented in Pacheco et al. (2021).

This grid was then employed in the modeling of integrated light based on color-magnitude diagrams of the old globular clusters NGC 2808 and NGC 7089. To compute stellar population integrated models, I proposed improvements in the synthesis methods based on the color-magnitude diagrams. Starting from methods in the literature (Martins et al., 2019), we devised the following updates (Pacheco et al., 2024, Pacheco et al. (a), in

prep.):

- The grid of spectra for hot and high gravity stellar models was included in the stellar population synthesis;
- Each observed star was directly matched to a synthetic spectrum using multi-band photometric data in a 10-dimensional color system using a nearest neighbors method;

The stars in the observed color-magnitude diagrams have been tagged according to their evolutionary phase, allowing us to compute one integrated light model for each of these phases. This allows us to quantify the impact of the evolutionary phases in the integrated flux, which is dominated by the Blue and Extreme Horizontal Branches in the far ultraviolet. This impact has been shown to vary across the blue part of the spectrum, contributing up to 100% in the far-ultraviolet, but still showing significant contributions in the near-ultraviolet of around 20%. This further enforces the necessity to include such components in population synthesis. Finally, the synthetic integrated spectrum of the stellar populations including these hot components has been computed. These models show remarkable agreement with observations over a very long baseline, from 1 200 to 6 300 Å and this method can form a suitable basis from which to build upon in further work, as outlined in Section 5.

Chapter 5

Future work

The following stages were not completed during the doctoral research but are slated for imminent completion.

The studies performed in Section 3.6.1 will be better quantified in terms of equivalent width measurements. Equivalent width measurements are a classic diagnostic, in which its utility is an exploratory role of spatially unresolved populations, offering insights into globular cluster properties such as age estimation. In this multifaceted role, equivalent widths are usually straightforward and robust, but such analysis must be done carefully and with caveats in mind. Also, it is essential to publish the methodology described in Chapter 3 to ensure its dissemination and potential use by other researchers in the field.

We plan on building additional simple stellar population models based on the color-magnitude diagrams of globular clusters with different ages, metallicities, and Horizontal Branch morphologies, thus producing a library that encompasses a broader range of stellar population parameters. The purpose is to apply our methodology combining the state-of-the-art single stellar spectra with a reliable grid of hot horizontal branch models based on their observed photometric properties. This new generation of synthesis of Horizontal Branch integrated spectra will be an innovative grid of semi-empirical single stellar population models. This aims to address the long-standing challenge of disentangling the age and horizontal branch morphology degeneracy in the integrated optical spectra of old stellar populations.

Another task involves investigating whether the new models can effectively address the issues highlighted in the work of Ocvirk (2010) and Gonçalves et al. (2020), potentially offering solutions to the age discrepancies in the study of metal-poor globular clusters. There is an intention to examine how the spectroscopic ages behave when the blue and

extreme Horizontal Branches are included in the stellar population. Furthermore, the search for features, such as colors or indices, that may aid in distinguishing between the age and morphology of the horizontal branch is essential for more accurate analyses and interpretations.

Applying the novel methodology presented in this thesis in the study of globular clusters in M31 could offer further validation and insights. As the closest Milky Way analog from which we can obtain high-quality integrated photometric and spectroscopic data, M31 holds great significance. Understanding the formation and evolution of the M31 ecosystem is pivotal as it greatly influences our comprehension of the local group as a whole. By analyzing its globular clusters, we have the opportunity to understand the history of M31 through a series of merging events. M31 likely had a more active history of accretion compared to our Galaxy, evident in the abundance of its halo substructure. Therefore, it provides an ideal laboratory for examining how Milky Way-like late-type galaxies can evolve.

The computation of distances in multi-dimensional color space (see Section 3.4.2) triggered explorations of using a neural network-trained model to infer stellar atmospheric parameters from colors. We plan on evaluating the neural network for performance, necessary to verify its effectiveness and reliability in future analyses. This is necessary to verify its effectiveness and reliability in future analyses.

Another project that is a potentially promising endeavor would be the analysis of the chemical differences between Giant Branch and Hot Subdwarf stars in globular clusters. As Subdwarfs may not follow the evolution of isolated stars, such differences are still unexplored. I propose to employ a neural network-trained model to determine Subdwarf's surface gravity and effective temperatures, thus computing advanced non-LTE atmosphere models for them. Thereby, by using the spectra to estimate the abundances I can tag their chemical abundance differences in stars within a globular cluster. This chemical diagnostics can improve our knowledge of the evolution of these stripped stars, that experienced such a large mass-loss rate.

Bibliography

Allard N. F., Noselidze I., Kruk J. W., New study of the quasi-molecular Lyman-γ satellites due to H-H^+ collisions, A&A, 2009, vol. 506, p. 993

Asplund M., Grevesse N., Sauval A. J., Scott P., The Chemical Composition of the Sun, Annual Review of Astronomy and Astrophysics, 2009, vol. 47

Baade W., The resolution of Messier 32, NGC 205, and the central region of the Andromeda, The Astrophysical Journal, 1944, vol. 100, p. 137

Bagnulo S., Jehin E., Ledoux C., et al. The UVES Paranal Observatory Project: A Library of High- Resolution Spectra of Stars across the Hertzsprung-Russell Diagram, The Messenger, 2003, vol. 114, p. 10

Barbary K., , 2016 extinction v0.3.0

Barbuy B., Perrin M.-N., Katz D., Coelho P., Cayrel R., Spite M., Van't Veer-Menneret C., A grid of synthetic spectra and indices Fe5270, Fe5335, Mgb and Mg_2 as a function of stellar parameters and [alpha/Fe], A&A, 2003, vol. 404, p. 661

Barnard A., Cooper J., Smith E., The Broadening of He I lines including ion dynamic corrections, with application to λ4471Å, Journal of Quantitative Spectroscopy and Radiative Transfer, 1974, vol. 14, p. 1025

Bastian N., Lardo C., Multiple Stellar Populations in Globular Clusters, ARA&A, 2018, vol. 56, p. 83

Baum W. A., Population Inferences from Star Counts, Surface Brightness and Colors, PASP, 1959, vol. 71, p. 106

Bautista M. A., Atomic data from the Iron Project. XVI. Photoionization cross sections and oscillator strengths for Fe V., A&AS, 1996, vol. 119, p. 105

Bautista M. A., Pradhan A. K., Atomic data from the Iron Project. XXVI. Photoionization cross sections and oscillator strengths for Fe IV, A&AS, 1997, vol. 126, p. 365

Bergeron P., Wesemael F., Fontaine G., On the influence of the convective efficiency on the determination of the atmospheric parameters of DA white dwarfs, ApJ, 1992, vol. 387, p. 288

Bessell M. S., Castelli F., Plez B., Model atmospheres broad-band colors, bolometric corrections and temperature calibrations for O - M stars, A&A, 1998, vol. 333, p. 231

Bica E., Population synthesis in galactic nuclei using a library of star clusters., A&A, 1988, vol. 195, p. 76

Bica E., Bonatto C., Giovannini O., A library of IUE white dwarf spectra for stellar population analyses., A&AS, 1996, vol. 119, p. 211

Bohlin R. C., Gordon K. D., Tremblay P.-E., Techniques and Review of Absolute Flux Calibration from the Ultraviolet to the Mid-Infrared, PASP, 2014, vol. 126, p. 711

Borisov S. B., Chilingarian I. V., Rubtsov E. V., et al. New Generation Stellar Spectral Libraries in the Optical and Near-infrared. I. The Recalibrated UVES-POP Library for Stellar Population Synthesis*, The Astrophysical Journal Supplement Series, 2023, vol. 266, p. 11

Bruzual G., Charlot S., Spectral Evolution of Stellar Populations Using Isochrone Synthesis, ApJ, 1993, vol. 405, p. 538

Bruzual G., Charlot S., Stellar population synthesis at the resolution of 2003, MNRAS, 2003, vol. 1028, p. 1000

Bruzual G. A., Spectral evolution of galaxies. I. Early-type systems., ApJ, 1983, vol. 273, p. 105

Busso G., Moehler S., Zoccali M., et al. Hot Subdwarfs in the Galactic Bulge, ApJ, 2005, vol. 633, p. L29

Butler K., Mendoza C., Zeippen C. J., Atomic data for opacity calculations. XIX. The magnesium isoelectronic sequence, Journal of Physics B Atomic Molecular Physics, 1993, vol. 26, p. 4409

Byrne C. M., Jeffery C. S., Tout C. A., Hu H., The effects of diffusion in hot subdwarf progenitors from the common envelope channel, MNRAS, 2018, vol. 475, p. 4728

Cabrera-Ziri I., Conroy C., Deriving ages and horizontal branch properties of integrated stellar populations, MNRAS, 2022, vol. 511, p. 341

Carretta E., Five Groups of Red Giants with Distinct Chemical Composition in the Globular Cluster NGC 2808, ApJ, 2015, vol. 810, p. 148

Castelli F., Hubrig S., A spectroscopic atlas of the HgMn star HD 175640 (B9 V) $\lambda\lambda$ 3040-10 000 Å, A&A, 2004, vol. 425, p. 263

Castelli F., Kurucz R. L., New Grids of ATLAS9 Model Atmospheres. In Modelling of Stellar Atmospheres , vol. 210, 2003, p. A20

Cenarro A. J., Peletier R. F., Sanchez-Blazquez P., et al. Medium-resolution Isaac Newton Telescope library of empirical spectra - II. The stellar atmospheric parameters, MNRAS, 2007, vol. 374, p. 664–690

Charlot S., Bruzual G., Stellar Population Synthesis Revisited, ApJ, 1991, vol. 367, p. 126

Charpinet S., Fontaine G., Brassard P., et al. Structural parameters of the hot pulsating B subdwarf PG 1219+534 from asteroseismology, A&A, 2005, vol. 437, p. 575

Chen Y.-P., Trager S. C., Peletier R. F., Lançon A., Vazdekis A., Prugniel P., Silva D. R., Gonneau A., The X-shooter Spectral Library (XSL). I. DR1: Near-ultraviolet through optical spectra from the first year of the survey, A&A, 2014, vol. 565, p. A117

Cid Fernandes R., Mateus A., Sodré L., Stasińska G., Gomes J. M., Semi-empirical analysis of Sloan Digital Sky Survey galaxies - I. Spectral synthesis method, MNRAS, 2005, vol. 358, p. 363

Coelho P., Model stars for the modelling of galaxies: α-enhancement in stellar populations models. In Revista Mexicana de Astronomia y Astrofisica Conference Series , vol. 35 of Revista Mexicana de Astronomia y Astrofisica Conference Series, 2009a, p. 133

Coelho P., Spectral libraries and their uncertainties. In Probing Stellar Populations Out to the Distant Universe: Cefalu 2008, Proceedings of the International Conference , vol. 1111 of American Institute of Physics Conference Series, 2009b, p. 67

Coelho P., Barbuy B., Meléndez J., et al. A library of high resolution synthetic stellar spectra from 300 nm to 1.8 μm with solar and α-enhanced composition, A&A, 2005, vol. 443, p. 735

Coelho P., Barbuy B., Meléndez J., Schiavon R. P., Castilho B. V., A library of high resolution synthetic stellar spectra from 300 nm to 1.8 μm with solar and α-enhanced composition, A&A, 2005, vol. 443, p. 735

Coelho P., Bruzual G., Charlot S., et al. Spectral models for solar-scaled and α-enhanced stellar populations, MNRAS, 2007, vol. 382, p. 498

Coelho P. R. T., A new library of theoretical stellar spectra with scaled-solar and α-enhanced mixtures, MNRAS, 2014, vol. 440, p. 1027

Coelho P. R. T., Bruzual G., Charlot S., To use or not to use synthetic stellar spectra in population synthesis models?, MNRAS, 2020, vol. 491, p. 2025

Colucci J. E., Bernstein R. A., McWilliam A., VizieR Online Data Catalog: High-resolution GC abundances. II., VizieR Online Data Catalog, 2017, p. J/ApJ/834/105

Crampin J., Hoyle F., On the change with time of the integrated colour and luminosity of an M67-type star group, MNRAS, 1961, vol. 122, p. 27

Culpan R., Geier S., Reindl N., et al. The population of hot subdwarf stars studied with Gaia, A&A, 2022, vol. 662, p. A40

de Freitas Pacheco J. A., Barbuy B., Horizontal branch morphology and Hβ indices of globular clusters., A&A, 1995, vol. 302, p. 718

Dorsch M., Latour M., Heber U., Spectral analysis of the He-enriched sdO-star HD 127493, Open Astronomy, 2018, vol. 27, p. 19

Dorsch M., Latour M., Heber U., Heavy metals in intermediate He-rich hot subdwarfs: The chemical composition of HZ44 and HD127493, Astronomy and Astrophysics, 2019

Edelmann H., Heber U., Hagen H. J., et al. Spectral analysis of sdB stars from the Hamburg Quasar Survey, A&A, 2003, vol. 400, p. 939

Faber S. M., Quadratic programming applied to the problem of galaxy population synthesis., A&A, 1972, vol. 20, p. 361

Falcón-Barroso J., Sánchez-Blázquez P., Vazdekis A., et al. An updated MILES stellar library and stellar population models, A&A, 2011, vol. 532, p. A95

Fernley J. A., Hibbert A., Kingston A. E., Seaton M. J., Atomic data for opacity calculations: XXIV. The boron-like sequence, Journal of Physics B Atomic Molecular Physics, 1999, vol. 32, p. 5507

Fitzpatrick E. L., Massa D., An Analysis of the Shapes of Interstellar Extinction Curves. V. The IR-through-UV Curve Morphology, ApJ, 2007, vol. 663, p. 320

Fontaine G., Bergeron P., Brassard P., et al. Testing Seismic Models of Hot B Subdwarfs with Gaia Data, ApJ, 2019, vol. 880, p. 79

Fontaine G., Brassard P., Charpinet S., et al.. A preliminary look at the empirical mass distribution of hot B subdwarf stars, A&A, 2012, vol. 539, p. A12

Fontaine G., Villeneuve B., Wilson J., On the acoustic flux of Sirius A., ApJ, 1981, vol. 243, p. 550

Gaia Collaboration Brown A. G. A., Vallenari A., et al. Gaia Data Release 2. Summary of the contents and survey properties, A&A, 2018, vol. 616, p. A1

Gaia Collaboration Brown A. G. A., Vallenari A., et al. Gaia Early Data Release 3. Summary of the contents and survey properties, A&A, 2021, vol. 649, p. A1

Gaia Collaboration Carrasco M. J., Evans et al. Gaia Data Release 1. Principles of the photometric calibration of the G band, A&A, 2016, vol. 595, p. A7

Geier S., The population of hot subdwarf stars studied with Gaia. III. Catalogue of known hot subdwarf stars: Data Release 2, A&A, 2020, vol. 635, p. A193

Geier S., Heber U., Podsiadlowski P., et al. Hot subdwarf stars in close-up view. I. Rotational properties of subdwarf B stars in close binary systems and nature of their unseen companions, A&A, 2010, vol. 519, p. A25

Geier S., Østensen R. H., Nemeth P., et al. Meet the family - the catalog of known hot subdwarf stars, Open Astronomy, 2017a, vol. 26, p. 164

Geier S., Østensen R. H., Nemeth P., et al. Meet the family - the catalog of known hot subdwarf stars, OAst, 2017b, vol. 26, p. 164

Geier S., Raddi R., Gentile Fusillo N. P., Marsh T. R., The population of hot subdwarf stars studied with Gaia. II. The Gaia DR2 catalogue of hot subluminous stars, A&A, 2019, vol. 621, p. A38

Gonçalves G., Coelho P., Schiavon R., Usher C., How well can we determine ages and chemical abundances from spectral fitting of integrated light spectra?, MNRAS, 2020, vol. 499, p. 2327

Green E. M., Fontaine G., Hyde E. A., et al. Hot Subdwarf Stars and Related Objects ASP Conference Systematics of Hot Subdwarfs Obtained from a Large Low Resolution Survey, ASP Conference Series, 2008, vol. 392

Greenstein J. L., Sargent A. I., The Nature of Faint Blue Stars in the Halo. II, ApJS, 1974, vol. 28, p. 157

Greggio L., Renzini A., Clues on the Hot Star Content and the Ultraviolet Output of Elliptical Galaxies, ApJ, 1990, vol. 364, p. 35

Grevesse N., Sauval A. J., Standard solar composition, Space Science Reviews, 1998, vol. 100

Gustafsson B., Edvardsson B., Eriksson K., et al. A grid of MARCS model atmospheres for late-type stars, A&A, 2008, vol. 486, p. 951

Hall P. D., Jeffery C. S., Hydrogen in hot subdwarfs formed by double helium white dwarf mergers, MNRAS, 2016, vol. 463, p. 2756

Han Z., Podsiadlowski P., Maxted P. F. L., et al. The origin of subdwarf B stars - I. The formation channels, MNRAS, 2002, vol. 336, p. 449

Han Z., Podsiadlowski P., Maxted P. F. L., Marsh T. R., The origin of subdwarf B stars - II, MNRAS, 2003, vol. 341, p. 669

Hauck B., Mermilliod M., Uvbybeta photoelectric photometric catalogue, A&AS, 1998, vol. 129, p. 431

Heber U., Hot Subdwarf Stars, ARA&A, 2009, vol. 47, p. 211

Heber U., Hot Subluminous Stars, Publications of the Astronomical Society of the Pacific, 2016, vol. 128, p. 082001

Heber U., Irrgang A., Schaffenroth J., Spectral energy distributions and colours of hot subluminous stars, Open Astronomy, 2017, vol. 1, p. 1

Hernández-Pérez F., Bruzual G., Revisiting binary stars in population synthesis models, MNRAS, 2013, vol. 431, p. 2612

Hibbert A., Scott M. P., Atomic data for opacity calculations. XXI. The neon sequence, Journal of Physics B Atomic Molecular Physics, 1994, vol. 27, p. 1315

Hubeny I., A computer program for calculating non-LTE model stellar atmospheres, Computer Physics Communications, 1988, vol. 52, p. 103

Hubeny I., Accelerated Lambda Iteration: An Overview. In Stellar Atmosphere Modeling , vol. 288 of PASP, 2003, p. 17

Hubeny I., Heap S. R., Lanz T., Non-LTE Line-Blanketed Model Atmospheres of O Stars. In Properties of Hot Luminous Stars , vol. 131 of PASP, 1998, p. 108

Hubeny I., Hummer D. G., Lanz T., NLTE model stellar atmospheres with line blanketing near the series limits., A&A, 1994, vol. 282, p. 151

Hubeny I., Lanz T., Non-LTE Line-blanketed Model Atmospheres of Hot Stars. I. Hybrid Complete Linearization/Accelerated Lambda Iteration Method, ApJ, 1995, vol. 439, p. 875

Hubeny I., Lanz T., , 2011a Synspec: General Spectrum Synthesis Program

Hubeny I., Lanz T., , 2011b TLUSTY: Stellar Atmospheres, Accretion Disks, and Spectroscopic Diagnostics

Hubeny I., Lanz T., , 2017a TLUSTY User's Guide II: Reference Manual

Hubeny I., Lanz T., , 2017b TLUSTY User's Guide III: Operational Manual

Hubeny I., Mihalas D., Theory of Stellar Atmospheres. Princeton series in astrophysics, 2014

Hubeny I., Mihalas D., Theory of stellar atmospheres: an introduction to astrophysical non-equilibrium quantitative spectroscopic analysis. Princeton University Press, 2014

Humason M. L., Zwicky F., A Search for Faint Blue Stars., ApJ, 1947, vol. 105, p. 85

Husser T. O., Wende-von Berg S., Dreizler S., et al. A new extensive library of PHOENIX stellar atmospheres and synthetic spectra, A&A, 2013, vol. 553, p. A6

Iben I. J., On the frequency of planetary nebula nuclei powered by helium burningand on the frequency of white dwarfs with hydrogen-deficient atmospheres., ApJ, 1984, vol. 277, p. 333

Johnson C., Green E., Wallace S., et al. Photometric Survey to Search for Field sdO Pulsators. In 6th Meeting on Hot Subdwarf Stars and Related Objects , vol. 481 of PASP, 2014, p. 153

Johnson H. L., Astronomical Measurements in the Infrared, ARA&A, 1966, vol. 4, p. 193

Kato S., Fukue J., Fundamentals of Astrophysical Fluid Dynamics: Hydrodynamics, Magnetohydrodynamics, and Radiation Hydrodynamics. Springer Nature Singapore, 2020

Kilkenny D., Heber U., Drilling J. S., A catalogue of spectroscopically identified hot subdwarf stars., South African Astronomical Observatory Circular, 1988, vol. 12, p. 1

Kurucz R., Atomic Data for Fe and Ni., Atomic Data for Fe and Ni. Kurucz CD-ROM No. 22. Cambridge, 1994, vol. 22

Kurucz R. L., Including all the lines: data releases for spectra and opacities, Canadian Journal of Physics, 2017, vol. 95, p. 825

Lanz T., Hubeny I., Non-LTE Line-blanketed Model Atmospheres of Hot Stars. II. Hot, Metal-rich White Dwarfs, ApJ, 1995, vol. 439, p. 905

Lanz T., Hubeny I., A Grid of Non-LTE Line-blanketed Model Atmospheres of O-Type Stars, ApJS, 2003, vol. 146, p. 417

Lanz T., Hubeny I., A grid of NLTE line-blanketed model atmospheres of early B-type stars, ApJS, 2007, vol. 169, p. 83

Lanz T., Hubeny I., Heap S. R., Non-LTE Line-blanketed Model Atmospheres of Hot Stars. III. Hot Subdwarfs: The sdO Star BD +75°325*, ApJ, 1997, vol. 485, p. 843

Lançon A., Gonneau A., Verro K., et al. A comparison between X-shooter spectra and PHOENIX models across the HR-diagram, A&A, 2021, vol. 649, p. A97

Lardo C., Mucciarelli A., Bastian N., The iron dispersion of the globular cluster M2, revised, MNRAS, 2016, vol. 457, p. 51–63

Lardo C., Salaris M., Cassisi S., Bastian N., Confirmation of a metallicity spread amongst first population stars in globular clusters, A&A, 2022, vol. 662, p. A117

Lardo C., Salaris M., Cassisi S., et al. High-precision abundances of first-population stars in NGC 2808: confirmation of a metallicity spread, A&A, 2023, vol. 669, p. A19

Le Borgne D., Rocca-Volmerange B., Prugniel P., et al. Evolutionary synthesis of galaxies at high spectral resolution with the code PEGASE-HR. Metallicity and age tracers, A&A, 2004, vol. 425, p. 881

Lee Y.-W., Joo S.-J., Han S.-I., et al. Super-Helium-rich Populations and the Origin of Extreme Horizontal-Branch Stars in Globular Clusters, ApJ, 2005, vol. 621, p. L57

Lei Z., Zhao J., Németh P., Zhao G., New Hot Subdwarf Stars Identified in Gaia DR2 with LAMOST DR5 Spectra. II. , ApJ, 2019a, vol. 881, p. 135

Lei Z., Zhao J., Németh P., Zhao G., New Hot Subdwarf Stars Identified in Gaia DR2 with LAMOST DR5 Spectra. II. , ApJ, 2019b, vol. 881, p. 135

Lei Z., Zhao J., Németh P., Zhao G., Hot Subdwarf Stars Identi fi ed in Gaia DR2 with Spectra of LAMOST DR6 and DR7 . I . Single-lined Spectra, ApJ, 2020, vol. 889, p. 117

Levenhagen R. S., Diaz M. P., Coelho P. R. T., Hubeny I., A Grid of Synthetic Spectra for Hot DA White Dwarfs and Its Application in Stellar Population Synthesis, ApJS, 2017, vol. 231, p. 1

Limberg G., Souza S. O., Pérez-Villegas A., et al. Reconstructing the Disrupted Dwarf Galaxy Gaia-Sausage/Enceladus Using Its Stars and Globular Clusters, ApJ, 2022, vol. 935, p. 109

Luo D., Pradhan A. K., Atomic data for opacity calculations. XI. The carbon isoelectronic sequence, Journal of Physics B Atomic Molecular Physics, 1989, vol. 22, p. 3377

Luo Y., Németh P., Deng L., Han Z., Hot subdwarf stars observed in Gaia DR2 and LAMOST DR5, The Astrophysical Journal, 2019, vol. 881

Luo Y., Németh P., Wang K., et al. Hot Subdwarf Atmospheric Parameters, Kinematics, and Origins Based on 1587 Hot Subdwarf Stars Observed in Gaia DR2 and LAMOST DR7, ApJS, 2021, vol. 256, p. 28

Lynas-Gray A. E., An Historical Overview, Ap&SS, 2004, vol. 291, p. 197

Maraston C., Evolutionary synthesis of stellar populations: a modular tool, MNRAS, 1998, vol. 300, p. 872

Maraston C., Evolutionary population synthesis: models, analysis of the ingredients and application to high-z galaxies, MNRAS, 2005, vol. 362, p. 799

Maraston C., Modelling Stellar Populations at High Redshift. In Tracing the Ancestry of Galaxies , vol. 277, 2011, p. 158

Maraston C., Strömbäck G., Stellar population models at high spectral resolution, MNRAS, 2011, vol. 418, p. 2785

Maraston C., Thomas D., Strong Balmer Lines in Old Stellar Populations: No Need for Young Ages in Ellipticals?, ApJ, 2000, vol. 541, p. 126

Martins L., Coelho P., Grids of synthetic stellar spectra, Canadian Journal of Physics, 2017, vol. 95, p. 840

Martins L. P., Coelho P. R. T., Testing the accuracy of synthetic stellar libraries, MNRAS, 2007, vol. 381, p. 1329

Martins L. P., Delgado R. M. G., Leitherer C., Cerviño M., Hauschildt P., A high-resolution stellar library for evolutionary population synthesis, MNRAS, 2005, vol. 358, p. 49

Martins L. P., Lima-Dias C., Coelho P. R., Laganá T. F., Testing stellar population fitting ingredients with Globular Clusters I: Stellar libraries, MNRAS, 2019, vol. 484, p. 2388

Martins L. P., Lima-Dias C., Coelho P. R. T., Laganá T. F., Testing stellar population fitting ingredients with Globular Clusters I: Stellar libraries, MNRAS, 2019, vol. 484, p. 2388

McLaughlin D. E., van der Marel R. P., Resolved Massive Star Clusters in the Milky Way and Its Satellites: Brightness Profiles and a Catalog of Fundamental Parameters, ApJS, 2005, vol. 161, p. 304

Mendoza C., Eissner W., LeDourneuf M., Zeippen C. J., Atomic data for opacity calculations. XXIII. The aluminium isoelectronic sequence, Journal of Physics B Atomic Molecular Physics, 1995, vol. 28, p. 3485

Mengel J. G., Norris J., Gross P. G., Binary Hypothesis for the Subdwarf B Stars, ApJ, 1976, vol. 204, p. 488

Mihalas D., Hummer D. G., Theory of extended stellar atmospheres, ApJS, 1974, vol. 265, p. 343

Milone A. P., Marino A. F., Piotto G., et al. The Hubble Space Telescope UV Legacy Survey of galactic globular clusters – II. The seven stellar populations of NGC 7089 (M2), MNRAS, 2014, vol. 447, p. 927–938

Moehler S., Hot Stars in Globular Clusters: A Spectroscopist's View, PASP, 2001, vol. 113, p. 1162

Moura T. C., Trevisan M., Barbuy B., Rossi S., Integrated Spectra of Milky Way Globular Clusters, ApJ, 2019, vol. 885, p. 28

Nahar S. N., Total electron-ion recombination of Fe III, Phys. Rev. A, 1996, vol. 53, p. 2417

Nahar S. N., Electron-ion recombination of FetII, Phys. Rev. A, 1997, vol. 55, p. 1980

Nahar S. N., Pradhan A. K., Atomic data for opacity calculations. XVIII. Photoionization and oscillator strengths of Si-like ions Si^0, S^{2+}, Ar^{4+}, Ca^{6+}, Journal of Physics B Atomic Molecular Physics, 1993, vol. 26, p. 1109

Nardiello D., Libralato M., Piotto G., et al. The Hubble Space Telescope UV Legacy Survey of Galactic Globular Clusters - XVII. Public Catalogue Release, MNRAS, 2018, vol. 481, p. 3382

Nemeth P., XTGRID Live: Online Spectral Analyses with TLUSTY Models. In Radiative Signatures from the Cosmos , vol. 519 of Astronomical Society of the Pacific Conference Series, 2019, p. 117

Németh P., Kawka A., Vennes S., A selection of hot subluminous stars in the GALEX survey - II. Subdwarf atmospheric parameters, MNRAS, 2012, vol. 427, p. 2180

Németh P., Østensen R., Tremblay P.-E., Hubeny I., Synthetic spectra for O and B type subdwarf stars, PASP, 2014, vol. 481

Ocvirk P., Fake Star Formation Bursts: Blue Horizontal Branch Stars Masquerade as Young Massive Stars in Optical Integrated Light Spectroscopy, ApJ, 2010, vol. 709, p. 88

O'Toole S. J., Heber U., Abundance studies of sdB stars using UV echelle HST/STIS spectroscopy, A&A, 2006, vol. 452, p. 579

Pacheco T. A., Coelho P. R. T., Martins L. P., et al. Subdwarf synthetic spectra to study hot components in old stellar populations. In Astronomy in Focus XXXI , vol. Accepted, 2024

Pacheco T. A., Diaz M. P., Levenhagen R. S., Coelho P. R. T., A Grid of Synthetic Spectra for Subdwarfs: Non-LTE Line-blanketed Atmosphere Models, ApJS, 2021, vol. 256, p. 41

Pacheco T. A., Levenhagen R. S., Diaz M. P., Coelho P. R. T., A grid of Non-LTE line-blanketed atmosphere structures and synthetic spectra for subdwarfs, Bull. Soc. R. Sci. Liege, 2023, vol. 92, p. 2

Peach G., Saraph H. E., Seaton M. J., Atomic data for opacity calculations. IX. The lithium isoelectronic sequence, Journal of Physics B Atomic Molecular Physics, 1988, vol. 21, p. 3669

Pedregosa F., Varoquaux G., Gramfort A., et al. Scikit-learn: Machine Learning in Python, Journal of Machine Learning Research, 2011, vol. 12, p. 2825

Pelisoli I., Vos J., Geier S., et al. Alone but not lonely: Observational evidence that binary interaction is always required to form hot subdwarf stars, A&A, 2020, vol. 642, p. A180

Peterson R. C., Carney B. W., Dorman B., et al. Blue Horizontal-Branch Stars in Old, Metal-rich Stellar Systems, ApJ, 2003, vol. 588, p. 299

Piotto G., King I. R., Djorgovski S. G., et. al HST color-magnitude diagrams of 74 galactic globular clusters in the HST F439W and F555W bands, A&A, 2002, vol. 391, p. 945

Piotto G., Milone A. P., Bedin L. R., et al. The Hubble Space Telescope UV Legacy Survey of Galactic Globular Clusters. I. Overview of the Project and Detection of Multiple Stellar Populations, AJ, 2015, vol. 149, p. 91

Prugniel P., Soubiran C., A database of high and medium-resolution stellar spectra, A&A, 2001, vol. 369, p. 1048–1057

Rauch T., Demleitner M., Hoyer D., Werner K., Stellar parameters for the central star of the planetary nebula PRTM 1 using the German Astrophysical Virtual Observatory service TheoSSA, MNRAS, 2018, vol. 475, p. 3896

Rebassa-Mansergas A., Parsons S. G., Dhillon V. S., Ren J., Littlefair S. P., Marsh T. R., Torres S., Accurate mass and radius determinations of a cool subdwarf in an eclipsing binary, Nature Astronomy, 2019, vol. 3, p. 553

Rennó C., Barbuy B., Moura T. C., Trevisan M., Abundances from integrated spectra of 47 Tucanae (NGC 104), MNRAS, 2020, vol. 498, p. 5834

Renzini A., Buzzoni A., Global properties of stellar populations and the spectral evolution of galaxies.. In Spectral Evolution of Galaxies , vol. 122 of Astrophysics and Space Science Library, 1986, p. 195

Rodrigo C., Solano E., The SVO Filter Profile Service. In XIV.0 Scientific Meeting (virtual) of the Spanish Astronomical Society , 2020a, p. 182

Rodrigo C., Solano E., The SVO Filter Profile Service. In XIV.0 Scientific Meeting (virtual) of the Spanish Astronomical Society , 2020b, p. 182

Rodrigo C., Solano E., Bayo A., , 2012a SVO Filter Profile Service Version 1.0 IVOA Working Draft 15 October 2012

Rodrigo C., Solano E., Bayo A., , 2012b SVO Filter Profile Service Version 1.0 IVOA Working Draft 15 October 2012

Rodríguez-Merino L. H., Chavez M., Bertone E., Buzzoni A., UVBLUE: A New High-Resolution Theoretical Library of Ultraviolet Stellar Spectra, ApJ, 2005, vol. 626, p. 411

Rutten R. J., Radiative transfer in stellar atmospheres 8th edition edn. Utrecht University lecture notes, 2003

Saffer R. A., Green E. M., Bowers T. P., The binary origins of Hot Subdwarfs: New radial velocities, ASP Conference Series, 2000, vol. 47

Sale S. E., Schoenaers C., Lynas-Gray A. E., A New Determination of Abundances for the Subdwarf B Star HD 4539. In Hot Subdwarf Stars and Related Objects , vol. 392 of Astronomical Society of the Pacific Conference Series, 2008, p. 109

Sánchez-Blázquez P., Peletier R. F., Jiménez-Vicente J., et al. Medium-resolution Isaac Newton Telescope library of empirical spectra, MNRAS, 2006, vol. 371, p. 703

Sandage A., The Light Travel Time and the Evolutionary Correction to Magnitudes of Distant Galaxies., ApJ, 1961, vol. 134, p. 916

Santos J. F. C. J., Bica E., Dottori H., Spectral Synthesis Aided by the H-R Diagram: The Open Cluster M11, PASP, 1990, vol. 102, p. 454

Santos J. F. C. J., Bica E., Dottori H., et al. Synthesis of the integrated spectrum of metal-rich globular clusters using the HR diagram and a stellar library., A&A, 1995, vol. 303, p. 753

Schiavon R. P., Caldwell N., Rose J. A., The Integrated Spectrum of M67 and the Spectroscopic Age of M32, AJ, 2004, vol. 127, p. 1513

Schiavon R. P., Rose J. A., Courteau S., MacArthur L. A., A Library of Integrated Spectra of Galactic Globular Clusters, ApJS, 2005, vol. 169, p. 163

Schiavon R. P., Rose J. A., Macarthur L. A., The identification of blue horizontal-branch stars in the integrated spectra of globular clusters, The Astrophysical Journal, 2004, vol. 608, p. 33

Schöning T., Butler K., Stark broadening of He II lines, ApJS, 1989, vol. 78, p. 51

Schwab J., Hot subdwarfs formed from the merger of two He white dwarfs, MNRAS, 2018, vol. 476, p. 5303

Shamey L. J., Stark Broadening of Important Helium i Lines and Their Forbidden Components., Uiversity of Colorado at Boulder, 1969, Ph.D. Thesis

Sharma K., Prugniel P., Singh H. P., New atmospheric parameters and spectral interpolator for the MILES cool stars, A&A, 2015, vol. 585, p. A64

Soubiran C., Katz D., Cayrel R., On-line determination of stellar atmospheric parameters T_{eff}, log g, [Fe/H] from ELODIE echelle spectra. II. The library of F5 to K7 stars, A&AS, 1998, vol. 133, p. 221

Spinrad H., Normal Galaxies in the Post-Baade ERA, PASP, 1966, vol. 78, p. 367

Sweigart A. V., Brown T. M., Lanz T., et al. The Origin of Hot Subluminous Horizontal-Branch Stars in ω Centauri and NGC 2808. In Omega Centauri, A Unique Window into Astrophysics , vol. 265 of Astronomical Society of the Pacific Conference Series, 2002, p. 261

Taylor M. B., TOPCAT & STIL: Starlink Table/VOTable Processing Software. In Astronomical Data Analysis Software and Systems XIV , vol. 347 of Astronomical Society of the Pacific Conference Series, 2005, p. 29

Thomas D., Maraston C., Bender R., Stellar population models of Lick indices with variable element abundance ratios, MNRAS, 2003, vol. 339, p. 897

Tinsley B. M., Evolution of the Stars and Gas in Galaxies, ApJ, 1968, vol. 151, p. 547

Tinsley B. M., Galactic Evolution, A&A, 1972, vol. 20, p. 383

Tinsley B. M., Analytical Approximations to the Evolution of Galaxies, ApJ, 1973, vol. 186, p. 35

Tremblay P. E., Bergeron P., Spectroscopic analysis of DA white dwarfs: Stark broadening of hydrogen lines including nonideal effects, The Astrophysical Journal, 2009, vol. 696, p. 308

Tully J. A., Seaton M. J., Berrington K. A., Atomic data for opacity calculations. XIV. The beryllium sequence, Journal of Physics B Atomic Molecular Physics, 1990, vol. 23, p. 3811

Usher C., Pastorello N., Bellstedt S., et al. The WAGGS project - I. The WiFeS Atlas of Galactic Globular cluster Spectra, MNRAS, 2017, vol. 468, p. 3828

Verro K., Trager S. C., Peletier R. F., et al. The X-shooter Spectral Library (XSL): Data Release 3, A&A, 2022, vol. 660, p. A34

Wade R. A., Stark M. A., Green R. F., How Many Hot Subdwarf Stars Were Rejected from the PG Survey?. In 14th European Workshop on White Dwarfs , vol. 334 of Astronomical Society of the Pacific Conference Series, 2005, p. 123

Worthey G., Faber S. M., Gonzalez J. J., MG and Fe absorption features in elliptical galaxies, ApJ, 1992, vol. 398, p. 69

Worthey G., Lee H.-C., An Empirical UBV RI JHK Color-Temperature Calibration for Stars, ApJS, 2011, vol. 193, p. 1

Yi S., Lee Y., Woo J., et al. The Ultraviolet Upturn in Elliptical Galaxies as an Age Indicator, ApJ, 1999, vol. 513, p. 128

Yi S. K., The Current Understanding on the UV Upturn. In Hot Subdwarf Stars and Related Objects , vol. 392 of Astronomical Society of the Pacific Conference Series, 2008, p. 3

Yong D., Roederer I. U., Grundahl F., et al. Iron and neutron-capture element abundance variations in the globular cluster M2 (NGC 7089), MNRAS, 2014, vol. 441, p. 3396

Yoon S.-J., Lee Y.-W., Rey S.-C., et al. Horizontal-Branch Stars as Sources of the UV Upturn in Early-Type Galaxies, Ap&SS, 2004, vol. 291, p. 223

Appendix

Appendix A

Atomic data

Table A.1 is a complement of Table 2.1, where we list the number of levels, super levels, and lines for each species included in the NLTE atmosphere models. Also, the references are shown as follows: (1) Lanz and Hubeny 2003; Lanz and Hubeny 2007; (2) `http://physics.nist.gov/PhysRefData/ASD/index.html`; (3) Luo and Pradhan 1989; (4) Fernley et al. 1999; (5) Tully et al. 1990; (6) Peach et al. 1988; (7) Hibbert and Scott 1994; (8) Butler et al. 1993; (9) Mendoza et al. 1995; (10) Nahar and Pradhan 1993; (11) Kurucz 1994; (12) Nahar 1997; (13) Nahar 1996; (14) Bautista and Pradhan 1997; (15) Bautista 1996. See more details in Lanz and Hubeny 2003 and Lanz and Hubeny 2007.

Table A.1 - Atomic data of the explicit species.

Ions	Super(level)	Lines	Reference
H^-	1	1	1
H	9	172	1
He	24	784	2
He II	20	190	1
C	40	3 201	3
C II	22	238	4
C III	46	738	5
C IV	25	330	6
N	34	785	1
N II	42	3 396	3
N III	32	549	4
N IV	48	1 093	5

Table A.1 - Continued. Atomic data of the explicit species.

Ions	Super(level)	Lines	Reference
N V	16	330	6
O	33	418	1
O II	48	3 484	1
O III	41	3 855	3
O IV	39	922	4
O V	6	4	4
Ne	35	2 715	7
Ne II	32	2 301	1
Ne III	34	1 354	1
Ne IV	12	38	1
Mg II	25	306	1
Al II	29	536	8
Al III	23	306	1
Si II	40	392	9
Si III	30	747	8
Si IV	23	306	1
S II	33	4 166	1
S III	41	3 452	10
S IV	38	909	9
S V	25	1 171	8
S VI	16	398	1
Fe II	36	1 264 969	12, 13
Fe III	50	1 604 934	11, 13
Fe IV	43	1 776 984	11, 14
Fe V	42	1 008 835	11, 15
Fe VI	32	40 298	11, 15